# AzTEC 1.1 mm observations of high-z protocluster environments

Monthly Notices
of the
ROYAL ASTRONOMICAL SOCIETY

MNRAS **479,** 4577–4632 (2018)
Advance Access publication 2018 June 29

doi:10.1093/mnras/sty1714

# AzTEC 1.1 mm observations of high-$z$ protocluster environments: SMG overdensities and misalignment between AGN jets and SMG distribution

M. Zeballos,[1,2] I. Aretxaga,[2] D. H. Hughes,[2] A. Humphrey,[3] G. W. Wilson,[4] J. Austermann,[5] J. S. Dunlop,[6] H. Ezawa,[7] D. Ferrusca,[2] B. Hatsukade,[8] R. J. Ivison,[6,9] R. Kawabe,[10,11,12] S. Kim,[13] T. Kodama,[10,12] K. Kohno,[8,14] A. Montaña,[2] K. Nakanishi,[10,12] M. Plionis,[15,16] D. Sánchez-Argüelles,[2] J. A. Stevens,[17] Y. Tamura,[8] M. Velazquez[2] and M. S. Yun[4]

*Affiliations are listed at the end of the paper*

Accepted 2018 June 14. Received 2018 June 13; in original form 2017 March 14

## ABSTRACT

We present observations at 1.1 mm towards 16 powerful radio galaxies and a radio-quiet quasar at $0.5 < z < 6.3$ acquired with the AzTEC camera mounted at the James Clerk Maxwell Telescope and Atacama Submillimeter Telescope Experiment to study the spatial distribution of submillimetre galaxies (SMGs) towards possible protocluster regions. The survey covers a total area of 1.01 sq deg with rms depths of 0.52–1.44 mJy and detects 728 sources above $3\sigma$. We find overdensities of a factor of $\sim$2 in the source counts of three individual fields (4C+23.56, PKS1138−262, and MRC0355−037) over areas of $\sim$200 sq deg. When combining all fields, the source-count analysis finds an overdensity that reaches a factor $\gtrsim$3 at $S_{1.1\mathrm{mm}} \geq 4$ mJy covering a 1.5-arcmin-radius area centred on the active galactic nucleus. The large size of our maps allows us to establish that beyond a radius of 1.5 arcmin, the radial surface density of SMGs falls to that of a blank field. In addition, we find a trend for SMGs to align closely to a perpendicular direction with respect to the radio jets of the powerful central radio galaxies ($73^{-14}_{+13}$ deg). This misalignment is found over projected comoving scales of 4–20 Mpc, departs from perfect alignment (0 deg) by $\sim 5\sigma$, and apparently has no dependence on SMG luminosity. Under the assumption that the AzTEC sources are at the redshift of the central radio galaxy, the misalignment reported here can be interpreted as SMGs preferentially inhabiting mass-dominant filaments funnelling material towards the protoclusters, which are also the parent structures of the radio galaxies.

**Key words:** galaxies: active – galaxies: evolution – galaxies: starburst – submillimetre: galaxies.

## 1 INTRODUCTION

Clusters of galaxies are the largest virialized structures in the Universe, with masses that range $10^{14}$–$10^{16}$ $M_\odot$. They originate from the gravitational collapse of matter and represent extreme potential wells developed from the initial conditions in the density field of the Universe. Thus, they are natural laboratories for studying evolutionary scenarios for the formation of large-scale structure (e.g. Jimenez & Verde 2009; Harrison & Coles 2012), and specifically, for the formation and evolution of galaxies (e.g. Demarco et al. 2010).

Despite extensive multiwavelength studies towards clusters in the nearby Universe, their progenitors remain relatively unexplored. Protocluster identification is difficult because of the small difference in density between the forming cluster and its surroundings. In addition, classical cluster detection techniques such as searching for extended X-ray emission (e.g. Rosati et al. 1998; Pierre et al. 2004) and identifying red galaxy overdensities (e.g. Andreon et al. 2009; Demarco et al. 2010) fail to work for $z > 2.5$. Both the X-ray emission produced by the hot intracluster medium (ICM) and the optical light emitted by red galaxies suffer from cosmological dimming due to the expansion of the Universe. Furthermore, these identification techniques, as well as the Sunyaev–Zeldóvich effect (e.g. Menanteau et al. 2009; Planck Collaboration et al. 2013), usually detect signals of an already evolved cluster,

* E-mail: zeballos@inaoep.mx

with an old galaxy population and a virialized environment heating the ICM.

One the most popular techniques to search for protoclusters has been targeting the fields of the most powerful high-redshift radio galaxies (RGs) and quasars (active galactic nucleus, AGN; e.g. Kurk et al. 2000; McLure & Dunlop 2001). Since these AGNs are hosted by the most massive galaxies in the Universe, they pinpoint the location of the highest density regions under the currently most accepted paradigm of structure formation, the $\Lambda$ cold dark matter ($\Lambda$CDM) model.

Evidence for the large masses of powerful AGN host galaxies comes from the radio/optical luminosities of the AGN itself, which indicate the presence of a supermassive black hole (SMBH). In the nearby Universe, there is a well-studied correlation between SMBH mass and the bulge luminosity of the host galaxy (e.g. McLure & Dunlop 2002), and although at higher redshifts this correlation is still under scrutiny (e.g. Wang et al. 2013; Willott, Bergeron & Omont 2015), powerful AGNs are expected to inhabit massive galaxies. In addition, RGs at high redshifts were found to have the largest *K*-band luminosities in the early Universe, which indicates stellar masses of up to $10^{12}\,M_{\odot}$ (e.g. Rocca-Volmerange et al. 2004; Seymour et al. 2007; Targett et al. 2011). Another piece of evidence comes from the existence of giant nebulae of ionized gas surrounding them, with sizes of up to $\sim$200 kpc, which contain enough gas to produce systems as large as cD-like galaxies (e.g. Reuland et al. 2003).

Previous narrow-band filter observations towards the environments of high-redshift AGN found overdensities of a variety of star-forming galaxies such as Ly$\alpha$ emitters (e.g. Venemans et al. 2007), H$\alpha$ emitters (e.g. Kurk et al. 2004; Hatch et al. 2011; Hayashi et al. 2012), and Lyman break galaxies (e.g. Miley et al. 2004; Overzier et al. 2006; Intema et al. 2006). These type of observations, however, trace relatively low-mass galaxies with unobscured star formation. Since about 50 per cent of the cosmic star formation is obscured by dust (e.g. Dole et al. 2006), far-infrared (far-IR), submillimetre (submm), or millimetre (mm) observations are required to fully understand the formation history of stellar mass in galaxy clusters. Besides recent systematic searches in *Planck* all sky maps (e.g. Planck Collaboration et al. 2015; Clements et al. 2014; Flores-Cacho et al. 2016), the primary protocluster identification technique used at these wavelengths has been targeting the fields of powerful AGNs (e.g. Stevens et al. 2003; De Breuck et al. 2004; Priddey, Ivison & Isaak 2008; Stevens et al. 2010; Wylezalek et al. 2013; Dannerbauer et al. 2014; Rigby et al. 2014) with the highest radio, optical, or X-ray luminosities and at the highest redshifts ($\gtrsim 2$). In most cases, these studies found a number density of sources $\geq$2 larger than blank-field estimates, consistent with these regions being extreme density peaks in the Universe.

Far-IR/submm/mm studies towards these biased regions are sensitive to a heavily obscured star-forming galaxy population characterized by extreme far-IR luminosities ($L_{\rm FIR} > 10^{12}\,L_{\odot}$), large star formation rates (SFR $>$100–1000 $M_{\odot}\,{\rm yr}^{-1}$), and a redshift distribution with $\sim$50 per cent of bright sources at $2 < z < 3$ (e.g. Chapman et al. 2003, 2005; Aretxaga et al. 2003, 2007; Pope et al. 2005; Wardlow et al. 2011; Smolčić et al. 2012; Simpson et al. 2014) with a possible tail towards higher values (e.g. Coppin et al. 2009; Riechers et al. 2010; Cox et al. 2011; Yun et al. 2012; Walter et al. 2012). This implies that they are a young population capable of building large stellar masses in $<$1 Gyr (provided the star-forming activity is sustained for the whole period of time; see Casey, Narayanan & Cooray 2014 for a review). Therefore, they are very good candidates to be the progenitors of the massive galaxies that we see today as the dominant population in the centre of rich galaxy clusters. In addition, recent studies of SMGs at $z = 1$–3 estimate stellar masses of $>10^{11}\,M_{\odot}$ (e.g. Dye et al. 2008; Targett et al. 2013), molecular gas masses of $\sim 5 \times 10^{10}\,M_{\odot}$ (e.g. Greve et al. 2005; Bothwell et al. 2013), and dust masses of $\sim 10^{8}\,M_{\odot}$ (e.g. Chapman et al. 2005; Magnelli et al. 2012), values that also support the theory that SMGs are destined to evolve into massive ellipticals in the low-redshift Universe. Studying the properties of SMGs towards protocluster regions will improve our understanding of the still elusive formation history of these massive galaxies, and possibly give us an insight into the formation of the stellar population of the richest galaxy clusters.

In this paper, we present 1.1 mm continuum imaging observations towards the environments of 16 powerful high-redshift RGs and a quasar acquired with the AzTEC camera (Wilson et al. 2008a). This sample is a subset of the AzTEC Cluster Environment Survey (ACES), which observed 40 fields towards powerful AGNs and massive galaxy clusters. We introduce the sample in Section 2. Section 3 describes the details of the observations, and Section 4 explains the data reduction process in order to obtain clean and optimally filtered sky maps. Section 5 estimates the number density of sources as a function of flux density for individual and combined fields, and Section 6 analyses a possible relation between the spatial distribution of SMGs and the radio jet directions of the RGs in the sample. In Section 7, we discuss our results, and in Section 8, we summarize the conclusions of the paper.

Throughout this paper, we adopt a flat cosmology with $\Omega_{\rm M} = 0.27$, $\Omega_{\Lambda} = 0.73$, and $H_0 = 71\,{\rm km\,s^{-1}\,Mpc^{-1}}$.

## 2 SAMPLE SELECTION

### 2.1 Target fields

We targeted fields centred on luminous AGN at $0.5 < z < 6.3$ which were known or suspected to be hosted by massive galaxies, as potential signposts of high-redshift overdensities. Our powerful high-redshift RGs are among the prime AGN to pinpoint protoclusters due to their location at the high end of the luminosity–redshift ($L_{500\,\rm MHz} - z$) plane, with luminosities in the range $26.5 < \log_{10}(L_{500\,\rm MHz}) < 28.1$ W Hz$^{-1}$ (Fig. 1) and their high-mass end SMBHs. We also include two Gigahertz Peaked Spectrum (GPS) sources, TXS2322-040 and MRC2008-068, that show lower 500-MHz luminosities due to synchrotron self-absorption, but some theories place them as young counterparts of classical extended radio sources (e.g. O'Dea 1998). More importantly, *R*- and *K*-band images show that these type of sources are also massive galaxies in their own right (Snellen et al. 1996a,b).

All fields are located far from the galactic plane and, in general, far from where there is large contamination by galactic cirrus. On average, these regions show background dust emission variations at 100 μm that are $<$0.3 mJy sr$^{-1}$. This yields a cirrus confusion noise $<$0.6 mJy beam$^{-1}$ at the wavelength (1.1 mm) and beam size (30 and 18 arcsec) of our observations under the assumption of an isothermal dust spectrum with $T = 19$ K and emissivity index $\beta = 1.4$ (Bracco et al. 2011).

Although seven of these selected targets were already confirmed as rich protoclusters via narrow-line emission observations (TNJ0924−2201, TNJ1338−1942, MRC0316−257, PKS0529−549, MRC2104−242, 4C+23.56, and PKS1138−262), the selection criteria of the fields were unbiased regarding previous overdensity detections.

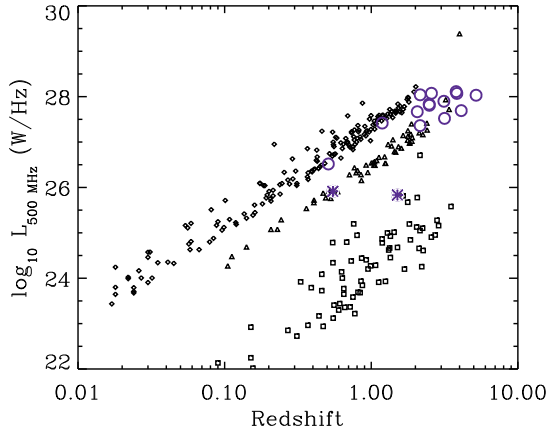


**Figure 1.** Radio luminosity–redshift ($L_{500\,\mathrm{MHz}}$–$z$) plane for radio surveys 3CRR (diamonds; Laing, Riley & Longair 1983), 6CE (triangles; Eales 1985; Rawlings, Eales & Lacy 2001), and LBDS (squares, Lynx and Hercules fields only; Rigby, Snellen & Best 2007), which have successively deeper flux-density limits. These radio luminosities were calculated using a typical spectral index of 0.8 (de Zotti et al. 2010). Open circles denote ACES RGs whose synchrotron self-absorption frequency appears to be at <500 MHz (rest frame). Asterisks denote the 2 GPS sources we include in our sample. ACES AGN luminosities were estimated by fitting a straight line or a parabola to their spectra, depending on the number of data points available.

We complete the ACES protocluster sample with one extra field centred at the optically luminous ($M_B = -27.7$) radio-quiet quasar (RQ-QSO) SDSSJ1030+0524 ($z = 6.28$), which at the time of our observations was the highest redshift known quasar. The list of selected targets is shown in Table 1.

### 2.2 Control field

AzTEC observed, together with the ACES sample, a set of well-known blank fields with available multiwavelength data (Scott et al. 2012, and references therein). This set covers a total area of 1.6 sq deg with a depth range between 0.4 and 1.7 mJy beam$^{-1}$, and provides the best estimation to-date of the surface density of SMGs towards blank fields at flux densities between $S_{1.1\mathrm{mm}} = 1$–12 mJy. We use these data to compare the properties of the SMGs in our sample against those of SMGs in unbiased environments.

## 3 OBSERVATIONS

The ACES protocluster sample was surveyed at a wavelength of 1.1 mm with the AzTEC camera as a visiting instrument at the 15-m James Clerk Maxwell Telescope (JCMT; FWHM = 18 arcsec) in Hawaii and at the 10-m Atacama Submillimeter Telescope Experiment (ASTE; FWHM = 30 arcsec) in the northern part of Chile. The field towards 4C+41.17 was observed at the JCMT in 2005 December, and the other 16 fields were observed at the ASTE from 2007 May to October and 2008 July to December. The sample was observed under very good weather conditions: for 95 per cent of the observing time the zenith atmospheric opacity was $\tau_{220\,\mathrm{GHz}} < 0.095$ at the ASTE and $\tau_{225\,\mathrm{GHz}} < 0.115$ at the JCMT. The zenith opacity mean and standard deviation values for each field are given in Table 2.

The 4C+41.17 field was mapped using a raster scanning technique, while the ASTE fields were mapped using a Lissajous pattern centred on the AGN. Integration times varied between 16 and 35 h per field (excluding calibration and pointing observations), and the resulting maps cover uniform noise areas ranging from 170 to 300 sq arcmin.

AzTEC maps were calibrated using planets as primary calibrators. Each night Uranus or Neptune was imaged to derive the flux conversion factor for each detector. In a single observation of a field, the typical statistical calibration error was 6–13 per cent (Wilson et al. 2008a). When all observations in each field are considered, the calibration errors on our measured source flux densities integrate down to 1.7–2.5 per cent, which need to be combined in quadrature with the 5 per cent absolute uncertainty on the flux densities of the planets.

**Table 1.** General properties of the AGN targeted in the AzTEC observations. There are 16 RG and an RQ-QSO. The columns show: (1) AGN name; (2) AGN type; (3) and (4) their most accurate coordinates as determined from radio, optical, or mid(near)-IR data; (5) redshift; (6) radio luminosity estimated at a rest-frame frequency of 500 MHz; (7) PA of the radio emission measured north to east; and (8) reference for PA.

| Central AGN | Type | RA (J2000) (hr:m:s) | Dec. (J2000) (d:am:as) | $z$ | $\log_{10}$(L) (W Hz$^{-1}$) | PA (deg) | References |
|---|---|---|---|---|---|---|---|
| SDSSJ1030+0524 | RQ-QSO | 10:30:27.10 | +05:24:55.0 | 6.311 | | | |
| TNJ0924−2201 | RG | 09:24:19.91 | −22:01:41.5 | 5.190 | 28.03 | 74 | De Breuck et al. (2000) |
| TNJ1338−1942 | RG | 13:38:26.23 | −19:42:33.6 | 4.110 | 27.69 | 152 | De Breuck et al. (2000) |
| TNJ2007−1316 | RG | 20:07:53.22 | −13:16:43.4 | 3.837 | 28.07 | 27 | De Breuck (private communication) |
| 4C+41.17 | RG | 06:50:52.35 | +41:30:31.4 | 3.792 | 28.11 | 48 | Chambers, Miley & van Breugel (1990) |
| TNJ2009−3040 | RG | 20:09:48.08 | −30:40:07.4 | 3.160 | 27.52 | 144 | De Breuck et al. (2000) |
| MRC0316−257 | RG | 03:18:12.14 | −25:35:10.2 | 3.130 | 27.90 | 51 | McCarthy et al. (1990) |
| PKS0529−549 | RG | 05:30:25.43 | −54:54:23.3 | 2.575 | 28.07 | 104 | Broderick et al. (2007) |
| MRC2104−242 | RG | 21:06:58:27 | −24:05:09.1 | 2.491 | 27.81 | 12 | Pentericci et al. (2001) |
| 4C+23.56 | RG | 21:07:14.82 | +23:31:45.1 | 2.483 | 27.84 | 52 | Chambers et al. (1996) |
| PKS1138−262 | RG | 11:40:48.35 | −26:29:08.6 | 2.156 | 28.04 | 90 | Pentericci et al. (1997) |
| MRC0355−037 | RG | 03:57:48.06 | −03:34:09.5 | 2.153 | 27.36 | 120 | Gopal-Krishna et al. (2005) |
| MRC2048−272 | RG | 20:51:03.49 | −27:03:03.7 | 2.060 | 27.67 | 45 | Kapahi et al. (1998) |
| TXS2322−040 | RG | 23:25:10.23 | −03:44:46.7 | 1.509 | 25.83 | −4 | Xiang et al. (2006) |
| MRC2322−052 | RG | 23:25:19.62 | −04:57:36.6 | 1.188 | 27.42 | 107 | Best et al. (1999) |
| MRC2008−068 | RG | 20:11:14.22 | −06:44:03.6 | 0.547 | 25.92 | −28 | Morganti, Killeen & Tadhunter (1993) |
| MRC2201−555 | RG | 22:05:04.83 | −55:17:44.0 | 0.510 | 26.52 | −85 | Burgess & Hunstead (2006) |

**Table 2.** Main properties of the AGN fields targeted in the AzTEC observations. The columns are: (1) RG or quasar at which the map is centred; (2) telescope used; (3) uniform noise area determined by a 50 per cent coverage cut; (4) range of noise rms values inside this area; (5) integration time (excluding calibration and pointing observations); (6) zenith opacity mean and standard deviation values measured at 220 GHz for the ASTE fields and at 225 GHz for the JCMT field; and (7) scanning pattern used to observe the target.

| Central AGN | Telescope | Area (arcmin$^2$) | Noise rms range (mJy beam$^{-1}$) | Int. time (h) | $\tau$ | Scan type |
|---|---|---|---|---|---|---|
| SDSSJ1030+0524 | ASTE | 212.6 | 0.52–0.77 | 31.82 | $0.035 \pm 0.020$ | Lissajous |
| TNJ0924−2201 | ASTE | 210.6 | 0.85–1.26 | 30.14 | $0.041 \pm 0.023$ | Lissajous |
| TNJ1338−1942 | ASTE | 209.5 | 0.96–1.44 | 16.48 | $0.064 \pm 0.023$ | Lissajous |
| TNJ2007−1316 | ASTE | 211.3 | 0.90–1.34 | 19.50 | $0.051 \pm 0.015$ | Lissajous |
| 4C+41.17 | JCMT | 303.3 | 0.97–1.42 | 35.44 | $0.074 \pm 0.027$ | Raster |
| TNJ2009−3040 | ASTE | 211.9 | 0.88–1.32 | 19.49 | $0.063 \pm 0.048$ | Lissajous |
| MRC0316−257 | ASTE | 211.7 | 0.65–0.96 | 22.28 | $0.045 \pm 0.016$ | Lissajous |
| PKS0529−549 | ASTE | 213.4 | 0.62–0.92 | 28.33 | $0.038 \pm 0.016$ | Lissajous |
| MRC2104−242 | ASTE | 209.1 | 0.83–1.24 | 24.87 | $0.046 \pm 0.015$ | Lissajous |
| 4C+23.56 | ASTE | 166.0 | 0.55–0.85 | 34.43 | $0.057 \pm 0.030$ | Lissajous |
| PKS1138−262 | ASTE | 211.6 | 0.70–1.04 | 42.14 | $0.042 \pm 0.025$ | Lissajous |
| MRC0355−037 | ASTE | 212.4 | 0.78–1.15 | 25.72 | $0.043 \pm 0.016$ | Lissajous |
| MRC2048−272 | ASTE | 211.7 | 0.73–1.09 | 19.88 | $0.054 \pm 0.017$ | Lissajous |
| TXS2322−040 | ASTE | 212.1 | 0.61–0.91 | 23.67 | $0.037 \pm 0.014$ | Lissajous |
| MRC2322−052 | ASTE | 212.4 | 0.68–1.01 | 23.68 | $0.051 \pm 0.019$ | Lissajous |
| MRC2008−068 | ASTE | 211.9 | 0.83–1.24 | 20.70 | $0.045 \pm 0.020$ | Lissajous |
| MRC2201−555 | ASTE | 213.4 | 0.74–1.11 | 26.45 | $0.089 \pm 0.062$ | Lissajous |

In order to correct the observations for small pointing offsets between the centre of the AzTEC array and the telescope boresight, well-known bright point sources (>1 Jy) a few degrees away from the science targets were periodically observed. They were taken every 1 or 2 h, always bracketing the ACES protocluster observations. The resulting absolute pointing uncertainty of the AzTEC maps is <2 arcsec, much smaller than our beam sizes (18 and 30 arcsec).

## 4 DATA REDUCTION AND ANALYSIS

We reduced the AzTEC data in a manner similar to that described in detail by Scott et al. (2008, 2012).

The raw timestream data from the instrument, which include both bolometer and pointing data, are despiked and then cleaned of atmospheric contamination using the standard principal component analysis technique. An astrometric correction is made to all pointing signals in the timestream based on a linear interpolation of the pointing offsets measured by the bracketing pointing observations. With this correction in place, the bolometer signals are flux-calibrated and binned into $3 \times 3$ ($2 \times 2$) sq arcsec pixels for ASTE (JCMT) observations. Performing this process for observations of each field results in independent maps which are then co-added to make a preliminary image of the sky around the AGN of choice. As in previous AzTEC analyses, we also produce a weight map and 100 noise-only realizations of each field. The weight map is built by adding in quadrature the inverse of the variance of all bolometer samples that contribute to a pixel, i.e. it represents the inverse of the squared noise level per pixel (pixel weight). The noise maps, on the other hand, are produced by jackknifing the timestream data and used in the characterization of the map properties.

In order to remove pixel-to-pixel variations, each preliminary AzTEC map needs to be convolved with the point-source response of the instrument. This point-source kernel is obtained by inserting three fake sources in the timestreams that made the original map and tracing them through the entire reduction process. A detailed description can be found in Downes et al. (2012). We use the mean power spectral density of the noise maps and the estimated point-source kernel to construct an optimal filter for point-source detection. The final set of filtered maps for each ACES protocluster field is composed of: a filtered signal map, a filtered weight map, the corresponding signal-to-noise (S/N) map, and a set of 100 filtered noise realizations.

### 4.1 The maps

Fig. 2 shows the final signal and weight maps towards the field of the RG PKS1138−262. The rest of the maps can be seen in Appendix A. Contours represent curves of constant noise and have values of 0.84 and 1.04 mJy beam$^{-1}$. The central part of the map is slightly deeper than the edges, and the noise increases rapidly towards them. Therefore, all the analysis is restricted to the central area where pixel weights are larger than 50 per cent of the maximum weight (50 per cent coverage-cut area).

Table 2 lists the 50 per cent coverage-cut areas for all the ACES protocluster fields, 15 of which cover areas of ∼8 arcmin radius. The 4C+23.56 map is slightly smaller, with a ∼6 arcmin radius, but large enough to cover a possible protocluster centred at the RG position and at the RG redshift (comoving area of ∼10 Mpc radius at $z = 2.48$). On the other hand, the 4C+41.17 map is the largest, covering an area of ∼10 arcmin radius. Table 2 also shows noise rms values for each ACES protocluster target. Since integration times per pixel slowly decrease from the centre of the map towards the edges, the quoted noise rms values are intervals. All noise rms values are <1.5 mJy beam$^{-1}$.

Using the standard rule of thumb (one source per 30 beams) and the AzTEC blank-field 1.1 mm source counts, we estimate the confusion limit given the 30 arcsec (18 arcsec) FWHM ASTE (JCMT) beam to be 2.1 (1.0) mJy. Our ACES/ASTE survey is 2–4 times deeper than the formal confusion limit. Therefore, in the next sections, we consider its effects on the properties of ours map following the analysis in Scott et al. (2010).

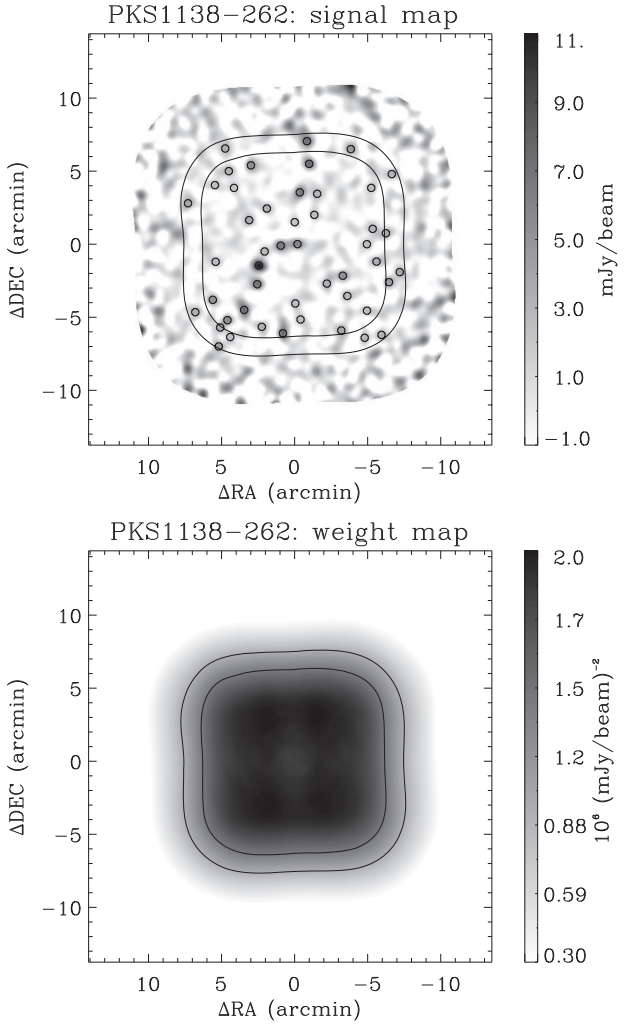


**Figure 2.** AzTEC signal and weight maps for the ACES protocluster candidate towards PKS1138−262. Source candidates with S/N >3 are marked by 30-arcsec diameter circles (FWHM at the ASTE). Contours represent curves of constant noise of 0.84 and 1.04 mJy beam$^{-1}$ (75 per cent and 50 per cent coverage cuts).

### 4.2 Source catalogues

Source candidates are identified in the S/N maps as local maxima above an S/N threshold of 3.5 for the shallowest maps (TNJ1338−1942 and 4C+41.17) and 3.0 for the rest. These S/N thresholds are established so that the number of possible sources is maximized, while minimizing the number of false detections (noise peaks). Fig. 3 and Appendix A show that a reasonably low percentage (∼8–24 per cent) of sources with S/N above these defined thresholds could be false positive peaks. Therefore, we considered these limits appropriate since the number of source candidates decreases significantly if higher (lower) thresholds (FDRs) are selected.

Table 3 shows the source catalogue for the PKS1138-262 field. This list is in decreasing order of S/N and includes the measured 1.1 mm flux densities and their deboosted fluxes (Section 5.1). Catalogues for the other ACES protoclusters can be found in Appendix A.

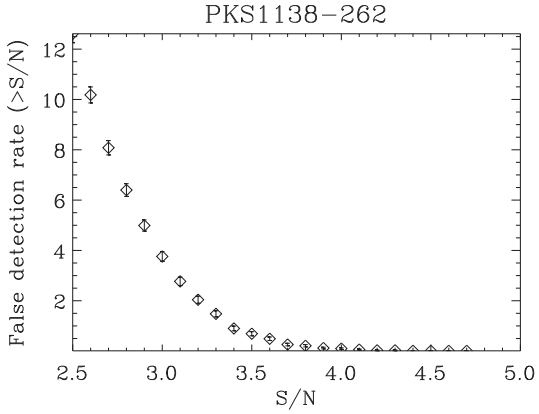


**Figure 3.** Expected number of false detections as a function of limiting S/N produced by jackknifing the timestream data towards the field of PKS1138−262. Error bars denote 68 per cent intervals for a Poisson distribution. There are 47 detections in this field with S/N >3, and according to the plot, at most four of these sources are false detections.

### 4.3 Number of false detections

Given the modest S/N of the source candidates, some fraction of the AzTEC sources are expected to be spurious. We identify the number of source detections extracted from the set of noise-only realizations, produced by jackknifing the timestream data of each protocluster field, in order to estimate the number of positive noise peaks that the source detection algorithm would pick up as source candidates. The expected number of false detections as a function of limiting S/N is shown in Fig. 3 for the field towards PKS1138−262. Appendix A shows similar plots for the rest of the sample.

These false detection rates (FDRs) are only upper limits, since the number of high-significance positive noise peaks in the signal map decreases because of the existence of real sources, which causes a negative bias in the pixel flux-density distribution of the signal map due to the negative side lobes of the point-source kernel. This effect was first demonstrated for the AzTEC/GOODS-N survey (Perera et al. 2008) and determined to be particularly strong for maps like ours, with depths below the confusion limit (Scott et al. 2010).

### 4.4 Completeness

The detection probability for a given source is affected by both Gaussian random noise and confusion noise from the underlying faint sources. To account for both effects, map completeness is estimated by injecting a total of 1000 fake sources per flux bin (ranging from 0.5 to 20 mJy), one at a time, into the signal map at random positions, and then checking if they are retrieved by the source identification algorithm of Section 4.2. Adding one source at a time to the signal map provides a valid estimate of the completeness because it accounts for the effects of both random and confusion noise present in the signal map (Scott et al. 2010). The input positions are restricted to be farther than 17 (10) arcsec from any real source in the ASTE (JCMT) maps, and real sources are defined as having S/N >4 in the shallowest maps (TNJ1338−1942 and 4C+41.17) and S/N >3.5 in the rest. Otherwise, the result could be biased because the detection algorithm cannot distinguish between two sources that close. Fig. 4 shows the map completeness for the field towards PKS1138−262. The plots for the rest of the sample are shown in Appendix A.

**Table 3.** AzTEC source catalogue for the field of PKS1138−262. The columns show: (1) source ID; (2) source name; (3) S/N of the detection; (4) measured 1.1 mm flux density and error; (5) deboosted 1.1 mm flux density and 68 per cent confidence interval; and (6) probability for the source to have a negative deboosted flux. The catalogue is limited to sources detected at an S/N >3 within 50 per cent coverage region of the AzTEC map. There are 47 detections, and according to the FDR upper limit estimated in Fig. 3, at most four of these sources could be false (8 per cent). Nevertheless, all sources show a probability of having a negative deboosted flux <0.05. Therefore, all of them are considered for the source-count analysis in Section 5.

| ID | IAU name | S/N | $S_{1.1\mathrm{mm}}$ (measured) (mJy) | $S_{1.1\mathrm{mm}}$ (deboosted) (mJy) | $P(<0)$ |
|---|---|---|---|---|---|
| 1 | MMJ114059.25−263038.40 | 16.09 | $11.4 \pm 0.7$ | $11.1^{+0.7}_{-0.7}$ | 0.000 |
| 2 | MMJ114103.73−263340.90 | 10.41 | $7.6 \pm 0.7$ | $7.2^{+0.7}_{-0.7}$ | 0.000 |
| 3 | MMJ114059.72−263155.49 | 10.10 | $7.1 \pm 0.7$ | $6.7^{+0.8}_{-0.7}$ | 0.000 |
| 4 | MMJ114043.85−262340.86 | 9.88 | $7.7 \pm 0.8$ | $7.2^{+0.8}_{-0.8}$ | 0.000 |
| 5 | MMJ114046.73−262538.01 | 9.60 | $6.8 \pm 0.7$ | $6.5^{+0.7}_{-0.8}$ | 0.000 |
| 6 | MMJ114052.55−262917.09 | 9.45 | $6.9 \pm 0.7$ | $6.5^{+0.7}_{-0.8}$ | 0.000 |
| 7 | MMJ114051.88−263516.75 | 9.24 | $7.6 \pm 0.8$ | $7.1^{+0.8}_{-0.8}$ | 0.000 |
| 8 | MMJ114047.42−262910.76 | 8.41 | $6.2 \pm 0.7$ | $5.8^{+0.7}_{-0.8}$ | 0.000 |
| 9 | MMJ114044.52−262207.98 | 7.97 | $7.5 \pm 0.9$ | $6.9^{+0.9}_{-1.0}$ | 0.000 |
| 10 | MMJ114033.54−263120.28 | 7.64 | $5.5 \pm 0.7$ | $5.1^{+0.7}_{-0.7}$ | 0.000 |
| 11 | MMJ114108.87−263422.79 | 7.47 | $5.9 \pm 0.8$ | $5.5^{+0.8}_{-0.8}$ | 0.000 |
| 12 | MMJ114101.65−262347.14 | 7.16 | $5.7 \pm 0.8$ | $5.2^{+0.8}_{-0.8}$ | 0.000 |
| 13 | MMJ114113.33−263259.16 | 6.68 | $5.3 \pm 0.8$ | $4.8^{+0.8}_{-0.8}$ | 0.000 |
| 14 | MMJ114102.20−262732.21 | 5.60 | $4.0 \pm 0.7$ | $3.6^{+0.7}_{-0.8}$ | 0.000 |
| 15 | MMJ114031.13−262240.44 | 5.58 | $5.0 \pm 0.9$ | $4.3^{+0.9}_{-0.9}$ | 0.000 |
| 16 | MMJ114019.41−263146.52 | 5.58 | $4.9 \pm 0.9$ | $4.2^{+0.9}_{-0.9}$ | 0.000 |
| 17 | MMJ114056.79−262644.48 | 5.12 | $3.6 \pm 0.7$ | $3.2^{+0.7}_{-0.8}$ | 0.000 |
| 18 | MMJ114038.43−263152.74 | 4.92 | $3.5 \pm 0.7$ | $3.0^{+0.7}_{-0.7}$ | 0.000 |
| 19 | MMJ114034.01−263505.27 | 4.91 | $4.0 \pm 0.8$ | $3.4^{+0.8}_{-0.8}$ | 0.000 |
| 20 | MMJ114023.25−263022.29 | 4.62 | $3.6 \pm 0.8$ | $3.1^{+0.8}_{-0.8}$ | 0.000 |
| 21 | MMJ114058.35−263450.33 | 4.60 | $3.6 \pm 0.8$ | $3.0^{+0.8}_{-0.8}$ | 0.000 |
| 22 | MMJ114041.40−262544.02 | 4.60 | $3.2 \pm 0.7$ | $2.7^{+0.7}_{-0.7}$ | 0.000 |
| 23 | MMJ114111.53−263610.73 | 4.52 | $4.6 \pm 1.0$ | $3.6^{+1.0}_{-1.0}$ | 0.000 |
| 24 | MMJ114108.41−262410.87 | 4.46 | $3.5 \pm 0.8$ | $2.9^{+0.8}_{-0.8}$ | 0.000 |
| 25 | MMJ114020.39−262825.87 | 4.45 | $3.8 \pm 0.9$ | $3.1^{+0.9}_{-0.8}$ | 0.000 |
| 26 | MMJ114032.18−263243.43 | 4.32 | $3.1 \pm 0.7$ | $2.6^{+0.7}_{-0.7}$ | 0.000 |
| 27 | MMJ114120.90−262622.62 | 4.24 | $4.1 \pm 1.0$ | $3.2^{+0.9}_{-1.0}$ | 0.001 |
| 28 | MMJ114111.07−263452.90 | 4.20 | $3.6 \pm 0.9$ | $2.8^{+0.9}_{-0.9}$ | 0.001 |
| 29 | MMJ114016.13−263105.22 | 4.20 | $4.1 \pm 1.0$ | $3.2^{+1.0}_{-1.0}$ | 0.001 |
| 30 | MMJ114057.47−262940.84 | 4.08 | $2.9 \pm 0.7$ | $2.4^{+0.7}_{-0.7}$ | 0.001 |
| 31 | MMJ114042.27−262710.52 | 4.05 | $2.9 \pm 0.7$ | $2.3^{+0.7}_{-0.7}$ | 0.001 |
| 32 | MMJ114024.41−262807.92 | 4.04 | $3.1 \pm 0.8$ | $2.5^{+0.8}_{-0.8}$ | 0.001 |
| 33 | MMJ114109.50−262237.90 | 3.82 | $3.6 \pm 0.9$ | $2.7^{+0.9}_{-1.0}$ | 0.003 |
| 34 | MMJ114118.70−263349.80 | 3.66 | $3.5 \pm 1.0$ | $2.5^{+1.0}_{-1.0}$ | 0.005 |
| 35 | MMJ114048.08−263314.27 | 3.61 | $2.6 \pm 0.7$ | $2.0^{+0.8}_{-0.7}$ | 0.003 |
| 36 | MMJ114021.69−263523.07 | 3.59 | $3.5 \pm 1.0$ | $2.5^{+1.0}_{-1.0}$ | 0.006 |
| 37 | MMJ114112.46−263023.03 | 3.58 | $2.8 \pm 0.8$ | $2.1^{+0.8}_{-0.8}$ | 0.004 |
| 38 | MMJ114046.48−263420.19 | 3.57 | $2.7 \pm 0.8$ | $2.1^{+0.8}_{-0.8}$ | 0.004 |
| 39 | MMJ114024.87−262519.63 | 3.56 | $2.8 \pm 0.8$ | $2.2^{+0.8}_{-0.8}$ | 0.004 |
| 40 | MMJ114112.65−262508.13 | 3.53 | $2.8 \pm 0.8$ | $2.1^{+0.8}_{-0.8}$ | 0.005 |
| 41 | MMJ114026.19−262910.95 | 3.49 | $2.6 \pm 0.8$ | $2.0^{+0.8}_{-0.8}$ | 0.005 |
| 42 | MMJ114026.84−263535.05 | 3.44 | $3.2 \pm 0.9$ | $2.2^{+1.0}_{-0.9}$ | 0.008 |
| 43 | MMJ114018.60−262422.91 | 3.32 | $3.2 \pm 1.0$ | $2.2^{+1.0}_{-1.0}$ | 0.013 |
| 44 | MMJ114026.15−263343.76 | 3.32 | $2.6 \pm 0.8$ | $1.9^{+0.8}_{-0.8}$ | 0.009 |
| 45 | MMJ114048.26−262740.46 | 3.19 | $2.3 \pm 0.7$ | $1.7^{+0.7}_{-0.8}$ | 0.011 |
| 46 | MMJ114108.01−263532.23 | 3.08 | $2.7 \pm 0.9$ | $1.8^{+0.9}_{-0.9}$ | 0.020 |
| 47 | MMJ114106.83−262519.65 | 3.02 | $2.2 \pm 0.7$ | $1.5^{+0.8}_{-0.7}$ | 0.018 |

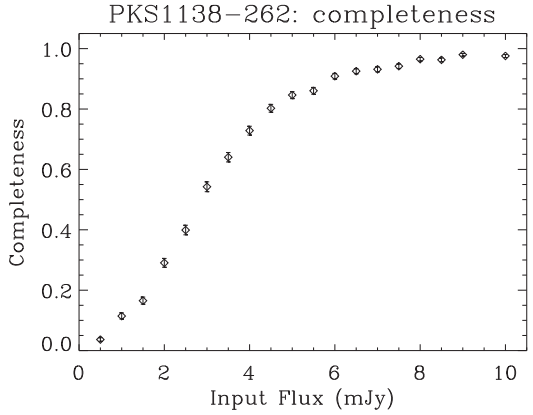


**Figure 4.** Completeness estimation for AzTEC sources in the ACES protocluster field towards PKS1138−262. The data points and 68 per cent confidence binomial error bars show the completeness estimated by inserting sources of known flux density one at a time into the real signal map. From the image, it can be seen that for sources with flux densities >4 mJy the completeness is >60 per cent. According to noise properties of the PKS1138−262 map, sources with S/N > 3 have flux densities >2.1 mJy.

### 4.5 Astrometry

Although ACES observations have been corrected for small pointing errors by periodically targeting well-known bright point sources, there is a possibility of a remaining systematic offset in the maps. Without very bright objects on each of the ACES protocluster fields to use as pointing references, or a large catalogue of fainter objects (with high positional certainty such as radio sources) to do individual stacking analysis on each of the signal maps, an overall pointing offset is estimated applying a similar technique as in Wilson et al. (2008b). For the ASTE maps, we averaged the positional offsets of the nine RGs detected at 1.1 mm; and for the single JCMT map, we averaged positional offsets of three AzTEC sources previously observed with submm interferometry (Submillimeter Array, i.e. SMA, follow-up program, PI: D. H. H.) and the central RG 4C+41.17.

The top panel of Fig. 5 shows the measured offsets in right ascension and declination for the nine ASTE RGs. The thick circle represents the mean pointing offset ($\Delta$RA = −2.8 arcsec and $\Delta$Dec. = −2.3 arcsec) and 1$\sigma$ error bars (1.6 arcsec in RA and Dec.). This is consistent with no systematic pointing error and therefore no correction was applied. The bottom panel of Fig. 5 shows the measured offsets for the three SMGs detected with SMA and the central RG in the JCMT map. Again, the thick circle represents the mean pointing offset ($\Delta$ RA = −0.5 arcsec and $\Delta$ Dec. = −1.9 arcsec) and 1$\sigma$ error bars (1.2 arcsec in RA and Dec.), and no correction was applied.

Random and confusion noise is another source of positional uncertainty. It can cause the peak of a detection to move away from its original location. This effect is considerably notorious for large beam surveys and depends on the S/N ratio of the detection (e.g. Ivison et al. 2007). We perform simulations for each ACES protocluster field to determine the probability for a certain source to be displaced some arcseconds away from its original location. The simulations consist of inserting sources with known flux densities in the signal map (one at a time) and determining how many arcseconds away they are recovered by the source detection algorithm. We repeat this procedure 1000 times for different flux-density bins in the range of 1–20 mJy to obtain a distribution of input-to-output source distances as a function of detected S/N. The probability $P$ ($>\theta$; S/N) that a source will be detected outside of a radial distance

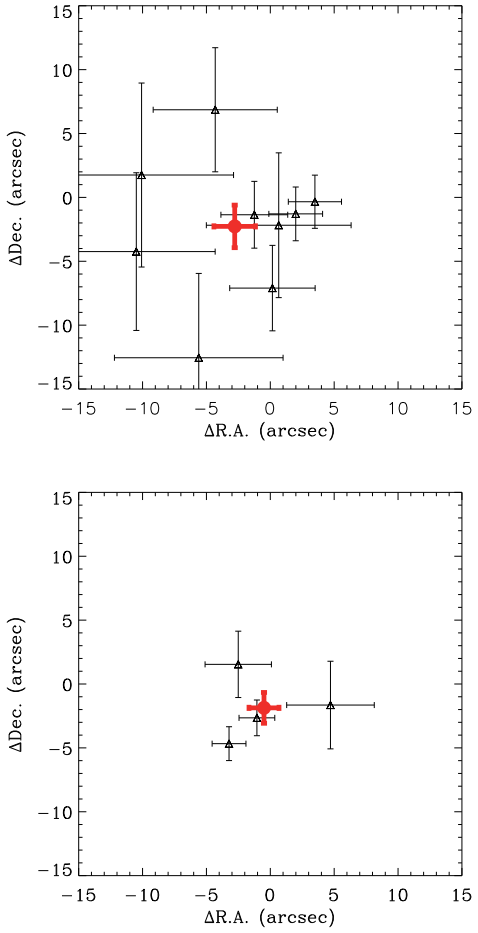


**Figure 5.** Top: measured pointing offsets in right ascension and declination for nine RGs detected at 1.1 mm with ASTE. Errors bars represent their positional uncertainties. The thick circle marks the pointing offset and its positional uncertainty estimated by averaging the RGs offsets. No systematic pointing error was found and therefore no correction was applied. Bottom: measured pointing offsets for three SMGs detected with SMA and the central RG in the 4C+41.17 map taken with the JCMT. The thick circle represents the mean pointing offset and its positional uncertainty. Again, no systematic pointing error was found and therefore no correction was applied.

$\theta$ of its true position in our map towards PKS1138−262 is shown in Fig. 6. The different symbols show results for three different S/N bins.

Ivison et al. (2007) derived an analytical expression for the positional uncertainty of low-S/N sources and found good agreement with the distribution of positional errors measured for the population of submm sources in the Submillimetre Common-User Bolometer Array Half Degree Extragalactic Survey (SCUBA/SHADES) that had radio counterparts. They reported Gaussian profiles for the RA and Dec. uncertainties, with $\sigma$ equal to $\Delta\alpha = \Delta\delta = 0.6 \times \mathrm{FWHM} \times \mathrm{S/N}^{-1}$, where $\Delta\alpha$ and $\Delta\delta$ represent RA and Dec. uncertainties, respectively, FWHM the full width at half-maximum of the beam, and S/N the signal-to-noise ratio of the submm source. Thus, the radial offsets follow a profile of the form $\theta e^{-\theta^2/2\sigma^2}$, for which 68 per cent (95.6 per cent) of offsets are expected to lie within 1.51$\sigma$ (2.5$\sigma$). To check whether our ACES positional uncertainties are consistent with this theoretical expectation, the cumulative probability of the radial offsets is overplotted in Fig.6 for the same S/N bins given the size of the ASTE beam. The curves show that the analytical expression and the empirical distributions follow roughly the same

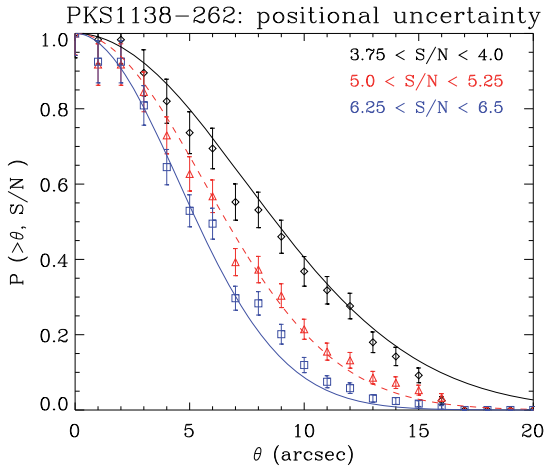


**Figure 6.** Positional uncertainty distribution for PKS1138−262 source candidates. The data points and error bars show the probability $P(>\theta; \mathrm{S/N})$ that a source detected with a given S/N ratio will be found outside a radial distance $\theta$ from its true location. The curves show the corresponding analytical expression derived in Ivison et al. (2007).

trend. The positional uncertainty distributions for the other ACES protocluster maps can be found in Appendix A.

## 5 SOURCE COUNTS

### 5.1 Flux deboosting

Our AzTEC maps are characterized by low S/N detections and an underlying flux-density distribution of sources whose estimated counts have a steep shape (Scott et al. 2012). Therefore, sources blindly detected in these maps have measured flux densities biased towards higher values (i.e. flux boosting, Hogg & Turner 1998). This can be corrected by constructing the full posterior flux-density distribution (PFD) for each source taking as a prior the parameters for a Schechter function that best characterizes the underlying distribution of sources. We use $N_{3\mathrm{mJy}} = 230\ \mathrm{deg}^{-2}$, $S^{'} = 1.7$ mJy, and $\alpha = -2.0$, which are the parameters measured for the source counts of SMGs at 1.1 mm towards blank fields (Scott et al. 2012).

PFDs are derived for all $>2.5\sigma$ peaks in the ASTE (JCMT) catalogues, and source candidates are selected from this sample if their PFDs show <5 per cent (<10 per cent) probability of having negative intrinsic flux density. The 5 per cent threshold has been traditionally used in previous SCUBA (Coppin et al. 2006) and AzTEC surveys (Perera et al. 2008; Austermann et al. 2009) to limit the number of false detections to a near negligible amount. For our JCMT field, however, a 5 per cent threshold would limit the AzTEC source candidate list to just those with S/N >3.7. Austermann et al. (2010) verified through simulations that the use of a higher threshold supplies additional data without introducing any significant biases in the number counts analysis. Therefore, we increase the threshold to 10 per cent for this particular field.

Since we are using a blank-field prior in fields where overdensities are expected, we examine how dependent the PFD estimation is on the prior. We found that PKS1138−262 is the ACES protocluster field that, on average, has the most deviant source counts with respect to the AzTEC blank-field data we discuss this point further in Section 5.3. We estimated its overdensity to be as high as 2 by determining the difference, per flux bin, between the differential source counts in the protocluster field and the reference field, and calculating the mean difference for all bins. Then, we used twice the source counts estimated for the AzTEC blank-field data as a prior to determine new PFDs for all the ACES-protocluster sources, and found that the variation in the estimated deboosted fluxes is, on average, 7 ± 3 per cent for sources with 3 < S/N <4.0. These flux-density changes are smaller than the deboosted flux errors, therefore the flux densities estimated with the initial prior are considered good estimates of the intrinsic flux densities of ACES sources.

The deboosted flux densities are listed in column 5 of the ACES protocluster catalogues of Table 3 and Appendix A.

### 5.2 AGN counterparts

Since we are interested in the number density of SMGs around the ACES AGN, we need to remove possible 1.1 mm counterparts to the active galaxies from our catalogues. We follow a similar approach as in Humphrey et al. (2011) and use the AGN coordinates that are most accurate as determined from radio, optical, or mid(near)-IR data. These coordinates are the most likely to mark the position of the radio core. For AGN with no detected radio cores, the preference is to use the centroid of the emission averaged across the 3.6 and 4.5 μm bands, taken by the Infrared Array Camera (IRAC) on board the *Spitzer Space Telescope* (Fazio et al. 2004). If these data are not available either, the longest wavelength detection in the optical or near-IR is used instead (Table 1). Then, we select the closest AzTEC source that has an S/N >2.5 and whose PFD has a probability of having negative intrinsic flux less than the threshold established in the previous section. Humphrey et al. (2011), on the other hand, adopt a selection criteria based only on an S/N ≥3.0. Both approaches minimize the possibility of assigning false detections as AGN counterparts with similar results, and both find possible 1.1 mm detections to 10 ACES AGN. In the case of TNJ2007−1316, however, the closest AzTEC source is a marginal detection with an S/N = 3.0, but a 5.9 per cent probability of having negative flux. Therefore, it is considered a false positive by us but regarded as counterpart by Humphrey et al. (2011).

Once the possible mm counterpart is identified at a certain distance $\theta$, we use the theoretical approach of Ivison et al. (2007), which is in good agreement with the positional uncertainty distributions found in Section 4.5, to estimate the probability for this counterpart to have been moved a distance $>\theta$ due to confusion and random noise (i.e. $P(>\theta; \mathrm{S/N})$). If that probability is ≤5 per cent, then the mm detection is discarded as the possible AGN counterpart. As can be seen from Table 4, 10 AGNs have possible mm counterparts in the deboosted catalogues.

In addition, we use the *P-statistic*, $P(r) = 1 - \mathrm{e}^{-n\pi r^2}$, to determine whether the possible mm counterpart is associated with the AGN only by chance (Downes et al. 1986). For $n$ we use the surface density of mm sources, as determined from the AzTEC blank-field number counts, that have 1.1 mm flux densities greater than or equal to that of the possible counterpart. We assume a blank field population, despite the fact that the environments of our AGN sample possibly contain source clustering or overdensity, because our goal is to find the probability of random association between the AGN and a foreground/background SMG, whose population is better described by a blank-field distribution of sources. The AGN-mm association is considered to be random when $P >$ 5 per cent. As can be seen from Table 4, each of the 10 previously selected mm counterparts for the AGN are not likely to be random associations.

**Table 4.** Possible AGN counterparts at 1.1 mm: (1) AGN name; (2) and (3) RA and Dec. coordinates of the closest mm source; (4) S/N of the mm source, (5) distance between the AGN and their closest mm source; (6) probability for the mm source to have been moved a distance $>\theta$ due to random and confusion noise; and (7) probability for the mm source to be randomly associated to the AGN (*P*-statistics). Rows highlighted in bold mark AGN with likely mm counterparts.

| AGN | Closest 1.1-mm source | | | | | |
|---|---|---|---|---|---|---|
| AGN name | RA (J2000) (deg) | Dec. (J2000) (deg) | S/N | $\theta$ (arcsec) | $P(>\theta;$ S/N) (per cent) | *P*-stat (per cent) |
| SDSSJ1030+0524 | 10:30:26.68 | +05:25:15.98 | 6.2 | 21.9 | 00.0 | 3.1 |
| **TNJ0924−2201** | **09:24:20.31** | **−22:01:28.95** | **4.0** | **13.8** | **11.4** | **1.6** |
| TNJ1338−1942 | 13:38:27.35 | −19:42:25.66 | 6.3 | 17.7 | 00.0 | 0.3 |
| TNJ2007−1316 | 20:07:51.03 | −13:15:29.15 | 4.0 | 80.9 | 00.0 | 42.2 |
| **4C+41.17** | **06:50:51.93** | **+41:30:33.04** | **3.5** | **5.0** | **35.7** | **0.4** |
| **TNJ2009−3040** | **20:09:48.89** | **−30:40:03.16** | **3.6** | **11.3** | **18.1** | **1.5** |
| MRC0316−257 | 03:18:13.14 | −25:35:08.26 | 5.5 | 13.6 | 00.3 | 1.1 |
| **PKS0529−549** | **05:30:25.20** | **−54:54:22.02** | **9.7** | **2.4** | **53.4** | **0.0** |
| **MRC2104−242** | **21:06:58.32** | **−24:05:15.96** | **4.3** | **8.2** | **23.7** | **0.5** |
| 4C+23.56 | 21:07:15.63 | +23:31:33.16 | 7.7 | 16.3 | 00.0 | 0.9 |
| PKS1138−262 | 11:40:47.42 | −26:29:10.75 | 8.4 | 12.6 | 00.0 | 0.2 |
| **MRC0355−037** | **03:57:48.05** | **−03:34:02.40** | **6.1** | **7.1** | **10.8** | **0.1** |
| **MRC2048−272** | **20:51:04.24** | **−27:03:05.45** | **3.0** | **10.2** | **36.3** | **2.6** |
| **TXS2322−040** | **23:25:10.19** | **−03:44:44.52** | **3.6** | **2.3** | **92.5** | **0.1** |
| MRC2322−052 | 23:25:18.38 | −04:57:27.48 | 3.34 | 20.5 | 00.4 | 8.6 |
| **MRC2008−068** | **20:11:13.99** | **−06:44:03.26** | **9.8** | **3.4** | **27.1** | **0.0** |
| **MRC2201−555** | **22:05:04.97** | **−55:17:42.64** | **7.8** | **1.8** | **79.8** | **0.0** |

**Table 5.** Differential and integrated source counts calculated for the ACES field towards PKS1138−262.

| Flux density (mJy) | d$N$/d$S$ (mJy$^{-1}$ deg$^{-2}$) | Flux density (mJy) | $N(>S)$ (deg$^{-2}$) |
|---|---|---|---|
| 1.4 | $1400^{+370}_{-450}$ | 1.0 | $2700^{+410}_{-500}$ |
| 2.4 | $730^{+170}_{-210}$ | 2.0 | $1320^{+220}_{-230}$ |
| 3.4 | $270^{+77}_{-99}$ | 3.0 | $590^{+110}_{-120}$ |
| 4.4 | $100^{+38}_{-53}$ | 4.0 | $314^{+68}_{-87}$ |
| 5.4 | $71^{+29}_{-42}$ | 5.0 | $213^{+51}_{-77}$ |
| 6.4 | $68^{+28}_{-40}$ | 6.0 | $142^{+40}_{-57}$ |
| 7.4 | $44^{+20}_{-32}$ | 7.0 | $73^{+29}_{-41}$ |
| 8.4 | $10^{+9}_{-10}$ | 8.0 | $28^{+13}_{-25}$ |

### 5.3 Source counts for individual fields

Once the possible counterparts to the ACES AGN are removed from the catalogues, we derive estimates for the number density of SMGs as a function of flux density using the Bayesian technique originally outlined in Coppin et al. (2005, 2006) and used extensively in previous AzTEC publications (e.g. Austermann et al. 2009, 2010; Aretxaga et al. 2011; Scott et al. 2012). The PFDs of the source candidates are randomly sampled (with replacement) to determine their intrinsic flux densities. They are sampled 20 000 times and the mock sources are binned by their flux density (bin size =1 mJy). Each bin in each iteration is then corrected for incompleteness. The source counts are calculated as the mean number of sources in each bin over the 20 000 iterations, and the uncertainties represent the 68 per cent confidence intervals calculated from the distribution in the counts across those iterations. For the differential counts, the flux densities are the effective bin centres weighted by the assumed prior, and for the integrated counts, the flux densities are the bin edges with the lowest flux density.

Table 5 and Fig. 7 show the 1.1 mm differential and integrated source counts derived for the field towards PKS1138−262. Appendix A shows similar plots and tables for the rest of the sample. As can be seen from the graphs, the counts from different fields show a lot of variance, especially when extreme cases such as PKS1138−262 and TNJ1338−1942 are compared. A look at the 4-mJy flux-density bin, which is above the average 3$\sigma$ detection level for all ACES maps, allow a fair comparison among fields with different noise levels. The significant scattering observed in this flux-density bin (and in higher flux-density bins) could be explained by a combination of sample variance, which largely affects small-size maps like these ones, and intrinsic clustering variations. According to the AzTEC blank-field source counts (Scott et al. 2012), ∼9 sources with $S_{1.1\mathrm{mm}} > 4$ mJy are expected to populate maps as large as ∼200 sq arcmin (∼7 in the case of the smaller 166-sq-arcmin map of 4C+23.56 and ∼13 in the case of the larger 303-sq-arcmin map of 4C+41.17). In 14 of the 17 ACES maps, the number of sources with $S_{1.1\mathrm{mm}} > 4$ mJy fall within the 95 per cent confidence interval of a Poisson probability distribution of the blank-field counts (Fig. 8). Therefore, sample variance cannot be ruled out as being the dominant effect on the large scattering observed in the individual counts.

In the fields towards 4C+23.56, PKS1138−262, and MRC0355−037, however, the numbers of sources with $S_{1.1\mathrm{mm}} >$ 4 mJy exceeds the number of expected sources in a blank field by a factor of ∼2. The significance of these overdensities is $>3\sigma$, which means that the probability of finding overdensities like these ones by chance is <0.3 per cent.

In order to reduce field-to-field scattering and improve the statistical significance of any overdensity result, the source-counts analysis is repeated with all the ACES protocluster fields combined.

### 5.4 Source counts for the combined fields

All 17 catalogues and completeness estimations are combined to produce a single study of the ACES protocluster source counts based on a total surveyed area of 1.01 sq deg. The differential and integrated counts are determined applying the same technique explained in Section 5.3 but taking into account that completeness depends on noise level and it is different for each field. The

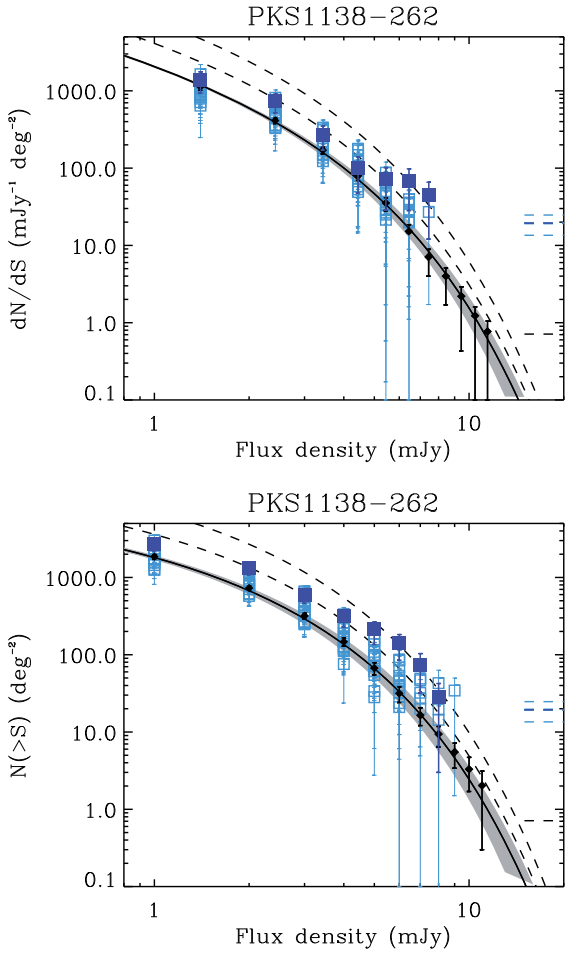


**Figure 7.** AzTEC 1.1 mm differential and integrated source counts for the field of PKS1138−262 (solid squares). Source counts for the AzTEC blank fields used as reference are also shown (diamonds; Scott et al. 2012). The solid line and grey shading represent the best fit of a Schechter function to the reference counts and its 68 per cent confidence interval. Overplotted in light colour are the counts for the other 16 ACES protocluster fields. This is to show the scattering in the data that is mainly due to sample variance. Dashed lines show twice and four times the reference-field density of sources. Horizontal dashed lines represent the survey limit, defined as the source density (inside the map area) that will Poisson deviate to zero sources 32 per cent of the time.

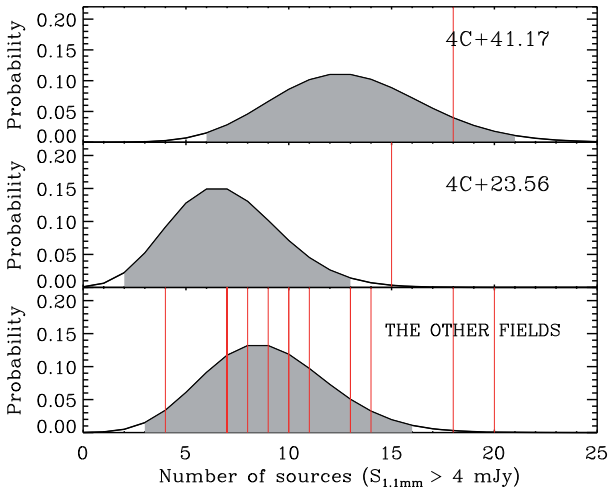


**Figure 8.** Poisson probability distributions of the number of sources with $S_{1.1\mathrm{mm}} > 4$ mJy expected for blank-field maps with sizes similar to the ACES protocluster maps. The 95 per cent confidence intervals are represented by grey shaded areas. Since not all the ACES maps have similar sizes, the probability distributions that correspond to the 4C+41.17 (area = 303 sq arcmin) and the 4C+23.56 (area = 166 sq arcmin) maps are plotted separately. The probability distribution for the rest of the protocluster maps, which have individual areas of ∼200 sq arcmin, is plotted at the bottom of the image. The numbers of sources found in each protocluster map are plotted as vertical lines. 14 of the 17 ACES fields show number of sources falling within the 95 per cent confidence interval of their corresponding blank-field data. Therefore, sample variance cannot be ruled out as being the dominant effect on the large scattering observed in the individual number counts of Fig. 7. Fields whose numbers of sources with $S_{1.1\mathrm{mm}} > 4$ mJy that exceed their 95 per cent confidence intervals are 4C+23.56, PKS1138−262, and MRC0355−037.

differential and cumulative counts from the combined biased fields are listed in Table 6, together with their 68 per cent confidence interval uncertainties.

In order to find out if there is an overdensity of mm sources around the AGN, we compare the ACES protocluster source counts to the ones of the AzTEC blank fields (Fig. 9). Overall, the combined ACES protocluster counts (circles) lie very close to the AzTEC blank-field estimation (diamonds). Since the surveyed area for the ACES protocluster project was nearly 1 sq deg, it is possible that if there was an overdensity spanning a few Mpc (a few arcmin) from the centre of the protocluster maps, it was diluted while estimating an average source density in a larger area (see Section 5.6). For instance, previous submm surveys around AGNs (e.g. Stevens et al. 2003; Priddey et al. 2008; Stevens et al. 2010) have claimed overdensity detections of ∼2–4 in areas of ∼1.5-arcmin radius (SCUBA field of view).

**Table 6.** Combined differential and integrated source counts for the 17 ACES protocluster fields.

| Flux density (mJy) | d$N$/d$S$ (mJy$^{-1}$ deg$^{-2}$) | Flux density (mJy) | $N$(>S) (deg$^{-2}$) |
|---|---|---|---|
| 1.4 | $1071^{+79}_{-87}$ | 1.0 | $1960^{+88}_{-96}$ |
| 2.4 | $487^{+34}_{-35}$ | 2.0 | $887^{+40}_{-42}$ |
| 3.4 | $212^{+18}_{-17}$ | 3.0 | $400^{+22}_{-23}$ |
| 4.4 | $97^{+10}_{-11}$ | 4.0 | $187^{+14}_{-15}$ |
| 5.4 | $46^{+7}_{-8}$ | 5.0 | $90^{+9}_{-10}$ |
| 6.4 | $23^{+5}_{-5}$ | 6.0 | $43^{+6}_{-7}$ |
| 7.4 | $11^{+3}_{-4}$ | 7.0 | $20^{+4}_{-5}$ |
| 8.4 | $4.7^{+1.8}_{-2.5}$ | 8.0 | $8.7^{+2.2}_{-3.4}$ |
| 9.4 | $2.1^{+1.0}_{-1.7}$ | 9.0 | $3.9^{+1.3}_{-2.1}$ |
| 10.4 | $1.2^{+0.6}_{-1.2}$ | 10.0 | $1.8^{+0.8}_{-1.3}$ |

### 5.5 Source counts at different radii from the AGN

We test the number density of SMGs in small areas around our AGN, first extracting a circle of 1.5-arcmin radius to let us conduct a direct comparison with previous studies, and then over 2 subsequent annuli between radii of 1.5 and 3 arcmin, and between 3 and 4.5 arcmin (Table 7). As can be seen in Fig. 10, source counts for the inner circle ($r < 1.5$ arcmin) are indeed larger than those of a typical blank field, even though the overdensity does not include the AGN 1.1-mm counterparts (Section 5.2). The overdensity reaches a factor $\gtrsim$3 at $S_{1.1\mathrm{mm}} \geq 4$ mJy. If we exclude the three fields that show individual

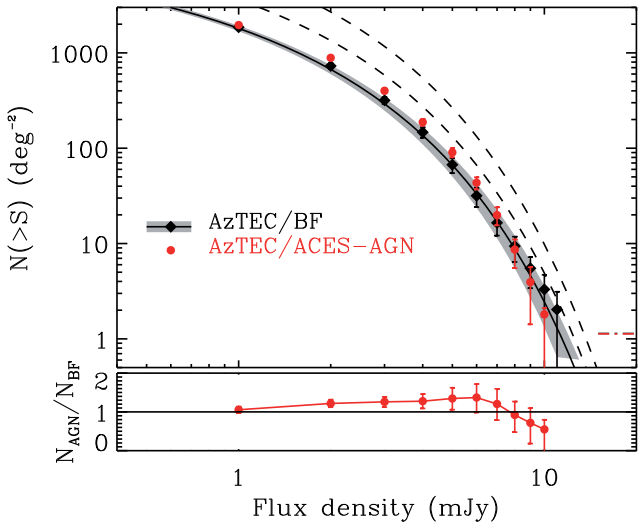


**Figure 9.** Top: AzTEC 1.1 mm integrated source counts for the combined 17 ACES protocluster fields (circles) along with the AzTEC blank-field data used as reference (diamonds). Dashed lines represent overdensities of 2 and 4 compared to the AzTEC blank-field data. The horizontal dashed line represents the survey limit. Bottom: ratio between the source counts of the ACES protocluster maps and the source counts that are predicted from the combined AzTEC blank-field data. The ACES protocluster counts lie very close to the blank-field data, which may not contradict previous studies around AGNs, since an overdensity in small areas close to the centre of the protoclusters might have been diluted while estimating an average source density in larger areas.

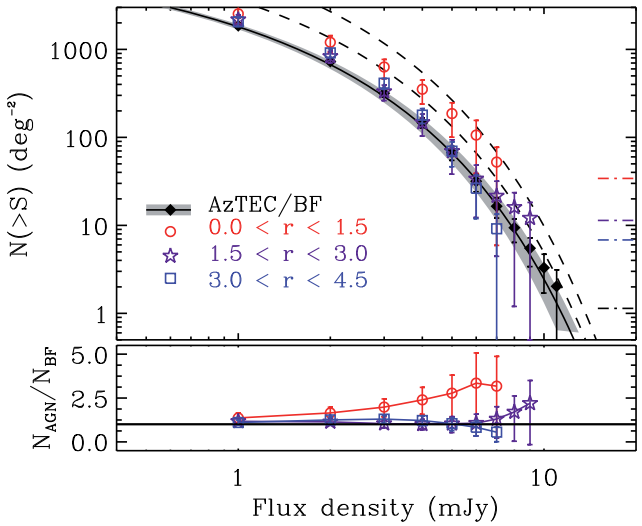


**Figure 10.** Top: AzTEC 1.1 mm integrated source counts estimated for the combined 17 ACES protocluster fields inside three different areas centred at the AGN: an inner circle of 1.5-arcmin radius (circles), and 2 annuli between radii of 1.5 and 3 arcmin (stars) and between 3 and 4.5 arcmin (squares). The AzTEC blank-field data used as reference is also plotted as solid diamonds. Beyond a radius of 1.5 arcmin, the source density looks like that of a blank field, and could be also used as a control field. Bottom: ratio between the source counts estimated for the protocluster fields inside the three chosen areas and those from the AzTEC blank-field data.

**Table 7.** Combined differential and integrated source counts for the 17 ACES protocluster fields calculated inside three different areas centred at the AGN.

| Flux density (mJy) | d$N$/d$S$ (mJy$^{-1}$ deg$^{-2}$) | Flux density (mJy) | $N(>S)$ (deg$^{-2}$) |
|---|---|---|---|
| | Circular area of 1.5-arcmin radius | | |
| 1.4 | $1335^{+441}_{-540}$ | 1.0 | $2538^{+492}_{-608}$ |
| 2.4 | $572^{+179}_{-221}$ | 2.0 | $1203^{+218}_{-279}$ |
| 3.4 | $279^{+96}_{-125}$ | 3.0 | $631^{+125}_{-170}$ |
| 4.4 | $166^{+65}_{-85}$ | 4.0 | $352^{+81}_{-116}$ |
| 5.4 | $80^{+36}_{-59}$ | 5.0 | $186^{+48}_{-78}$ |
| 6.4 | $54^{+26}_{-47}$ | 6.0 | $106^{+31}_{-51}$ |
| | Annulus between radii of 1.5 and 3.0 arcmin | | |
| 1.4 | $1344^{+262}_{-301}$ | 1.0 | $2176^{+290}_{-320}$ |
| 2.4 | $501^{+103}_{-116}$ | 2.0 | $832^{+120}_{-130}$ |
| 3.4 | $184^{+46}_{-58}$ | 3.0 | $331^{+61}_{-70}$ |
| 4.4 | $78^{+26}_{-34}$ | 4.0 | $148^{+36}_{-44}$ |
| 5.4 | $36^{+15}_{-22}$ | 5.0 | $70^{+24}_{-30}$ |
| 6.4 | $12^{+6}_{-12}$ | 6.0 | $34^{+15}_{-21}$ |
| 7.4 | $6^{+6}_{-6}$ | 7.0 | $22^{+10}_{-17}$ |
| | Annulus between radii of 3.0 and 4.5 arcmin | | |
| 1.4 | $1144^{+204}_{-206}$ | 1.0 | $2058^{+223}_{-233}$ |
| 2.4 | $500^{+75}_{-93}$ | 2.0 | $913^{+98}_{-107}$ |
| 3.4 | $234^{+43}_{-48}$ | 3.0 | $413^{+53}_{-61}$ |
| 4.4 | $109^{+25}_{-30}$ | 4.0 | $179^{+33}_{-35}$ |
| 5.4 | $43^{+14}_{-19}$ | 5.0 | $70^{+19}_{-23}$ |
| 6.4 | $17^{+8}_{-12}$ | 6.0 | $26^{+11}_{-14}$ |
| 7.4 | $8^{+4}_{-8}$ | 7.0 | $9^{+4}_{9}$ |

overdensities (4C+23.56, PKS1138−262, and MRC0355−037), we still detect a global overdensity of a factor of ∼2 at these flux densities. Beyond a radius of 1.5 arcmin, the source density looks like that of a blank field, and could be also used as a control field.

In order to estimate the significance of the overdensity found in the inner area, we construct synthetic maps with a blank-field source population for each protocluster field. This is performed by populating the noise maps with the number of sources described by the best fit of a Schechter function to the AzTEC blank-field data, properly scaled to the size of the maps, and Poisson deviated to introduce sample variance. We iteratively construct 10 000 maps for each protocluster and extract sources with flux densities >4 mJy inside circular areas of 1.5-arcmin radius placed at the centre of the maps. In each iteration, we generate a set of 17 maps corresponding to the 17 protocluster fields. We add up their number of extracted sources, and at the end, we can construct the distribution of the number of sources with flux densities >4 mJy that is characteristic of a blank field, the size of 17 circles of 1.5-arcmin radius. The source extraction is performed with the same algorithm used in the observed maps, and with a flux-density threshold rather than an S/N one because our protocluster maps have different noise levels. Since we compare the number of sources extracted from the observed maps directly to the one extracted from the synthetic maps, no deboosting or completeness correction needs to be applied. The result is shown in Fig. 11, where a vertical line denotes the 15 sources that were found in the protocluster fields. As can be seen, the probability of finding ≥15 sources with $S_{1.1\mathrm{mm}} > 4$ mJy in a blank-field area of 120 sq arcmin is 0.25 per cent, i.e. the significance of the ACES protocluster overdensity is 99.75 per cent ($\gtrsim 3\sigma$).

### 5.6 Probability of missing a compact overdensity in large maps

We also use these simulations to estimate the probability for a central overdensity of 2 to be diluted in the analysis of large maps as ours.

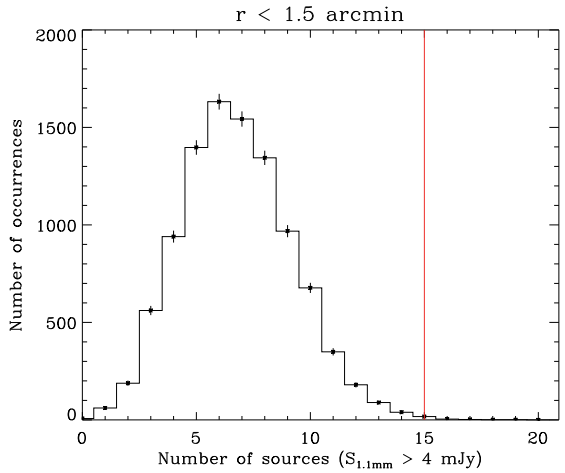


**Figure 11.** Number of sources with $S_{1.1\mathrm{mm}} > 4$ mJy extracted from the ACES protocluster maps inside an area centred on the AGN and of 1.5 arcmin radius (vertical line) compared to the distribution of the number of sources extracted from 10 000 synthetic maps with similar noise properties to the ACES maps, but populated as AzTEC blank fields (histogram). According to this distribution, the probability of finding 15 or more sources is 0.25 per cent.

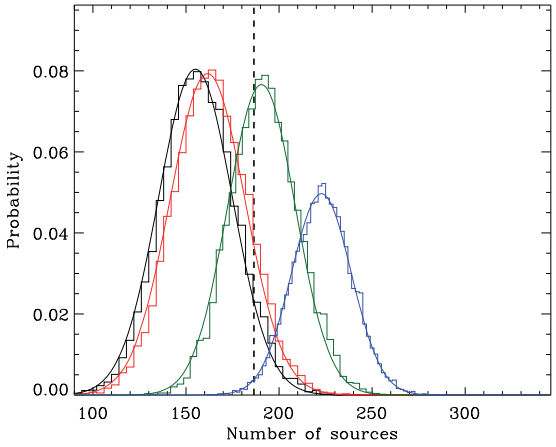


**Figure 12.** Distribution of sources with flux densities $S_{1.1\mathrm{mm}} > 4$ mJy for the 17 ACES-like synthetic maps with only a blank-field population (in black). This distribution peaks close to the 150 sources expected from the AzTEC blank-field source counts. The other three distributions are obtained from the same synthetic maps but with an inserted overdensity of 2 spatially distributed following King density profiles with $r_c = 0.3$ (in red), 0.7 (in green), and 1 (in blue) arcmin. These $r_c$ values are selected to account for overdensities with 95 per cent of the sources distributed inside radii of 1.5, 3, and 4.5 arcmin, respectively. The plot shows that 95 per cent of the time, a blank-field population is characterized by <186 sources (vertical dashed line). Therefore, the overdensity of 2 is confused with a blank field 91 per cent of the time if it is distributed following a King profile with $r_c = 0.3$ arcmin. This confusion rate decreases to 69 per cent if $r_c = 0.7$ arcmin, and continues to fall to only 4 per cent if $r_c = 1$ arcmin.

We obtain the probability distribution of the number of sources with flux densities >4 mJy found in 17 blank fields the size of our ACES protocluster maps. Then, we populate the central areas of these maps with twice the number of sources estimated for circular areas of 1.5 arcmin radius (following a King density profile with $r_c = 0.3$ arcmin, which is characterized by having 95 per cent of the sources inside a radius of 1.5 arcmin) and obtain the new probability distribution of the number of sources. Comparing these two distributions shows that 95 per cent of the time a blank-field population is characterized by <186 sources, and that the overdensity of 2 is confused with a blank field 91 per cent of the time (Fig. 12).

These simulations explain why it is not surprising that an overdensity of 2 inside a 1.5 arcmin radius of the AGN is missed when we analyse the whole 1.01 sq deg of the ACES AGN survey. In addition, it offers an explanation for the non-detection of overdensities in 14 of our ACES individual maps. The overdensities can get confused with the expected sample variance of our individual fields if they only cover a small central area.

## 6 ALIGNMENT OF SMGS AND RADIO JETS

Numerical simulations suggest that alignments occur naturally on various scales in hierarchical models of structure formation such as the ΛCDM model (e.g. Basilakos et al. 2006; Faltenbacher et al. 2008; Velliscig et al. 2015). Under this paradigm, primordial alignments along the large-scale filamentary structures can originate from a combination of different mechanisms such as tidal sheering, produced by the matter distribution around galaxies, and galaxy–galaxy interactions in the direction of the filaments.

Since SMGs are a high-redshift population, undergoing violent episodes of star formation and, as shown in the previous section, associated with protocluster candidates, they are likely to trace large-scale structure (e.g. Tamura et al. 2009; Umehata et al. 2015). Therefore, we may expect to find them preferentially forming inside the filaments feeding our cluster progenitors. Since our ACES maps cover areas with radii of ∼6–8 arcmin (Table 2), which are equivalent to comoving distances of 4–20 Mpc, we may be capable of identifying filamentary structure in them.

Although we have no redshift information for our sources, we can test whether they are randomly distributed around the AGN or aligned in a preferred direction. Sixteen of our ACES AGNs are high-redshift RGs with known jet position angles (PAs; Table 1). The direction of their radio jets is thought to be the direction of the angular momentum axis of the SMBH that drives their nuclear activity. Since the black hole spin axis may be strongly coupled to the surrounding large-scale structure (e.g. Rees 1978; Taylor & Jagannathan 2016), identifying a preferred direction for the distribution of mm sources with respect to the radio jets could be an indication of filamentary structure.

### 6.1 Principal axes

To determine if SMGs around our RGs align in a preferred direction, we find the major axis of their spatial distribution using a tool motivated by the form of the inertia tensor. Since we have no redshift information, we calculate the major axis in two dimensions. In addition, since moments of inertia are heavily dependent on the distance between the sources and the central RG, we calculate a form of reduced version (Gerhard 1983), which uses only directional information to estimate the shape of the distribution and weights sources equally regardless of their distance to the centre,

$$I = \begin{bmatrix} \sum_{i=1}^{n} \frac{x^2}{r^2} & -\sum_{i=1}^{n} \frac{xy}{r^2} \\ -\sum_{i=1}^{n} \frac{xy}{r^2} & \sum_{i=1}^{n} \frac{y^2}{r^2} \end{bmatrix}, \quad (1)$$

where $n$ is the number of sources, $r$ is the distance from the RG to the source, and $x$, $y$ are the horizontal and vertical components of

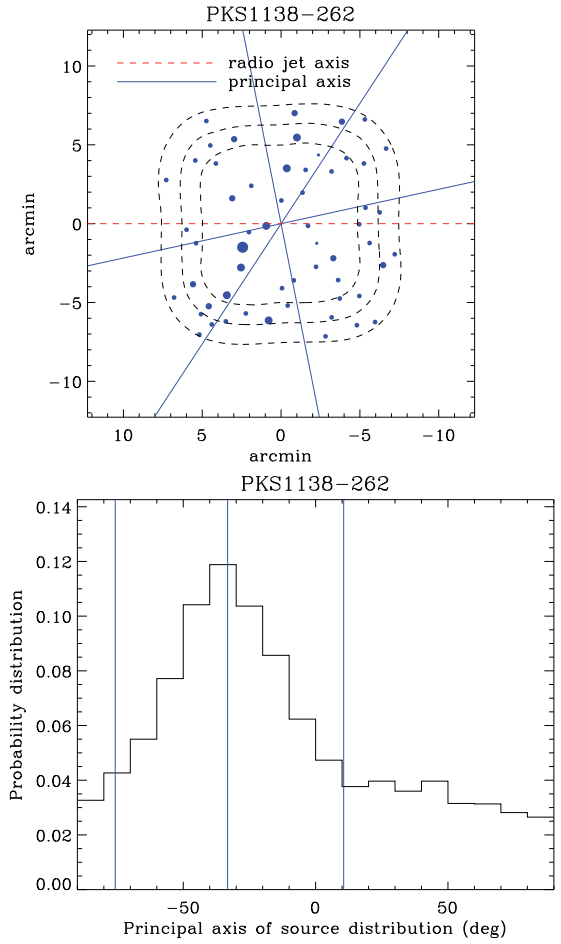


**Figure 13.** Top: position map of the AzTEC sources around the RG PKS1138−262. The circle diameter is proportional to the source S/N. The radio jet PA is obtained from the literature (Table 1) and is represented by the horizontal dashed line. The principal axis of the source distribution is determined using equation (1), motivated by the form of the inertia tensor, and is marked by the solid line. Its 68 per cent confidence interval is estimated from the bootstrapped probability distribution and is represented by the two doted–dashed lines. Both, the radio jet and the principal axis directions are measured north to east. Dashed contours show different noise levels (50 per cent, 75 per cent, and 95 per cent coverage cuts) which show no correlation with the principal axis. Bottom: principal axis probability distribution determined by bootstrapping. The vertical line marks the principal axis calculated from the source distribution and the two dotted–dashed lines the 68 per cent confidence interval.

that distance. The major axis of the distribution is defined by the major eigenvector of equation (1). We call this the *principal axis*. In order to estimate the error on this measurement, we sample the source distribution 6000 times with replacement (i.e. it is possible to sample a source more than once in each iteration) and calculate the principal axis in each iteration to produce a probability distribution of angles (bootstrapping). For all 16 fields, the peak of the distribution lies close to the *principal axis*, and it is used as starting point for the 68 per cent confidence interval estimation. The position map of SMGs around the RG PKS1138−262, together with the probability distribution of its principal axis, is plotted in Fig. 13. Appendix A shows similar plots for the rest of the sample. Angles are measured northeast.

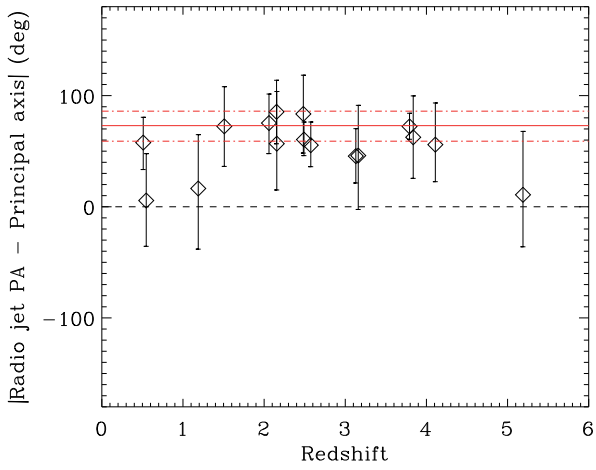


**Figure 14.** Angular difference (absolute value) between the RG jet and the principal axis of the surrounding source distribution for the 16 ACES RG fields, plotted against redshift. In most cases, the radio jet direction and the principal axis are separated more than 45 deg, although the error bars are quite large. A similar analysis using all fields is performed in Section 6.3. The result is plotted as solid and dotted–dashed horizontal lines.

### 6.2 Alignment in individual maps

PAs for the ACES RG jets were obtained from the literature and are listed in Table 1. For all RGs except two, radio images show at least two components or radio lobes. In the cases of MRC2201−555 and TNJ2009−3040, their jet PAs denote the orientation of the radio emission, since it is not symmetric. Using these angles, it is possible to estimate the angular separation between radio jets and the *principal axes* of the surrounding source distributions. Fig. 14 shows absolute values for these separations against redshift. In 13 cases, the radio jet direction and the *principal axis* are separated more than 45 deg, indicating a possible signal of misalignment, but the error bars are large. Combining the information for all the 16 fields will enhance this signal.

### 6.3 Combined analysis

The 16 RG maps are rotated so that their radio jets lie horizontally and aligned to each other. Then, all the maps are stacked at the position of the targeted RGs, and the *principal axis* and its 68 per cent confidence interval are calculated in the same manner as with the individual maps. The top part of Fig. 15 shows a position map of the stacked distribution of sources together with the radio jets (dashed line) and the principal axis (solid line) directions. As can be seen from the bottom part, the combined coverage map for the 16 ACES RG fields shows no obvious bias in the principle axis determination towards deeper map areas. The probability distribution for the *principal axis* is plotted in Fig. 16. As can be seen from the images, the principal axis is $73^{+13}_{-14}$ deg away from the radio jets direction, which makes this a $\sim 5\sigma$ detection of a misalignment. We caution the reader that all projections are measured on the plane of the sky, since we do not have redshift information for the SMGs, and that we do not expect a strong dilution of the alignment due to this projection, since the modified inertia tensor only takes into account the direction and not the distance to the AGN. However, the chances for source blending could be severe if the intrinsic alignment were perpendicular to the plane of the sky.

In order to test if there are additional biases in the way the *principal axis* is estimated, the modified tensor of inertia technique is

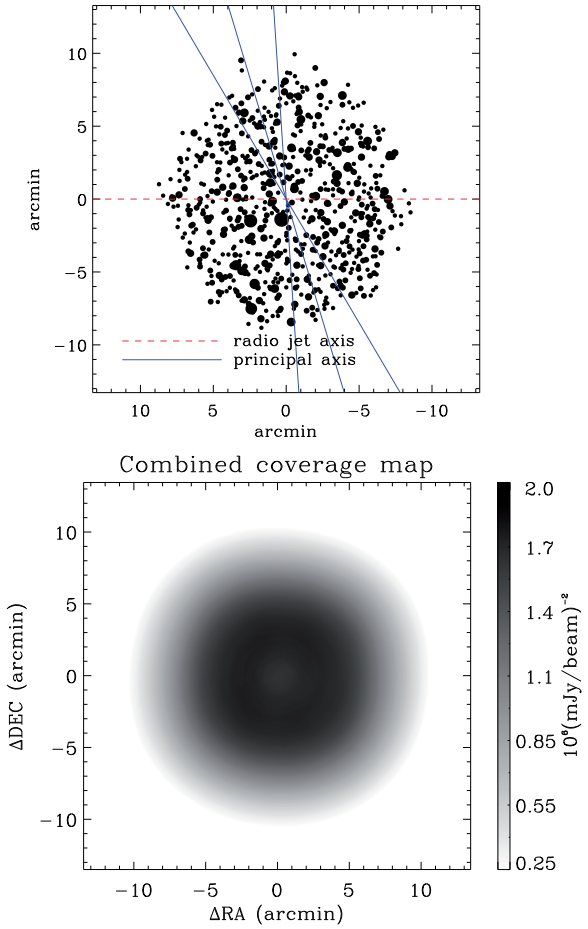


**Figure 15.** Top: principal axis for the source distribution of the stacked 16 ACES RG fields. Circles represent sources and their diameters are proportional to the S/N ratio. The dashed line represents the horizontally aligned radio jet directions, and the solid and dotted–dashed lines mark the preferred direction of the source distribution and its 68 per cent confidence interval (see Fig. 16). As can be seen, the principal axis is $73^{+13}_{-14}$ deg away from the radio jets, which makes this a $\sim 5\sigma$ detection of a misalignment. Bottom: combined coverage map for the 16 ACES RG fields that shows an isotropic coverage; and therefore, that the principle axis determination is not bias towards deeper parts of the map.

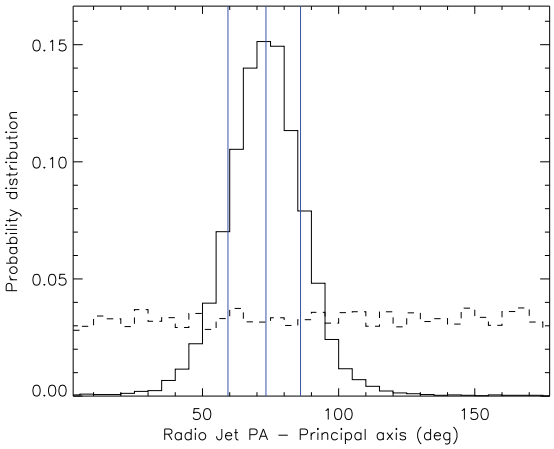


**Figure 16.** Estimated probability distribution for the difference between the principal axis of the stacked distribution of sources around the 16 ACES RG fields and the aligned radio jets (see Fig. 15). The probability distribution is represented as the solid-line histogram and was obtained by sampling the stacked source distribution with replacement. The vertical solid line represents the value found directly from the map and the dotted–dashed lines mark its 68 per cent confidence interval. The dashed-line histogram shows the corresponding probability distribution for 10 000 simulations of a 1.1 mm blank-field population randomly distributed on the same area.

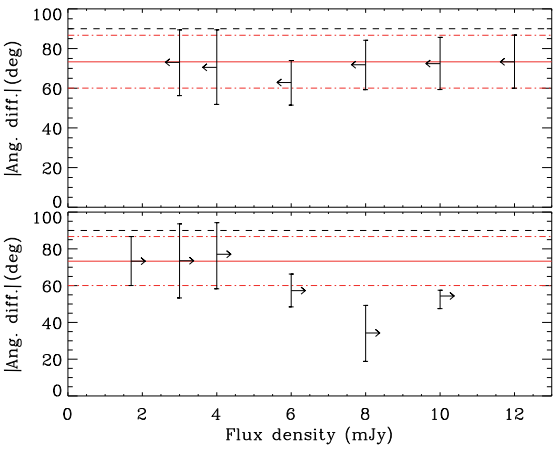


**Figure 17.** Angular differences between the aligned radio jets and the principal axes for the stacked distribution of sources around the 16 ACES RGs as a function of limiting flux density (arrows). The vertical lines are their associated error. The red horizontal lines (solid and dotted–dashed lines) represent the 73-deg principal axis found for the whole distribution of sources and its 68 per cent confidence interval, respectively. The dashed line marks 90 deg. Top: angular differences for sources with flux densities less than a certain value. When the brightest sources are gradually removed, no significant change in the misalignment is found. Bottom: angular differences for sources with flux densities greater than a certain value.

applied to each of the 10 000 blank-field simulated maps used in Section 5.5. Because the sources are randomly distributed, the probability distribution of their principal axes should be characteristic of fields without any alignment. The result can be seen in Fig. 16 as the dashed-line histogram. As expected, there is no preferred direction or no principal axis and the distribution is quite flat. Although a principal axis can be defined for any individual simulation, and the angle can be at any given value between 0 and 180 deg, the resulting probability of the 68 per cent confidence intervals is quite wide, with a median value of 60 deg. The distribution of widths has a tail towards high values, and widths as small as 27 deg happen by chance only 2 per cent of the time. However, these distributions are significantly different when a Kolmogorov–Smirnov test is used, and in no case, we find a shape coincidence with a significance greater than 95 per cent.

At submm/mm wavelengths higher flux densities usually mean higher luminosities (due to a flat $K$ correction for objects with $1 < z < 10$). Therefore, in order to test if the misalignment is traced by the most luminous SMGs, we determine principal axes of our stacked distribution of sources after applying different flux-density cuts. Top panel of Fig. 17 shows the angular differences between the radio jets and the principal axes of distributions of sources with flux densities less than a certain value. The bottom panel shows a similar plot but for sources with flux densities greater than those values. The red horizontal lines (solid and dotted–dashed lines) represent the 73-deg principal axis found for the whole distribution of sources and its 68 per cent confidence interval. As can be seen from the plots, while gradually removing the brightest galaxies causes no significant change in the alignment, gradually removing the faintest

galaxies shows some variation, mainly because brighter sources are much less common. Nevertheless, most estimated axes are above 45 deg, which points to a consistent trend for the principal axes.

## 7 DISCUSSION

### 7.1 Overdensity of SMGs towards AGN

Our source-counts analysis performed individually on the 17 fields show that only in the surroundings of three RGs (4C+23.56, PKS1138−262, and MRC0355−037), the number density of sources with $S_{1.1\mathrm{mm}} > 4$ mJy exceeds that of a blank field. The overdensity factors are ∼2 and have a significance $\gtrsim 3\sigma$, which means that the probability of finding overdensities like these ones by chance is <0.3 per cent. This finding is in line with previous studies, which described 4C+23.56 and PKS1138−262 fields as overdense environments via narrow-line emission surveys (Kurk et al. 2000; Tanaka et al. 2011) and, more recently, via IRAC studies at 3.6 and 4.5 μm (Galametz et al. 2012), and MIPS studies at 24 μm (Mayo et al. 2012). PKS1138−262 was also reported as SMG overdense by Dannerbauer et al. (2014). In addition, these three fields belong to the Clusters Around Radio-loud AGN (CARLA) sample (Wylezalek et al. 2013), which found overdensities in IRAC 3.6 and 4.5 μm data deeper than that used by Galametz et al. (2012). One point worth noticing is that these three fields have redshifts between $2.0 < z < 2.5$. Arguably, this may suggest that the field density of dust-enshrouded star-forming galaxies in protoclusters has a dependence on redshift, and that the epoch of protocluster peak activity is $z \sim 2$, which is consistent with the epoch of peak activity for blank-field SMGs (e.g. Chapman et al. 2005) and other populations like luminous quasars and X-ray-selected AGN (e.g Schmidt, Schneider & Gunn 1991; Boyle & Terlevich 1998). Nevertheless, our sample is too small to fully support such a statement, but future surveys with tens of protocluster candidates per redshift bin will help clarify this issue.

The rest of the ACES fields show source counts in agreement with those of a blank field. We showed, however, that in maps as large as ours an overdensity of 2 covering small areas (such as a circle of 1.5 arcmin radius) is confused with a blank field 91 per cent of the time (Section 5.6). Therefore, we cannot discard the presence of overdensities diluted by the expected sample variance of these individual maps. In the case of 4C+41.17, the field was found tentatively overdense by Ivison et al. (2000) using SCUBA observations with a field of view of 2.5 arcmin. However, Wylezalek et al. (2013) used *Herschel*/SPIRE observations to estimate that the excess of galaxies is at $z \sim 2.5$ and not at the redshift of the RG ($z = 3.792$).

In order to reduce sample variance, we performed the same source-count analysis in the combined fields. We detected an overdensity $\gtrsim 3$ at $S_{1.1\mathrm{mm}} \geq 4$ mJy occurring only inside areas of 1.5-arcmin radius centred at the AGN. The number density of sources falls to reach a blank-field density for successive and concentric annuli with 1.5-arcmin widths ($\Delta r = 1.5$ arcmin). The size of our ACES sample enabled us to detect this overdensity with a statistical significance >99.75 per cent (for sources with flux densities >4 mJy), which corresponds to a $3.5\sigma$ significance when the distribution of number of sources is approximated by a Gaussian. Another key advantage of the ACES survey is that both the sample and the blank-field reference data were observed with the same instrument (AzTEC), under very similar conditions, and reduced and analysed using the same techniques. Therefore, any bias or systematic error that could not have been identified during the observation and reduction stages affects both sets of data equally, allowing a fair comparison between them. In addition, the source counts used as reference come from the analysis of the combined data from six blank-field surveys carried out with AzTEC, which is the best estimation to-date of the 1.1-mm source counts at flux densities between $S_{1.1\mathrm{mm}} = 1$–12 mJy (Scott et al. 2012).

Since the redshift range of our sample of RGs and quasar spans from $z = 0.5$−6.3, a 1.5-arcmin radius corresponds to comoving diameters between 1.7 and 7.5 Mpc. This implies that at all redshifts the extension of the overdensity covers at least an area equivalent to the core of an average galaxy protocluster, whose diameter ($2 \times R_{200}$) can range from ∼0.4 to 2 comoving Mpc according to simulations (e.g. Chiang et al. 2017) and recent observations Miller et al. (2018). This result is in agreement with that of previous works that claim that high-redshift RGs reside in rich environments and may indicate the presence of protoclusters. It also supports the idea that SMGs trace dense environments at high redshifts (e.g. Umehata et al. 2015), although it is important to mention that there are observational and simulated data suggesting that SMGs do not always trace the most massive ones (e.g. Chapman et al. 2009; Miller et al. 2015).

Our measured overdensity shows a tendency to increase from a factor of ∼2–3.3 for sources with higher flux densities. This could be interpreted as the environment of protoclusters enhancing SFRs, probably through an increment in the merging rate, as expected under the standard model of structure formation (ΛCDM model). But it is important to remember that due to the AzTEC large beam size, very bright sources can also be the result of blending multiple fainter sources. Were this the case, we could still argue that around our AGN sample, the source density is higher than that in the blank field, implying that our fields could indeed be clusters in the process of formation. Nevertheless, it should be noted that recovery rates for sources with low S/Ns are difficult to estimate accurately and could affect the completeness calculations for low flux-density sources. Therefore, the decrement in the overdensity signal for lower flux-density sources could be artificial.

The SMGs contributing to our detected overdensity have 1.1-mm flux densities ranging from about 1–10 mJy with their SFRs ranging between 200 and 1800 $\mathrm{M}_{\odot}\ \mathrm{yr}^{-1}$ (Kennicutt 1998). If Arp 220 is indeed a good analogue (Stevens et al. 2010; Lapi et al. 2011; Magnelli et al. 2012; Contini 2013), and if the starburst can be sustained for a few hundred million years or so, then a stellar mass equivalent to that of the bulge of a large galaxy will be assembled ($10^{11}$–$10^{12}\ \mathrm{M}_{\odot}$). It is, therefore, logical to think that these overdense regions at high redshift contain galaxies that are capable of building large populations of stars that will evolve over cosmic time to become the massive elliptical galaxies that dominate the population in the cluster cores of the local Universe.

#### *7.1.1 Comparison with previous submm surveys*

Fig. 18 compares our results to previous submm studies acquired with SCUBA at 850 μm. Their observations were centred at AGN and covered areas of ∼1.5-arcmin radius. Their source counts are scaled to 1.1 mm using a dust emissivity index of 1.5, which is a common assumption since several works find its value in the range 1–2 (Casey et al. 2014). Fig. 18 shows that the magnitude and extension of the overdensity we found is mostly in agreement with the SCUBA studies, but taking into account some caveats.

Stevens et al. (2003) surveyed the environments of seven RGs with redshifts between $z = 2.2$−4.3, and found an overdensity of ∼2 although not statistically significant ($<2\sigma$) due to their

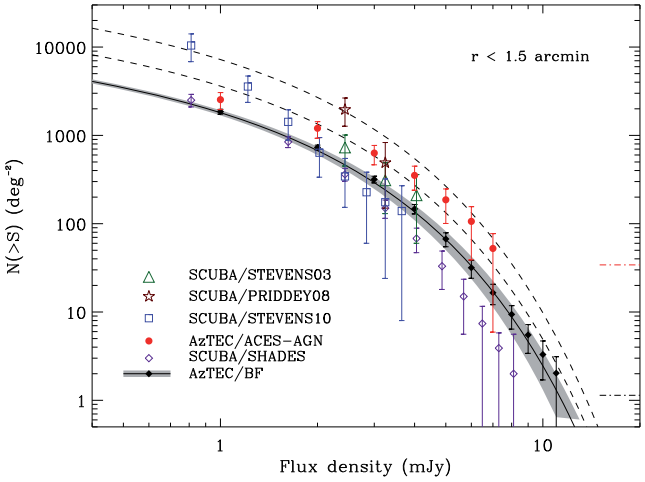


**Figure 18.** AzTEC 1.1 mm integrated source counts for the combined 17 ACES protocluster fields inside an area of 1.5-arcmin radius centred at the ACES AGN (solid circles). Source counts from previous studies with SCUBA at 850 μm by Stevens et al. (2003, triangles), Priddey et al. (2008, stars), and Stevens et al. (2010, squares) are shown for comparison. The AzTEC combined blank-field (AzTEC/BF; solid diamonds) and SCUBA/SHADES (diamonds) number counts are plotted for reference. SCUBA data are scaled to 1.1 mm using a dust emissivity index of 1.5 (Casey et al. 2014). Dashed lines represent overdensities of 2 and 4 compared to the AzTEC/BF, and horizontal dashed lines mark survey limits.

small sample. Meanwhile, Priddey et al. (2008) surveyed the environments of 3 optically selected quasars with redshifts between $z = 5$and6.3, and found an overdensity of ∼4, although the magnitude of this overdensity must be interpreted carefully because no corrections for incompleteness or flux boosting were applied on the data, in contrast to the corrections applied on SCUBA/SHADES (Coppin et al. 2006), their control field. Fig. 18 also shows that SHADES data points fall below AzTEC blank-field data, indicating that the assumed dust emissivity index may be < 1.5. Recently determined 850-μm source counts shows that these SHADES data points are in agreement with source-counts analysis from the ∼5-sq deg SCUBA-2 Cosmology Legacy Survey (Geach et al. 2017).

Stevens et al. (2010), on the other hand, found an opposite trend. They surveyed the environment of five X-ray-selected quasars with redshifts between $z = 1.7$ and 2.8 and reported an overdensity of ∼4 at the lower end of their source counts ($S_{1.1\mathrm{mm}} < 2$ mJy). This overdensity decreases at higher flux densities reaching their reference blank-field source density. A reason for such different trend could be that the lower flux-density bins are not well corrected for incompleteness and therefore the trend is artificial. But there is also the fact that Stevens et al. (2010) surveyed the environments of RQ-QSO in contrast to our study that concentrates on the environments of RGs. Following the work of Falder et al. (2010), who found evidence for larger overdensities of galaxies in the environments of radio-loud objects compared to the environments of radio-quiet ones (based on observations at 3.6 μm), Stevens et al. (2010) suggested that if their AGNs are indeed located in less dense regions of the Universe, the detection of an overdensity of sources only in the lowest flux-density bins (and therefore with the lowest SFRs) is feasible. Another possible explanation, specially regarding the fact that Priddey et al. (2008) detected an overdensity of SMGs towards $z > 5$ RQ-QSO at $S_{1.1\mathrm{mm}} > 2$ mJy, is that obscured star formation activity in protoclusters is incremental with redshift. This is in agreement with studies at submm wavelengths on high-redshift RGs showing that their detection rates increases at $z > 2.5$ (e.g. Archibald et al. 2001; Reuland et al. 2003).

In addition to SCUBA, *Hershel*/SPIRE (250, 350, and 500 μm) also performed surveys towards high-redshift biased regions. Rigby et al. (2014) studied the environment of 19 high-redshift RGs and reported a marginal excess of 500 μm sources within 6 comoving Mpc of the RG. When the analysis was restricted to potential protocluster members only (identified using a far-IR colour selection), it revealed that two fields have significant overdensities, one of 1.5 ($3.9\sigma$) and the other of 1.9 ($4.3\sigma$). Both the extension and the magnitude of these overdensities are in good agreement with our ACES results.

More recently, and based on studies suggesting that obscured AGN could be more strongly clustered and inhabit denser environments than unobscured AGN (e.g. Donoso et al. 2014), Jones et al. (2015, 2017) used 850 μm SCUBA-2 observations to study ovedensities of SMGs around obscured active galaxies. They studied the surroundings of 10 hot dust-obscured galaxies (Hot DOGs) and 30 *WISE* (*Wide-field Infrared Survey Explorer*, Wright et al. 2010)/radio-selected AGN, finding overdensities inside 1.5 arcmin scale maps of a factor of ∼2.4 and ∼5.6, respectively. In addition, Silva et al. (2015) used 870 μm high-resolution (0.45–1.24 arcsec) Atacama Large Millimeter Array (ALMA) observations to study the surroundings of 49 *WISE*/radio-selected dusty, hyperluminous quasars to find that the number of detected sources is 10 times greater than what is expected for unbiased regions. These results surely add to the idea that dusty powerful AGNs are signposts of dense regions in the early Universe. The overdensity factors, however, are not straightforward to compare. While the SCUBA-2 results appear to be in agreement with ours, the level of overdensity measured in the ALMA study appears five times higher. Silva et al. (2015) suggested that it could be an effect of source blending due to the large beam sizes of submm/mm single-dish telescopes.

### 7.1.2 *Comparison with Spitzer studies*

IRAC 3.6 and 4.5 μm studies were carried out towards 48 high-redshift RGs by Galametz et al. (2012), and more extensively towards 387 radio-loud AGNs by Wylezalek et al. (2013), both within a redshift range of $1.2 < z < 3.2$. They restricted the analysis to sources with colours [3.6] – [4.5] >−0.1 (AB) in order to select $z > 1.3$ galaxies, and found a clear rise in surface density of sources towards the position of the AGN. This rise sharpens at distances <1 arcmin, coinciding with the extension of the overdensity measured in our combined fields.

The 24-μm study by Mayo et al. (2012) of the environments of 63 RGs between redshifts $1 \leq z \leq 5.2$ also found an average overdensity of $2.2 \pm 1.2$ in 1.75-arcmin-radius circular cells centred on the RGs. In this case, both the extension and magnitude of the overdensity are in agreement with our results. Previous blank-field studies have shown that very red DOGs observed at 24 μm ($R - [24]$ colour>14) have similar properties to bright SMGs ($S_{850\mu\mathrm{m}} > 6$ mJy), which could suggest that these two populations are associated, at least in an evolutionary sequence (e.g. Dey et al. 2008; Pope et al. 2008; Wu et al. 2012). Consequently, a coincident ∼2 times overdensity of 24 μm and mm sources around RGs adds to the idea that, first, RGs are indeed very good protoclusters candidates, and second, these populations could very well form part of an evolutionary succession in which SMGs represent the early phase of the formation of a massive galaxy (the starburst-dominated phase, possibly <1 Gyr long), while DOGs represent the transition from a

starburst-dominated phase to an AGN-dominated phase (possibly ∼ 3–5 times shorter than the starburst-dominated phase – e.g. Coppin et al. 2010).

Higher resolution submm/mm experiments like ALMA or the 50-m Large Millimeter Telescope Alfonso Serrano (LMT) will help clarify this picture allowing more accurate multiwavelength counterpart identifications, better Spectral Energy Density (SED) determinations, and therefore, a more complete comparison of these two populations.

### 7.2 Misalignment of mm sources with respect to radio jets

We found that there is a trend for SMGs to align closer to a perpendicular direction to the ACES RG jets. This result is measured on the plane of the sky, since we do not have redshift information for the SMGs. The misalignment is found over a projected comoving scale of 4–20 Mpc, departs from perfect alignment (0 deg) by $\sim 5\sigma$ and is independent of source luminosity. We propose, under the assumption that the SMGs are at similar redshifts to the RGs that this misalignment could be the result of SMGs preferentially inhabiting dominant filaments feeding the protocluster structures that contain the RGs.

Using dark matter simulations, several studies have investigated primordial alignments between dark matter haloes and their large-scale filamentary structures (e.g. Aragón-Calvo et al. 2007; Zhang et al. 2009; Codis et al. 2012). They found that the orientation of the spin axes of the dark matter haloes is mass-dependent. Low-mass haloes ($\sim M < 10^{12}\,M_{\odot}$) have a tendency to have their spin axes oriented along the parent structure, while high-mass haloes have their spin axes perpendicular to it. Regarding baryonic matter, however, fewer studies have investigated the alignment between galaxy spin axes and their embedding cosmic web, mainly because of the high computational cost of the simulations. Recently, Dubois et al. (2014) used a large-scale hydrodynamical cosmological simulation to investigate the alignment between galaxy spins and their surrounding cosmic filaments at $1.2 < z < 1.8$. They showed that the spin of low-mass blue galaxies is preferentially aligned with their neighbouring filaments, while high-mass red galaxies tend to have a perpendicular spin as a result of mergers.

Observationally, Tempel, Stoica & Saar (2013) and Zhang et al. (2013) also found tentative evidence of such alignments in the Sloan Digital Sky Survey. In addition, one of the best known examples of preferential alignments is the orientation of the major axes of bright cluster galaxies (BCGs) along the distribution of cluster members and how they point towards other nearby clusters on scales of ∼10–20 Mpc (Carter & Metcalfe 1980; Binggeli 1982; Struble 1990; Plionis 1994; Hashimoto, Henry & Boehringer 2008). This alignment could be explained as clusters forming at the intersection of different filaments but with a dominant filamentary feature that is likely to exert the most profound influence on the final cluster–BCG orientation (West 1994).

Considering all this evidence and the fact that high-redshift RGs are very massive sources, we may expect their spin axes, both of their dark matter halo and the galaxy itself, to be aligned perpendicularly to the direction of their embedding dominant filaments. Currently, there is no way to observationally corroborate how dark matter spins in galaxies. In some cases, however, radio jets PAs were found to act as a proxy for the direction of the major axis of the baryonic matter in their host galaxies. For instance, extended radio jets were found preferentially aligned with the optical minor axes of their galaxies, particularly for elliptical galaxies (e.g. Condon, Frayer & Broderick 1991; Battye & Browne 2009). If we assume that the radio jets in our sample are aligned with their galaxies' minor axes, the fact that we find their PAs to be closer to a perpendicular direction with respect to the principal axis of the SMGs spatial distribution could be interpreted as SMGs tracing large-scale structure and inhabiting dominant filaments feeding the protocluster structures that contain the RGs.

Stevens et al. (2003) also studied alignments of SMGs around their high-redshift RG sample. They compared the radio jet PA with the location of the brightest submm source in the map, apart from the AGN. The location of this bright submm companion was expected to give an idea about the orientation of the large-scale structure around the RG. They found a possible alignment between the radio jet and the large-scale structure. We propose that this opposite outcome was the result of having small maps (2.5-arcmin diameter) and a limited data set (seven fields). If we artificially reduce our field of views to what Stevens et al. (2003) would have observed, we find that 13 of the 16 fields have at least one mm companion. From these 13, 11 have their brightest companion more than 45 deg away from the radio jet, i.e. in agreement with our misalignment result.

## 8 CONCLUSIONS

We explored the spatial distribution of SMGs towards the environments of 16 powerful high-redshift RGs and a quasar using continuum observations at 1.1 mm taken with the AzTEC camera. We targeted the environments of powerful high-redshift AGN in order to pinpoint the location of the progenitors of the richest galaxy clusters we see today in the local Universe. After removing possible mm counterparts to the AGN, we estimated source counts for individual fields, but in the majority of cases the density of sources with $S_{1.1\mathrm{mm}} > 4$ mJy fell within the 95 per cent confidence interval of the density of sources in a comparison sample of unbiased blank fields. Only in the surroundings of 4C+23.56, PKS1138−262, and MRC0355−037 did we detect individual overdensity signals of ∼2 with a significance of $\sim 3\sigma$. Performing simulations, however, we found that 91 per cent of the time an overdensity of a factor 2 covering a small area of 1.5 arcmin radius is lost in a number density analysis of sources with $S_{1.1\mathrm{mm}} > 4$ mJy populating maps as large as our ACES maps. Therefore, we cannot discard the presence of overdensities confused with the expected sample variance of our individual maps.

When we performed a combined analysis on the complete sample, we found an overdensity $\gtrsim 3$ at $S_{1.1\mathrm{mm}} \geq 4$ mJy with greater statistical significance, covering an area of 1.5-arcmin radius centred on the AGN (corresponding to a comoving diameter of 1.7–7.5 Mpc over the redshift range $0.5 < z < 6.3$ of the sample, and a comoving diameter of 4.6–7.5 Mpc over $2 < z < 6.3$, where most of our targets lie). The large size of our maps allowed us to establish that beyond a radius of 1.5 arcmin, the radial surface density of SMGs falls to reach a typical value for a blank-field distribution of SMGs. The measured angular extent of this overdensity is in agreement with protocluster core simulations and observations. In addition, we found that the overdensity shows a tendency to increase with higher flux densities.

We interpreted this as an enhancement in the dust-obscured star formation activity towards protocluster environments, detected either as an increment in the SFRs of individual galaxies or as an increment in the number of sources that get blended due to the large size of the AzTEC beam.

The data used as reference to measure the magnitude and extent of the overdensity are composed of six blank-field surveys

carried out also with AzTEC. These observations provide the best estimation to-date of the 1.1-mm source counts towards blank fields at $S_{1.1\mathrm{mm}} = 1$–12 mJy. In addition, our protocluster targets and the blank-field data were observed, reduced, and analysed under very similar conditions and using the same techniques. Therefore, a fair comparison between them is possible.

We also examined if there was a preferred direction, on the plane of the sky, in which the SMGs align around our sample of high-redshift RGs. Using a tool motivated by the form of the tensor of inertia, we found that there is a trend for SMGs to align along an orientation that is closer to a perpendicular direction with respect to the radio jets ($73^{-14}_{+13}$ deg) than to the parallel direction. This misalignment was found over projected comoving scales of 4–20 Mpc, departs from perfect alignment (0 deg) by $\sim 5\sigma$ and apparently has no dependence on the source luminosity, although the dynamical range of our flux-limited sample is probably not large enough to draw a definite conclusion.

Since our RGs are thought to be massive sources, and simulations predict that their dark matter halo spin axes align perpendicularly to the direction of the dominant filament feeding them, we suggest that this misalignment could be the result of SMGs preferentially inhabiting the mass-dominant filaments funnelling material towards the protoclusters that contain our RGs. This suggestion is based on the assumptions that the distribution of baryonic matter roughly follows the distribution of dark matter, and that the radio jets in our sample are a proxy for their galaxies' minor axes.

The properties of the SMG distribution described above are consistent with the idea that powerful AGNs reside in massive dark matter haloes, and that these protocluster regions are sites of enhanced dust-obscured star formation. In the local Universe, the centres of rich clusters are inhabited preferentially by massive elliptical galaxies. Assuming their progenitors go through a submm phase, we speculate that SMGs in these environments are forming a large fraction of the stellar population of the massive ellipticals. Moreover, these properties also show that SMGs are probably contributing to the formation of the stellar population in the filamentary structure around them, since they appear to be tracing at least the most dominant structures.

## ACKNOWLEDGEMENTS

We would like to thank everyone who supported the AzTEC/ASTE and AzTEC/JCMT observations of the ACES fields. This work has been supported by Consejo Nacional de Ciencia y Tecnologia (CONACYT) projects CB-2011-01-167291 and FDC-2016-1848, and by CONACYT studentship 12812. AH acknowledges Fundaçâo para a Ciência e a Tecnologia (FCT) support through UID/FIS/04434/2013, and through project FCOMP-01-0124-FEDER-029170 (reference FCT PTDC/FIS-AST/3214/2012) funded by FCT-MEC (PIDDAC) and FEDER (COMPETE), in addition to FP7 project PIRSES-GA-2013-612701, and FCT grant SFRH/BPD/107919/2015. KK recognizes the support of the MEXT Grant-in-Aid for Specially Promoted Research JP20001003 and the JSPS Grant-in-Aid for Scientific Research (S) JP17H06130. The ASTE project is driven by the Nobeyama Radio Observatory (NRO), a branch of the National Astronomical Observatory of Japan (NAOJ), in collaboration with the University of Chile and Japanese institutions including the University of Tokyo, Nagoya University, Osaka Prefecture University, Ibaraki University, and Hokkaido University. Observations with ASTE were in part carried out remotely from Japan by using NTT's GEMnet2 and its partner R&E (Research and Education) networks, which are based on AcessNova collaboration of University of Chile, NTT Laboratories, and NAOJ. The JCMT is operated by the Joint Astronomy Centre on behalf of the Science and Technology Facilities Council of the United Kingdom, the Netherlands Organisation for Scientific Research, and the National Research Council of Canada.

## REFERENCES

Andreon S., Maughan B., Trinchieri G., Kurk J., 2009, A&A, 507, 147
Aragón-Calvo M. A., van de Weygaert R., Jones B. J. T., van der Hulst J. M., 2007, ApJ, 655, L5
Archibald E. N., Dunlop J. S., Hughes D. H., Rawlings S., Eales S. A., Ivison R. J., 2001, MNRAS, 323, 417
Aretxaga I., Hughes D. H., Chapin E. L., Gaztañaga E., Dunlop J. S., Ivison R. J., 2003, MNRAS, 342, 759
Aretxaga I. et al., 2007, MNRAS, 379, 1571
Aretxaga I. et al., 2011, MNRAS, 415, 3831
Austermann J. E. et al., 2009, MNRAS, 393, 1573
Austermann J. E. et al., 2010, MNRAS, 401, 160
Basilakos S., Plionis M., Yepes G., Gottlöber S., Turchaninov V., 2006, MNRAS, 365, 539
Battye R. A., Browne I. W. A., 2009, MNRAS, 399, 1888
Best P. N., Eales S. A., Longair M. S., Rawlings S., Rottgering H. J. A., 1999, MNRAS, 303, 616
Binggeli B., 1982, A&A, 107, 338
Bothwell M. S. et al., 2013, MNRAS, 429, 3047
Boyle B. J., Terlevich R. J., 1998, MNRAS, 293, L49
Bracco A. et al., 2011, MNRAS, 412, 1151
Broderick J. W., De Breuck C., Hunstead R. W., Seymour N., 2007, MNRAS, 375, 1059
Burgess A. M., Hunstead R. W., 2006, AJ, 131, 114
Carter D., Metcalfe N., 1980, MNRAS, 191, 325
Casey C. M., Narayanan D., Cooray A., 2014, Phys. Rep., 541, 45
Chambers K. C., Miley G. K., van Breugel W. J. M., 1990, ApJ, 363, 21
Chambers K. C., Miley G. K., van Breugel W. J. M., Bremer M. A. R., Huang J.-S., Trentham N. A., 1996, ApJS, 106, 247
Chapman S. C., Blain A. W., Ivison R. J., Smail I. R., 2003, Nature, 422, 695
Chapman S. C., Blain A. W., Smail I., Ivison R. J., 2005, ApJ, 622, 772
Chapman S. C., Blain A., Ibata R., Ivison R. J., Smail I., Morrison G., 2009, ApJ, 691, 560
Chiang Y.-K., Overzier R. A., Gebhardt K., Henriques B., 2017, ApJ, 844, L23
Clements D. L. et al., 2014, MNRAS, 439, 1193
Codis S., Pichon C., Devriendt J., Slyz A., Pogosyan D., Dubois Y., Sousbie Th., 2012, MNRAS, 427, 3320
Condon J. J., Frayer D. T., Broderick J. J., 1991, AJ, 101, 362
Contini M., 2013, MNRAS, 429, 242
Coppin K., Halpern M., Scott D., Borys C., Chapman S. 2005, MNRAS, 357, 1022
Coppin K. et al., 2006, MNRAS, 372, 1621
Coppin K. E. K. et al., 2009, MNRAS, 395, 1905
Coppin K. et al., 2010, ApJ, 713, 503
Cox P. et al., 2011, ApJ, 740, 63
Dannerbauer H. et al., 2014, A&A, 570, A55
De Breuck C., van Breugel W., Röttgering H. J. A., Miley G., 2000, A&AS, 143, 303
De Breuck C. et al., 2004, A&A, 424, 1
de Zotti G., Massardi M., Negrello M., Wall J., 2010, A&AR, 18, 1
Demarco R. et al., 2010, ApJ, 725, 1252
Demarco R. et al., 2010, ApJ, 711, 1185
Dey A. et al., 2008, ApJ, 677, 943
Dole H. et al., 2006, A&A, 451, 417
Donoso E., Yan L., Stern D., Assef R. J., 2014, ApJ, 789, 44
Downes A. J. B., Peacock J. A., Savage A., Carrie D. R., 1986, MNRAS, 218, 31

Downes T. P., Welch D., Scott K. S., Austermann J., Wilson G. W., Yun M. S., 2012, MNRAS, 423, 529
Dubois Y. et al., 2014, MNRAS, 444, 1453
Dye S. et al., 2008, MNRAS, 386, 1107
Eales S. A., 1985, MNRAS, 217, 149
Falder J. T. et al., 2010, MNRAS, 405, 347
Faltenbacher A., Jing Y. P., Li C., Mao S., Mo H. J., Pasquali A., van den Bosch F. C., 2008, ApJ, 675, 146
Fazio G. G. et al., 2004, ApJS, 154, 10
Flores-Cacho I. et al., 2016, A&A, 585, A54
Galametz A. et al., 2012, ApJ, 749, 169
Geach J. E. et al., 2017, MNRAS, 465, 1789
Gerhard O. E., 1983, MNRAS, 203, 19P
Gopal-Krishna Ledoux C., Melnick J., Giraud E., Kulkarni V., Altieri B., 2005, A&A, 436, 457
Greve T. R. et al., 2005, MNRAS, 359, 1165
Harrison I., Coles P., 2012, MNRAS, 421, L19
Hashimoto Y., Henry J. P., Boehringer H., 2008, MNRAS, 390, 1562
Hatch N. A., Kurk J. D., Pentericci L., Venemans B. P., Kuiper E., Miley G. K., Röttgering H. J. A., 2011, MNRAS, 415, 2993
Hayashi M., Kodama T., Tadaki K.-i., Koyama Y., Tanaka I. 2012, ApJ, 757, 15
Hogg D. W., Turner E. L., 1998, PASP, 110, 727
Humphrey A. et al., 2011, MNRAS, 418, 74
Intema H. T., Venemans B. P., Kurk J. D., Ouchi M., Kodama T., Röttgering H. J. A., Miley G. K., Overzier R. A., 2006, A&A, 456, 433
Ivison R. J., Dunlop J. S., Smail I., Dey A., Liu M. C., Graham J. R., 2000, ApJ, 542, 27
Ivison R. J. et al., 2007, MNRAS, 380, 199
Jimenez R., Verde L., 2009, Phys. Rev. D, 80, 127302
Jones S. F. et al., 2015, MNRAS, 448, 3325
Jones S. F. et al., 2017, MNRAS, 469, 4565
Kapahi V. K., Athreya R. M., van Breugel W., McCarthy P. J., Subrahmanya C. R. 1998, ApJS, 118, 275
Kennicutt R. C., Jr., 1998, ARA&A, 36, 189
Kurk J. D. et al., 2000, A&A, 358, L1
Kurk J. D., Pentericci L., Overzier R. A., Röttgering H. J. A., Miley G. K. 2004, A&A, 428, 817
Laing R. A., Riley J. M., Longair M. S., 1983, MNRAS, 204, 151
Lapi A. et al., 2011, ApJ, 742, 24
Magnelli B. et al., 2012, A&A, 548, A22
Mayo J. H., Vernet J., De Breuck C., Galametz A., Seymour N., Stern D., 2012, A&A, 539, A33
McCarthy P. J., Kapahi V. K., van Breugel W., Subrahmanya C. R., 1990, AJ, 100, 1014
McLure R. J., Dunlop J. S., 2001, MNRAS, 321, 515
McLure R. J., Dunlop J. S., 2002, MNRAS, 331, 795
Menanteau F. et al., 2009, ApJ, 698, 1221
Miley G. K. et al., 2004, Nature, 427, 47
Miller T. B., Hayward C. C., Chapman S. C., Behroozi P. S., 2015, MNRAS, 452, 878
Miller T. B. et al., 2018, Nature, 556, 469
Morganti R., Killeen N. E. B., Tadhunter C. N., 1993, MNRAS, 263, 1023
O'Dea C. P., 1998, PASP, 110, 493
Overzier R. A. et al., 2006, ApJ, 637, 58
Pentericci L., Roettgering H. J. A., Miley G. K., Carilli C. L., McCarthy P. 1997, A&A, 326, 580
Pentericci L., McCarthy P. J., Röttgering H. J. A., Miley G. K., van Breugel W. J. M., Fosbury R., 2001, ApJS, 135, 63
Perera T. A. et al., 2008, MNRAS, 391, 1227
Pierre M. et al., 2004, J. Cosmol. Astropart. Phys., 9, 11
Planck Collaboration VI, 2013, A&A, 550, A132
Planck Collaboration XXVII, 2015, A&A, 582, A30
Plionis M., 1994, ApJS, 95, 401
Pope A., Borys C., Scott D., Conselice C., Dickinson M., Mobasher B., 2005, MNRAS, 358, 149
Pope A. et al., 2008, ApJ, 689, 127
Priddey R. S., Ivison R. J., Isaak K. G., 2008, MNRAS, 383, 289
Rawlings S., Eales S., Lacy M., 2001, MNRAS, 322, 523
Rees M. J., 1978, Nature, 275, 516
Reuland M. et al., 2003, ApJ, 592, 755
Riechers D. A. et al., 2010, ApJ, 720, L131
Rigby E. E., Snellen I. A. G., Best P. N., 2007, MNRAS, 380, 1449
Rigby E. E. et al., 2014, MNRAS, 437, 1882
Rocca-Volmerange B., Le Borgne D., De Breuck C., Fioc M., Moy E. 2004, A&A, 415, 931
Rosati P., della Ceca R., Norman C., Giacconi R., 1998, ApJ, 492, L21
Schmidt M., Schneider D. P., Gunn J. E., 1991, in ASP Conf. Ser., Vol. 21, The Space Distribution of Quasars. Astron. Soc. Pac., San Francisco, p. 394
Scott K. S. et al., 2008, MNRAS, 385, 2225
Scott K. S. et al., 2010, MNRAS, 405, 2260
Scott K. S. et al., 2012, MNRAS, 423, 575
Seymour N. et al., 2007, ApJS, 171, 353
Silva A., Sajina A., Lonsdale C., Lacy M., 2015, ApJ, 806, L25
Simpson J. M. et al., 2014, ApJ, 788, 125
Smolčić V. et al., 2012, A&A, 548, A4
Snellen I. A. G., Bremer M. N., Schilizzi R. T., Miley G. K., van Ojik R. 1996, MNRAS, 279, 1294
Snellen I. A. G., Bremer M. N., Schilizzi R. T., Miley G. K., 1996, MNRAS, 283, L123
Stevens J. A. et al., 2003, Nature, 425, 264
Stevens J. A., Jarvis M. J., Coppin K. E. K., Page M. J., Greve T. R., Carrera F. J., Ivison R. J., 2010, MNRAS, 405, 2623
Struble M. F., 1990, AJ, 99, 743
Tamura Y. et al., 2009, Nature, 459, 61
Tanaka I. et al., 2011, PASJ, 63, 415
Targett T. A., Dunlop J. S., McLure R. J., Best P. N., Cirasuolo M., Almaini O., 2011, MNRAS, 412, 295
Targett T. A. et al., 2013, MNRAS, 432, 2012
Taylor A. R., Jagannathan P., 2016, MNRAS, 459, L36
Tempel E., Stoica R. S., Saar E., 2013, MNRAS, 428, 1827
Umehata H. et al., 2015, ApJ, 815, L8
Velliscig M. et al., 2015, MNRAS, 454, 3328
Venemans B. P. et al., 2007, A&A, 461, 823
Walter F. et al., 2012, Nature, 486, 233
Wang R. et al., 2013, ApJ, 773, 44
Wardlow J. L. et al., 2011, MNRAS, 415, 1479
West M. J., 1994, MNRAS, 268, 79
Willott C. J., Bergeron J., Omont A., 2015, ApJ, 801, 123
Wilson G. W. et al., 2008, MNRAS, 386, 807
Wilson G. W. et al., 2008, MNRAS, 390, 1061
Wright E. L. et al., 2010, AJ, 140, 1868
Wu J. et al., 2012, ApJ, 756, 96
Wylezalek D. et al., 2013, ApJ, 769, 79
Wylezalek D. et al., 2013, MNRAS, 428, 3206
Xiang L., Reynolds C., Strom R. G., Dallacasa D., 2006, A&A, 454, 729
Yun M. S., 2012, MNRAS, 420, 957
Zhang Y., Yang X., Faltenbacher A., Springel V., Lin W., Wang H., 2009, ApJ, 706, 747
Zhang Y., Yang X., Wang H., Wang L., Mo H. J., van den Bosch F. C., 2013, ApJ, 779, 160

## APPENDIX A: DATA REDUCTION AND ANALYSIS PRODUCTS

Set of products for each ACES protocluster field. The sets are listed in decreasing order according to the redshift of the central AGN (as shown in Table 1). Each set contains the following plots and tables:

(1) AzTEC signal and weight maps. Source candidates have S/N $>3.5$ for the fields of TNJ1338−1942 and 4C+41.17, and S/N $>3.0$ for the rest of the maps. ASTE maps have their source candidates marked by 30-arcsec diameter circles, while the JCMT map has

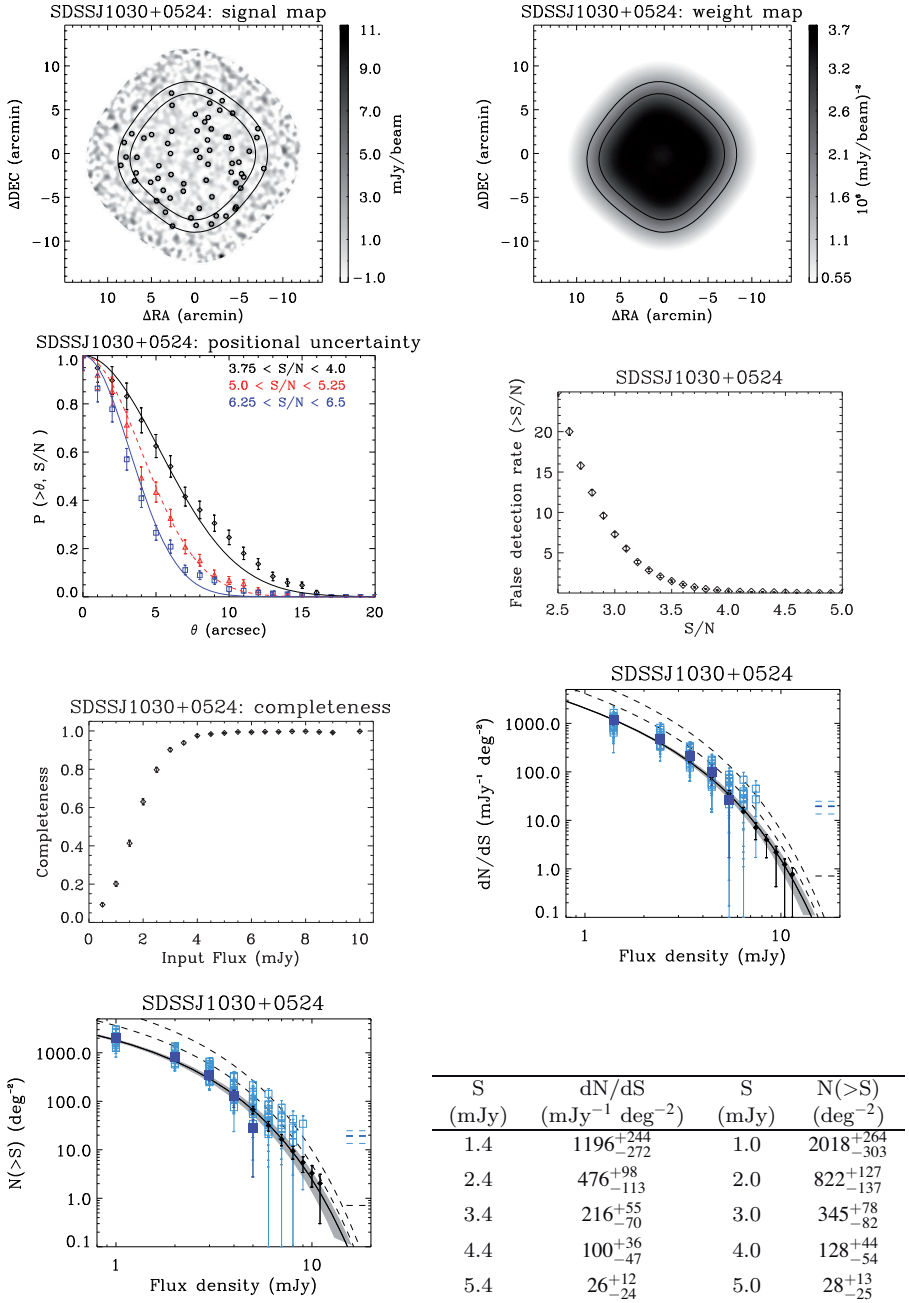


| S (mJy) | dN/dS (mJy$^{-1}$ deg$^{-2}$) | S (mJy) | N(>S) (deg$^{-2}$) |
|---|---|---|---|
| 1.4 | $1196^{+244}_{-272}$ | 1.0 | $2018^{+264}_{-303}$ |
| 2.4 | $476^{+98}_{-113}$ | 2.0 | $822^{+127}_{-137}$ |
| 3.4 | $216^{+55}_{-70}$ | 3.0 | $345^{+78}_{-82}$ |
| 4.4 | $100^{+36}_{-47}$ | 4.0 | $128^{+44}_{-54}$ |
| 5.4 | $26^{+12}_{-24}$ | 5.0 | $28^{+13}_{-25}$ |

**Figure A1.** SDSSJ1030+0524 products.

18-arcsec diameter circles. Contours represent the 75 per cent and 50 per cent coverage cuts.

(2) Positional uncertainty distributions for sources within three different S/N bins: 3.75 < S/N < 4.0 (diamonds), 5.0 < S/N < 5.25 (triangles), and 6.25 < S/N < 6.5 (squares). The curves show the analytical expression derived in Ivison et al. (2007) for the corresponding S/N bins.

(3) FDR, estimated using jackknife maps, for sources with S/N greater than a certain value. The error bars represent the 68 per cent confidence interval from a Poisson distribution.

(4) Completeness estimation as a function of flux density. The error bars represent the 68 per cent confidence interval from a binomial distribution.

(5) AzTEC 1.1-mm differential source counts (solid squares) compared to those of the reference field (diamonds). Differential source counts for the other 16 fields are also shown as comparison (open squares). The solid line and grey shading represent the best fit of a Schechter function to the density of sources of the reference field and its 68 per cent confidence interval. Dashed lines show twice and four times the source counts described by the fit. Horizontal dashed lines represent the survey limit, defined as the source density (inside de map area) that will Poisson deviate to zero sources 32 per cent of the time.

(6) AzTEC 1.1-mm integrated source counts. Symbols and lines are coded as with the differential source counts.

**Table A1.** SDSSJ1030+0524 source catalogue.

| ID | IAU name | S/N | $S_{1.1mm}$ (measured) (mJy) | $S_{1.1mm}$ (deboosted) (mJy) | $P(<0)$ |
|---|---|---|---|---|---|
| 1 | MMJ103019.72+052743.31 | 9.37 | $5.0 \pm 0.5$ | $4.7^{+0.6}_{-0.5}$ | 0.000 |
| 2 | MMJ103008.45+052133.48 | 8.59 | $5.0 \pm 0.6$ | $4.7^{+0.6}_{-0.6}$ | 0.000 |
| 3 | MMJ103044.81+051930.54 | 8.30 | $5.3 \pm 0.6$ | $5.0^{+0.6}_{-0.7}$ | 0.000 |
| 4 | MMJ103025.24+051839.75 | 8.14 | $4.6 \pm 0.6$ | $4.3^{+0.6}_{-0.6}$ | 0.000 |
| 5 | MMJ103032.40+052128.05 | 8.12 | $4.3 \pm 0.5$ | $4.0^{+0.6}_{-0.5}$ | 0.000 |
| 6 | MMJ103010.00+052930.91 | 7.12 | $4.5 \pm 0.6$ | $4.2^{+0.7}_{-0.7}$ | 0.000 |
| 7 | MMJ103022.10+052151.99 | 7.09 | $3.8 \pm 0.5$ | $3.5^{+0.5}_{-0.5}$ | 0.000 |
| 8 | MMJ103029.06+051734.06 | 6.80 | $4.2 \pm 0.6$ | $3.9^{+0.6}_{-0.6}$ | 0.000 |
| 9 | MMJ103019.46+051958.00 | 6.59 | $3.6 \pm 0.5$ | $3.3^{+0.6}_{-0.6}$ | 0.000 |
| 10 | MMJ103002.34+052510.13 | 6.46 | $3.8 \pm 0.6$ | $3.5^{+0.6}_{-0.6}$ | 0.000 |
| 11 | MMJ103053.87+052428.75 | 6.42 | $3.8 \pm 0.6$ | $3.5^{+0.6}_{-0.6}$ | 0.000 |
| 12 | MMJ103026.68+052515.98 | 6.24 | $3.4 \pm 0.5$ | $3.1^{+0.6}_{-0.5}$ | 0.000 |
| 13 | MMJ103019.68+051651.81 | 6.10 | $4.3 \pm 0.7$ | $3.9^{+0.7}_{-0.7}$ | 0.000 |
| 14 | MMJ103037.54+051637.49 | 6.08 | $4.7 \pm 0.8$ | $4.1^{+0.8}_{-0.8}$ | 0.000 |
| 15 | MMJ103041.78+052042.58 | 5.90 | $3.3 \pm 0.6$ | $3.0^{+0.6}_{-0.6}$ | 0.000 |
| 16 | MMJ103032.57+052036.81 | 5.75 | $3.1 \pm 0.5$ | $2.8^{+0.5}_{-0.6}$ | 0.000 |
| 17 | MMJ103038.00+053148.37 | 5.67 | $3.9 \pm 0.7$ | $3.4^{+0.7}_{-0.7}$ | 0.000 |
| 18 | MMJ103020.50+052517.10 | 5.55 | $2.9 \pm 0.5$ | $2.6^{+0.5}_{-0.6}$ | 0.000 |
| 19 | MMJ103037.91+052727.52 | 5.53 | $2.9 \pm 0.5$ | $2.6^{+0.5}_{-0.6}$ | 0.000 |
| 20 | MMJ103010.19+052347.41 | 5.37 | $2.9 \pm 0.5$ | $2.5^{+0.6}_{-0.5}$ | 0.000 |
| 21 | MMJ103059.69+052609.82 | 5.28 | $3.9 \pm 0.7$ | $3.3^{+0.8}_{-0.8}$ | 0.000 |
| 22 | MMJ103050.66+052640.44 | 5.25 | $3.1 \pm 0.6$ | $2.7^{+0.6}_{-0.6}$ | 0.000 |
| 23 | MMJ103037.74+053025.12 | 5.22 | $3.1 \pm 0.6$ | $2.7^{+0.6}_{-0.6}$ | 0.000 |
| 24 | MMJ103040.79+051813.05 | 5.12 | $3.4 \pm 0.7$ | $3.0^{+0.7}_{-0.7}$ | 0.000 |
| 25 | MMJ103017.47+051747.86 | 4.98 | $3.3 \pm 0.7$ | $2.8^{+0.7}_{-0.7}$ | 0.000 |
| 26 | MMJ103021.24+052341.16 | 4.93 | $2.6 \pm 0.5$ | $2.3^{+0.5}_{-0.6}$ | 0.000 |
| 27 | MMJ103058.85+052430.84 | 4.91 | $3.3 \pm 0.7$ | $2.8^{+0.7}_{-0.7}$ | 0.000 |
| 28 | MMJ103025.01+052427.94 | 4.69 | $2.5 \pm 0.5$ | $2.2^{+0.6}_{-0.6}$ | 0.000 |
| 29 | MMJ103020.46+053039.70 | 4.64 | $2.8 \pm 0.6$ | $2.4^{+0.6}_{-0.6}$ | 0.000 |
| 30 | MMJ103044.20+052204.44 | 4.49 | $2.4 \pm 0.5$ | $2.1^{+0.6}_{-0.6}$ | 0.000 |
| 31 | MMJ103039.76+052603.63 | 4.39 | $2.3 \pm 0.5$ | $2.0^{+0.5}_{-0.6}$ | 0.000 |
| 32 | MMJ103054.87+052147.14 | 4.37 | $2.8 \pm 0.7$ | $2.4^{+0.7}_{-0.7}$ | 0.000 |
| 33 | MMJ102958.84+052644.21 | 4.36 | $2.9 \pm 0.7$ | $2.4^{+0.7}_{-0.7}$ | 0.000 |
| 34 | MMJ103022.75+052831.35 | 4.35 | $2.3 \pm 0.5$ | $2.0^{+0.5}_{-0.6}$ | 0.000 |
| 35 | MMJ103026.71+051642.99 | 4.26 | $2.9 \pm 0.7$ | $2.4^{+0.7}_{-0.8}$ | 0.001 |
| 36 | MMJ103047.14+052704.44 | 4.18 | $2.3 \pm 0.6$ | $2.0^{+0.6}_{-0.6}$ | 0.001 |
| 37 | MMJ103006.24+052057.68 | 4.12 | $2.6 \pm 0.6$ | $2.1^{+0.7}_{-0.7}$ | 0.001 |
| 38 | MMJ102958.37+052745.51 | 4.11 | $3.0 \pm 0.7$ | $2.4^{+0.8}_{-0.8}$ | 0.001 |
| 39 | MMJ103101.22+052333.94 | 4.05 | $3.0 \pm 0.7$ | $2.4^{+0.8}_{-0.8}$ | 0.002 |
| 40 | MMJ103020.25+053201.18 | 3.94 | $2.8 \pm 0.7$ | $2.2^{+0.7}_{-0.7}$ | 0.002 |
| 41 | MMJ103005.87+052235.96 | 3.86 | $2.2 \pm 0.6$ | $1.8^{+0.6}_{-0.6}$ | 0.002 |
| 42 | MMJ103013.02+051746.17 | 3.81 | $2.8 \pm 0.7$ | $2.1^{+0.8}_{-0.8}$ | 0.004 |
| 43 | MMJ103015.88+052951.74 | 3.81 | $2.3 \pm 0.6$ | $1.8^{+0.6}_{-0.6}$ | 0.003 |
| 44 | MMJ103013.05+052648.17 | 3.77 | $2.0 \pm 0.5$ | $1.6^{+0.6}_{-0.6}$ | 0.002 |
| 45 | MMJ103027.07+052924.53 | 3.74 | $2.0 \pm 0.5$ | $1.6^{+0.6}_{-0.6}$ | 0.003 |
| 46 | MMJ103038.20+052230.82 | 3.66 | $2.0 \pm 0.5$ | $1.5^{+0.6}_{-0.5}$ | 0.003 |
| 47 | MMJ103010.44+052528.28 | 3.62 | $1.9 \pm 0.5$ | $1.5^{+0.5}_{-0.6}$ | 0.004 |
| 48 | MMJ103047.57+052137.80 | 3.59 | $2.0 \pm 0.6$ | $1.6^{+0.6}_{-0.6}$ | 0.005 |
| 49 | MMJ103056.22+052710.33 | 3.48 | $2.4 \pm 0.7$ | $1.7^{+0.7}_{-0.7}$ | 0.010 |

**Table A1** – *continued*

| ID | IAU name | S/N | $S_{1.1mm}$ (measured) (mJy) | $S_{1.1mm}$ (deboosted) (mJy) | $P(<0)$ |
|---|---|---|---|---|---|
| 50 | MMJ103021.18+052901.68 | 3.42 | $1.9 \pm 0.5$ | $1.4^{+0.6}_{-0.6}$ | 0.008 |
| 51 | MMJ103008.78+051835.73 | 3.41 | $2.5 \pm 0.7$ | $1.8^{+0.8}_{-0.8}$ | 0.014 |
| 52 | MMJ103026.26+052730.51 | 3.37 | $1.8 \pm 0.5$ | $1.4^{+0.5}_{-0.6}$ | 0.009 |
| 53 | MMJ103008.40+051848.25 | 3.33 | $2.4 \pm 0.7$ | $1.7^{+0.8}_{-0.8}$ | 0.017 |
| 54 | MMJ103038.64+051949.84 | 3.30 | $1.9 \pm 0.6$ | $1.4^{+0.6}_{-0.6}$ | 0.012 |
| 55 | MMJ103004.87+052213.53 | 3.24 | $1.9 \pm 0.6$ | $1.4^{+0.6}_{-0.6}$ | 0.016 |
| 56 | MMJ103021.48+052627.72 | 3.21 | $1.7 \pm 0.5$ | $1.2^{+0.6}_{-0.6}$ | 0.014 |
| 57 | MMJ103038.46+052454.78 | 3.10 | $1.6 \pm 0.5$ | $1.2^{+0.6}_{-0.6}$ | 0.019 |
| 58 | MMJ103007.10+052355.59 | 3.08 | $1.7 \pm 0.5$ | $1.2^{+0.6}_{-0.6}$ | 0.021 |
| 59 | MMJ103010.58+052246.46 | 3.06 | $1.7 \pm 0.5$ | $1.2^{+0.6}_{-0.6}$ | 0.022 |
| 60 | MMJ103011.93+052647.02 | 3.06 | $1.6 \pm 0.5$ | $1.2^{+0.6}_{-0.6}$ | 0.022 |
| 61 | MMJ103043.80+052331.41 | 3.06 | $1.6 \pm 0.5$ | $1.1^{+0.6}_{-0.6}$ | 0.021 |
| 62 | MMJ103014.75+053056.13 | 3.03 | $2.1 \pm 0.7$ | $1.4^{+0.7}_{-0.7}$ | 0.034 |
| 63 | MMJ102955.67+052311.57 | 3.03 | $2.3 \pm 0.7$ | $1.5^{+0.8}_{-0.8}$ | 0.039 |
| 64 | MMJ103054.22+052241.98 | 3.03 | $1.8 \pm 0.6$ | $1.3^{+0.6}_{-0.7}$ | 0.029 |

(7) Position maps for the AzTEC sources around the central RG, together with the principal axis of the source distribution (solid line), its 68 per cent confidence interval (two dotted–dashed lines), and the radio jet direction (dashed line). Dashed contours show different noise levels (50 per cent, 75 per cent, and 95 per cent coverage cuts).

(8) Probability distribution of the principal axis described in item 7 and determined by bootstrapping. The vertical line marks the principal axis calculated from the source distribution and the two dotted–dashed lines the 68 per cent confidence interval.

(9) Differential and integrated source counts table.

(10) Catalogue of AzTEC sources with S/N >3.5 for the shallowest maps (TNJ1338−1942 and 4C+41.17) and S/N >3.0 for the rest. The columns show: (1) source ID; (2) source name; (4) S/N of the detection; (4) measured 1.1 mm flux density and error; (5) deboosted 1.1 mm flux density and 68 per cent confidence interval; and (6) probability for the source to have a negative deboosted flux. The catalogue is limited to sources detected within the 50 per cent coverage region of the map.

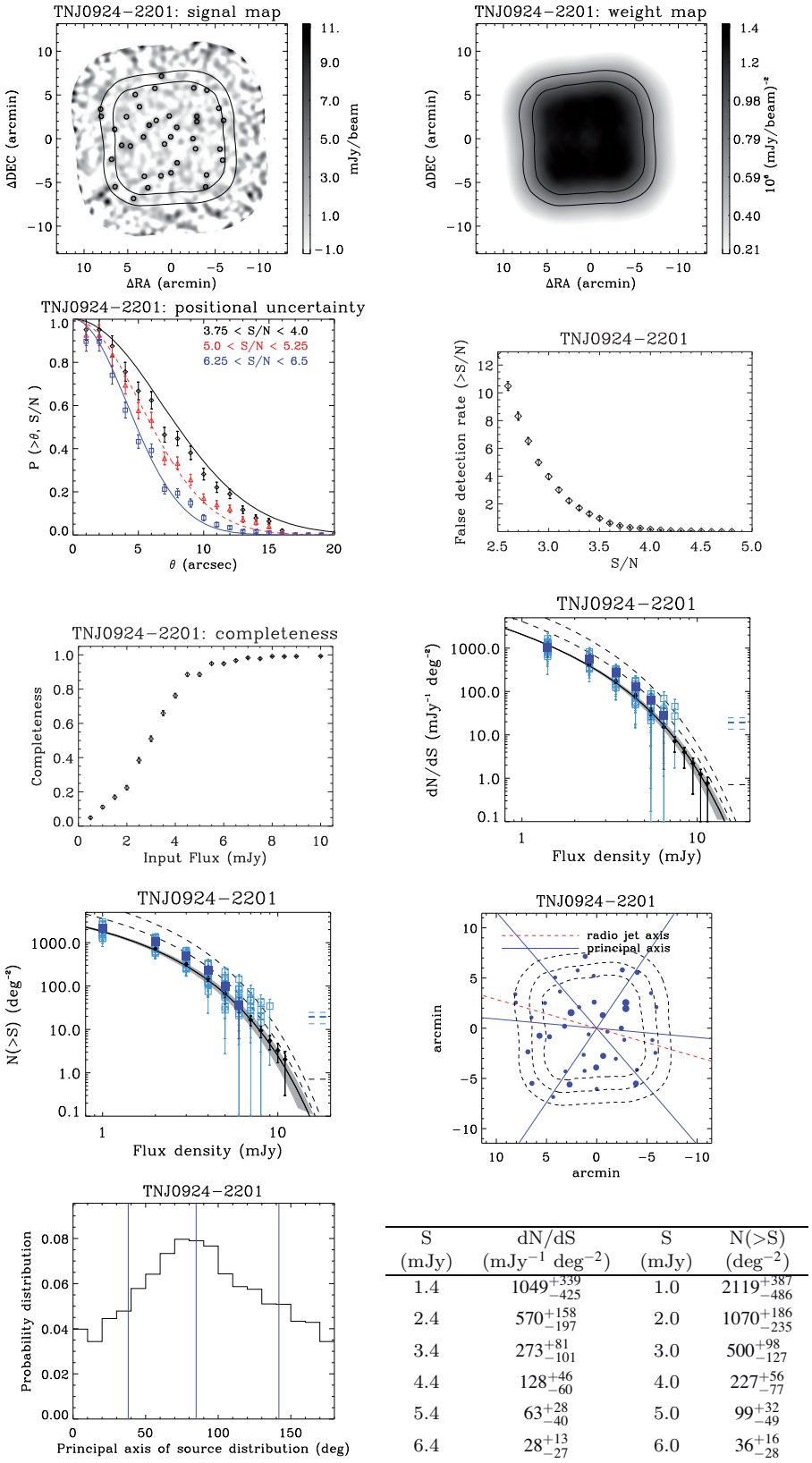


| S (mJy) | dN/dS (mJy$^{-1}$ deg$^{-2}$) | S (mJy) | N(>S) (deg$^{-2}$) |
|---|---|---|---|
| 1.4 | $1049^{+339}_{-425}$ | 1.0 | $2119^{+387}_{-486}$ |
| 2.4 | $570^{+158}_{-197}$ | 2.0 | $1070^{+186}_{-235}$ |
| 3.4 | $273^{+81}_{-101}$ | 3.0 | $500^{+98}_{-127}$ |
| 4.4 | $128^{+46}_{-60}$ | 4.0 | $227^{+56}_{-77}$ |
| 5.4 | $63^{+28}_{-40}$ | 5.0 | $99^{+32}_{-49}$ |
| 6.4 | $28^{+13}_{-27}$ | 6.0 | $36^{+16}_{-28}$ |

**Figure A2.** TNJ0924−2201 products.

**Table A2.** TNJ0924−2201 source catalogue.

| ID | IAU name | S/N | $S_{1.1mm}$ (measured) (mJy) | $S_{1.1mm}$ (deboosted) (mJy) | $P(<0)$ |
|---|---|---|---|---|---|
| 1 | MMJ092430.92−220008.37 | 7.73 | $6.8 \pm 0.9$ | $6.1^{+1.0}_{-0.8}$ | 0.000 |
| 2 | MMJ092407.41−215908.67 | 7.61 | $6.7 \pm 0.9$ | $6.1^{+0.9}_{-0.9}$ | 0.000 |
| 3 | MMJ092407.39−215944.35 | 6.86 | $6.0 \pm 0.9$ | $5.4^{+0.9}_{-0.9}$ | 0.000 |
| 4 | MMJ092403.07−220712.00 | 6.06 | $6.1 \pm 1.0$ | $5.2^{+1.1}_{-0.9}$ | 0.000 |
| 5 | MMJ092444.49−220226.45 | 5.82 | $5.6 \pm 1.0$ | $4.8^{+1.0}_{-0.9}$ | 0.000 |
| 6 | MMJ092417.14−220426.99 | 5.72 | $5.0 \pm 0.9$ | $4.4^{+0.8}_{-0.9}$ | 0.000 |
| 7 | MMJ092420.16−220535.93 | 5.46 | $4.8 \pm 0.9$ | $4.1^{+0.9}_{-0.9}$ | 0.000 |
| 8 | MMJ092431.59−220717.70 | 5.46 | $5.2 \pm 1.0$ | $4.5^{+1.0}_{-1.0}$ | 0.000 |
| 9 | MMJ092417.32−220023.48 | 5.23 | $4.6 \pm 0.9$ | $4.0^{+0.9}_{-0.9}$ | 0.000 |
| 10 | MMJ092409.32−220141.04 | 5.09 | $4.4 \pm 0.9$ | $3.8^{+0.8}_{-0.9}$ | 0.000 |
| 11 | MMJ092424.85−215432.11 | 4.95 | $5.8 \pm 1.2$ | $4.6^{+1.3}_{-1.1}$ | 0.000 |
| 12 | MMJ092433.71−220129.50 | 4.78 | $4.2 \pm 0.9$ | $3.6^{+0.9}_{-0.9}$ | 0.000 |
| 13 | MMJ092440.21−220232.18 | 4.54 | $4.1 \pm 0.9$ | $3.3^{+0.9}_{-0.9}$ | 0.000 |
| 14 | MMJ092408.91−215553.30 | 4.52 | $4.4 \pm 1.0$ | $3.6^{+0.9}_{-1.1}$ | 0.000 |
| 15 | MMJ092420.99−215905.74 | 4.43 | $3.9 \pm 0.9$ | $3.1^{+0.9}_{-0.9}$ | 0.000 |
| 16 | MMJ092449.49−220402.61 | 4.25 | $4.6 \pm 1.1$ | $3.6^{+1.1}_{-1.2}$ | 0.001 |
| 17 | MMJ092402.47−215608.36 | 4.05 | $4.1 \pm 1.0$ | $3.1^{+1.1}_{-1.0}$ | 0.001 |
| 18 | MMJ092420.31−220128.95 | 4.00 | $3.6 \pm 0.9$ | $2.8^{+0.9}_{-0.9}$ | 0.001 |
| 19 | MMJ092447.77−220711.06 | 3.97 | $4.5 \pm 1.1$ | $3.3^{+1.2}_{-1.2}$ | 0.003 |
| 20 | MMJ092402.62−220550.25 | 3.82 | $3.5 \pm 0.9$ | $2.6^{+0.9}_{-1.0}$ | 0.003 |
| 21 | MMJ092354.27−215935.69 | 3.76 | $3.9 \pm 1.0$ | $2.8^{+1.1}_{-1.1}$ | 0.004 |
| 22 | MMJ092355.99−220252.75 | 3.76 | $3.6 \pm 1.0$ | $2.7^{+1.0}_{-1.0}$ | 0.004 |
| 23 | MMJ092438.66−220832.22 | 3.75 | $4.2 \pm 1.1$ | $3.0^{+1.1}_{-1.2}$ | 0.005 |
| 24 | MMJ092454.64−215908.27 | 3.53 | $4.4 \pm 1.2$ | $2.8^{+1.3}_{-1.3}$ | 0.013 |
| 25 | MMJ092437.79−215638.59 | 3.52 | $3.4 \pm 1.0$ | $2.4^{+1.0}_{-1.0}$ | 0.008 |
| 26 | MMJ092408.05−220250.72 | 3.48 | $3.0 \pm 0.9$ | $2.2^{+0.9}_{-0.9}$ | 0.007 |
| 27 | MMJ092442.13−215910.85 | 3.46 | $3.1 \pm 0.9$ | $2.2^{+0.9}_{-0.9}$ | 0.008 |
| 28 | MMJ092428.10−215556.20 | 3.44 | $3.4 \pm 1.0$ | $2.4^{+1.0}_{-1.1}$ | 0.010 |
| 29 | MMJ092435.67−215802.20 | 3.43 | $3.1 \pm 0.9$ | $2.2^{+0.9}_{-0.9}$ | 0.008 |
| 30 | MMJ092454.87−215818.47 | 3.39 | $4.3 \pm 1.3$ | $2.7^{+1.3}_{-1.4}$ | 0.019 |
| 31 | MMJ092354.69−220408.63 | 3.37 | $3.4 \pm 1.0$ | $2.3^{+1.1}_{-1.0}$ | 0.012 |
| 32 | MMJ092425.12−220556.27 | 3.35 | $3.0 \pm 0.9$ | $2.1^{+0.9}_{-0.9}$ | 0.010 |
| 33 | MMJ092447.96−220037.09 | 3.31 | $3.4 \pm 1.0$ | $2.3^{+1.0}_{-1.1}$ | 0.015 |
| 34 | MMJ092433.33−220559.80 | 3.28 | $2.9 \pm 0.9$ | $2.1^{+0.9}_{-0.9}$ | 0.012 |
| 35 | MMJ092423.38−220218.18 | 3.17 | $2.8 \pm 0.9$ | $1.9^{+0.9}_{-0.9}$ | 0.017 |
| 36 | MMJ092427.45−215935.96 | 3.07 | $2.7 \pm 0.9$ | $1.8^{+0.9}_{-0.9}$ | 0.021 |
| 37 | MMJ092356.57−215812.08 | 3.04 | $3.1 \pm 1.0$ | $1.9^{+1.0}_{-1.1}$ | 0.030 |

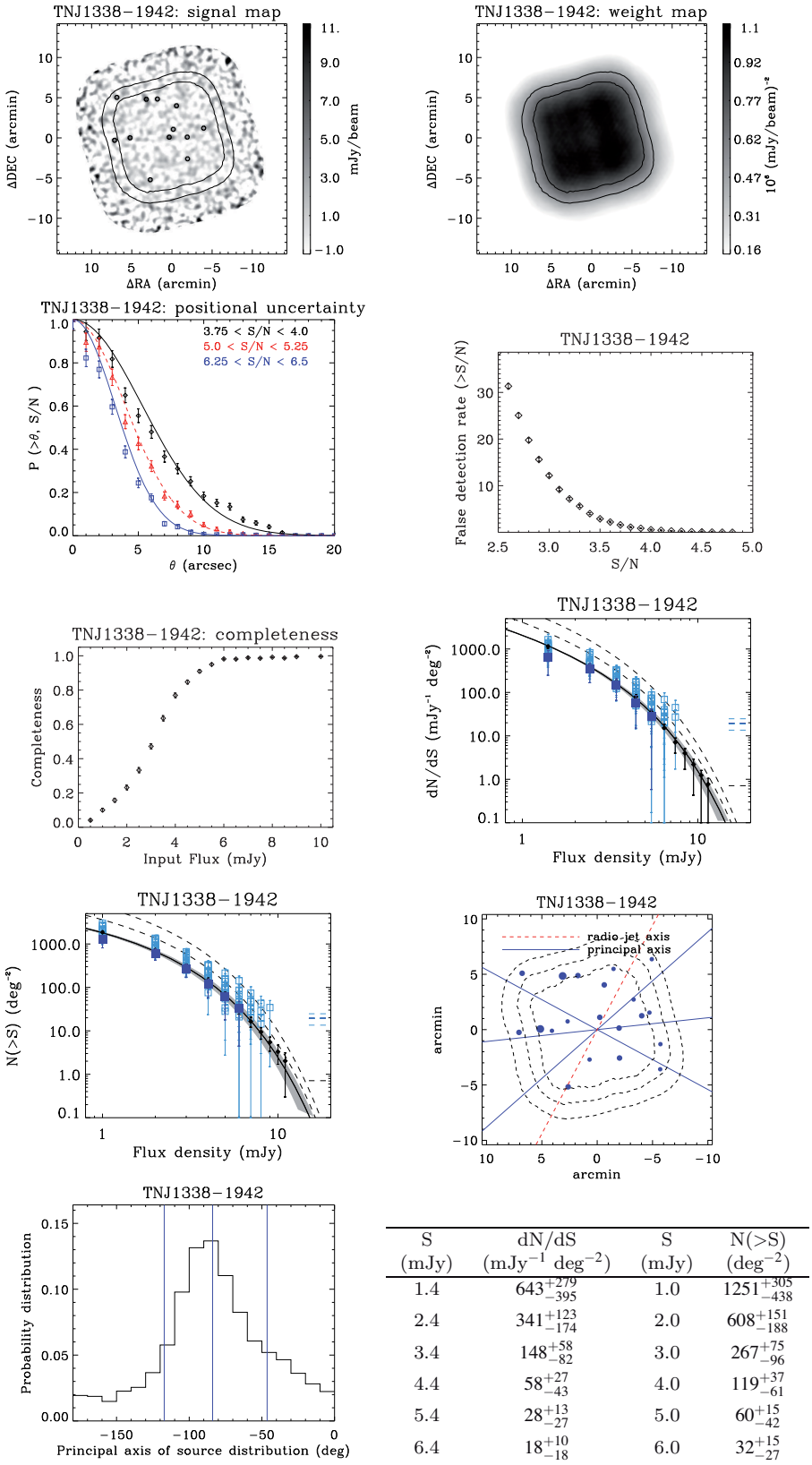


| S (mJy) | dN/dS (mJy$^{-1}$ deg$^{-2}$) | S (mJy) | N(>S) (deg$^{-2}$) |
|---|---|---|---|
| 1.4 | $643^{+279}_{-395}$ | 1.0 | $1251^{+305}_{-438}$ |
| 2.4 | $341^{+123}_{-174}$ | 2.0 | $608^{+151}_{-188}$ |
| 3.4 | $148^{+58}_{-82}$ | 3.0 | $267^{+75}_{-96}$ |
| 4.4 | $58^{+27}_{-43}$ | 4.0 | $119^{+37}_{-61}$ |
| 5.4 | $28^{+13}_{-27}$ | 5.0 | $60^{+15}_{-42}$ |
| 6.4 | $18^{+10}_{-18}$ | 6.0 | $32^{+15}_{-27}$ |

**Figure A3.** TNJ1338−1942 products.

**Table A3.** TNJ1338−1942 source catalogue.

| ID | IAU name | S/N | $S_{1.1mm}$ (measured) (mJy) | $S_{1.1mm}$ (deboosted) (mJy) | $P(<0)$ |
|---|---|---|---|---|---|
| 1 | MMJ133839.49−193742.74 | 7.31 | $7.9 \pm 1.1$ | $6.9^{+1.1}_{-1.0}$ | 0.000 |
| 2 | MMJ133848.07−194230.00 | 6.65 | $6.8 \pm 1.0$ | $6.0^{+1.0}_{-1.1}$ | 0.000 |
| 3 | MMJ133827.35−194225.65 | 6.28 | $6.5 \pm 1.0$ | $5.6^{+1.1}_{-1.1}$ | 0.000 |
| 4 | MMJ133823.52−193831.12 | 4.64 | $4.5 \pm 1.0$ | $3.6^{+1.0}_{-1.0}$ | 0.000 |
| 5 | MMJ133856.25−194248.63 | 4.54 | $5.7 \pm 1.3$ | $4.2^{+1.4}_{-1.3}$ | 0.001 |
| 6 | MMJ133833.62−193740.75 | 4.41 | $4.6 \pm 1.0$ | $3.6^{+1.1}_{-1.1}$ | 0.001 |
| 7 | MMJ133817.83−194225.07 | 4.23 | $4.2 \pm 1.0$ | $3.2^{+1.0}_{-1.0}$ | 0.002 |
| 8 | MMJ133825.23−194127.00 | 4.16 | $4.2 \pm 1.0$ | $3.2^{+1.1}_{-1.1}$ | 0.002 |
| 9 | MMJ133855.03−193728.17 | 3.97 | $5.1 \pm 1.3$ | $3.5^{+1.3}_{-1.5}$ | 0.009 |
| 10 | MMJ133837.39−194743.56 | 3.95 | $4.1 \pm 1.0$ | $3.0^{+1.0}_{-1.1}$ | 0.005 |
| 11 | MMJ133809.13−194118.36 | 3.71 | $3.8 \pm 1.0$ | $2.7^{+1.1}_{-1.2}$ | 0.011 |
| 12 | MMJ133817.65−194507.40 | 3.68 | $3.6 \pm 1.0$ | $2.5^{+1.1}_{-1.1}$ | 0.010 |

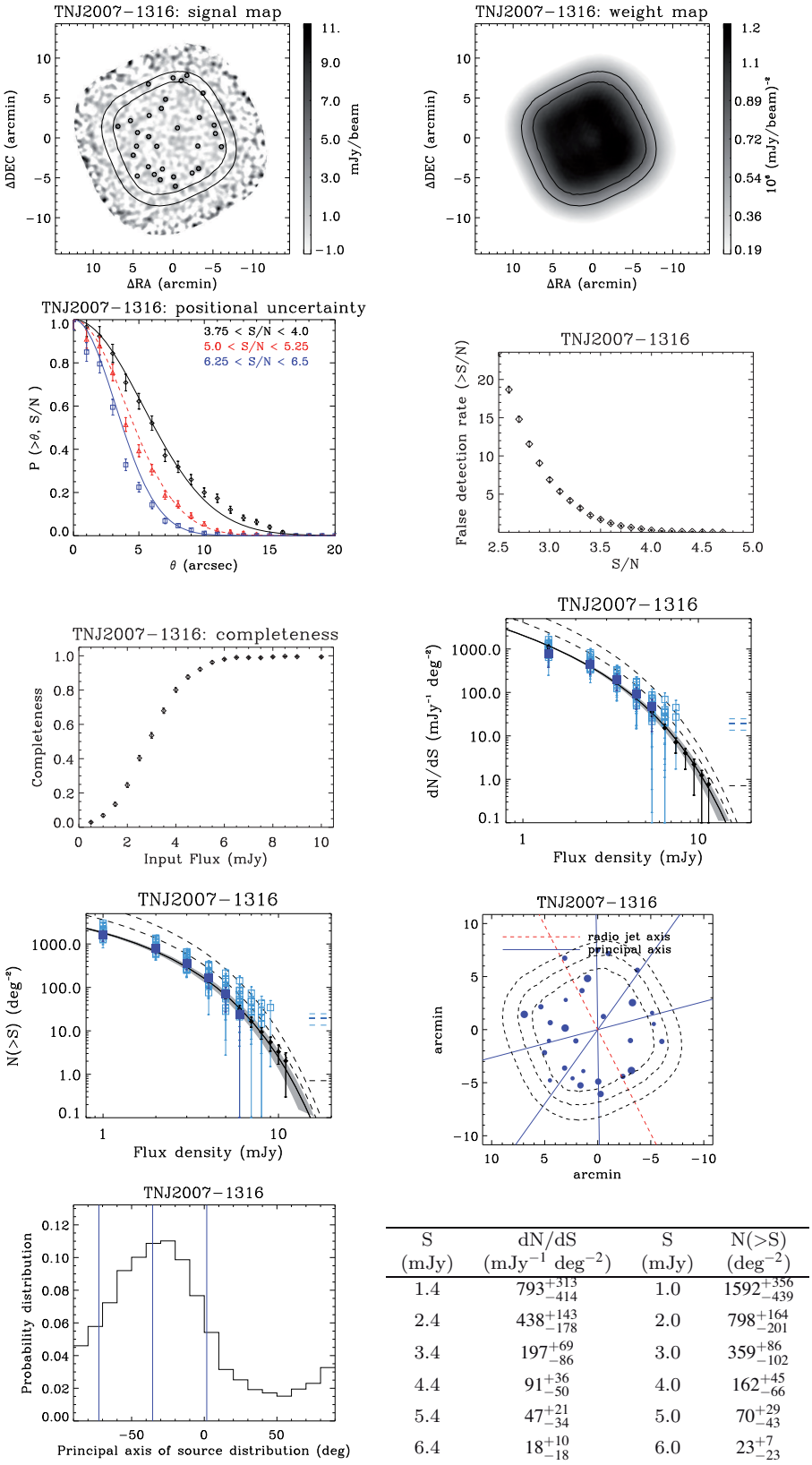


| S (mJy) | dN/dS (mJy$^{-1}$ deg$^{-2}$) | S (mJy) | N(>S) (deg$^{-2}$) |
|---|---|---|---|
| 1.4 | $793^{+313}_{-414}$ | 1.0 | $1592^{+356}_{-439}$ |
| 2.4 | $438^{+143}_{-178}$ | 2.0 | $798^{+164}_{-201}$ |
| 3.4 | $197^{+69}_{-86}$ | 3.0 | $359^{+86}_{-102}$ |
| 4.4 | $91^{+36}_{-50}$ | 4.0 | $162^{+45}_{-66}$ |
| 5.4 | $47^{+21}_{-34}$ | 5.0 | $70^{+29}_{-43}$ |
| 6.4 | $18^{+10}_{-18}$ | 6.0 | $23^{+7}_{-23}$ |

**Figure A4.** TNJ2007−1316 products.

**Table A4.** TNJ2007−1316 source catalogue.

| ID | IAU name | S/N | $S_{1.1mm}$ (measured) (mJy) | $S_{1.1mm}$ (deboosted) (mJy) | $P(<0)$ |
|---|---|---|---|---|---|
| 1 | MMJ200740.16−132034.59 | 7.09 | $6.8 \pm 1.0$ | $6.0^{+1.0}_{-1.0}$ | 0.000 |
| 2 | MMJ200805.85−131634.54 | 6.19 | $5.7 \pm 0.9$ | $5.1^{+0.9}_{-1.0}$ | 0.000 |
| 3 | MMJ200821.68−131517.16 | 6.01 | $6.2 \pm 1.0$ | $5.3^{+1.1}_{-1.0}$ | 0.000 |
| 4 | MMJ200757.17−131154.25 | 5.99 | $5.6 \pm 0.9$ | $4.9^{+1.0}_{-1.0}$ | 0.000 |
| 5 | MMJ200739.78−131410.92 | 5.96 | $5.6 \pm 0.9$ | $4.9^{+0.9}_{-1.0}$ | 0.000 |
| 6 | MMJ200752.11−132247.28 | 5.51 | $5.6 \pm 1.0$ | $4.7^{+1.1}_{-1.0}$ | 0.000 |
| 7 | MMJ200759.91−132158.67 | 5.22 | $4.9 \pm 0.9$ | $4.2^{+0.9}_{-1.0}$ | 0.000 |
| 8 | MMJ200753.03−132137.21 | 4.88 | $4.6 \pm 0.9$ | $3.7^{+1.0}_{-0.9}$ | 0.000 |
| 9 | MMJ200813.84−131853.72 | 4.42 | $4.2 \pm 1.0$ | $3.3^{+1.0}_{-1.0}$ | 0.001 |
| 10 | MMJ200759.32−131302.84 | 4.21 | $3.9 \pm 0.9$ | $3.0^{+0.9}_{-1.0}$ | 0.001 |
| 11 | MMJ200806.05−132020.78 | 4.06 | $3.7 \pm 0.9$ | $2.8^{+1.0}_{-1.0}$ | 0.002 |
| 12 | MMJ200737.87−131107.67 | 4.06 | $4.5 \pm 1.1$ | $3.2^{+1.2}_{-1.2}$ | 0.004 |
| 13 | MMJ200801.71−131747.17 | 4.02 | $3.8 \pm 0.9$ | $2.8^{+1.0}_{-1.0}$ | 0.003 |
| 14 | MMJ200751.02−131529.16 | 3.99 | $3.7 \pm 0.9$ | $2.8^{+0.9}_{-1.0}$ | 0.003 |
| 15 | MMJ200815.25−131434.22 | 3.96 | $3.8 \pm 0.9$ | $2.8^{+1.0}_{-1.1}$ | 0.004 |
| 16 | MMJ200728.39−131750.22 | 3.86 | $4.0 \pm 1.0$ | $2.8^{+1.1}_{-1.1}$ | 0.007 |
| 17 | MMJ200740.55−131745.09 | 3.69 | $3.3 \pm 0.9$ | $2.4^{+1.0}_{-1.0}$ | 0.008 |
| 18 | MMJ200811.62−131604.09 | 3.66 | $3.4 \pm 0.9$ | $2.4^{+1.0}_{-1.0}$ | 0.010 |
| 19 | MMJ200743.48−132107.99 | 3.64 | $3.5 \pm 1.0$ | $2.4^{+1.1}_{-1.0}$ | 0.011 |
| 20 | MMJ200753.29−130913.11 | 3.63 | $4.2 \pm 1.2$ | $2.8^{+1.2}_{-1.4}$ | 0.018 |
| 21 | MMJ200806.00−130959.22 | 3.60 | $4.5 \pm 1.2$ | $2.8^{+1.3}_{-1.4}$ | 0.022 |
| 22 | MMJ200749.12−130932.94 | 3.57 | $4.0 \pm 1.1$ | $2.7^{+1.1}_{-1.3}$ | 0.019 |
| 23 | MMJ200732.16−131508.39 | 3.45 | $3.5 \pm 1.0$ | $2.3^{+1.1}_{-1.1}$ | 0.021 |
| 24 | MMJ200731.48−131611.49 | 3.40 | $3.4 \pm 1.0$ | $2.2^{+1.1}_{-1.1}$ | 0.023 |
| 25 | MMJ200812.13−131746.26 | 3.33 | $3.1 \pm 0.9$ | $2.1^{+1.0}_{-1.0}$ | 0.025 |
| 26 | MMJ200802.98−132118.79 | 3.30 | $3.1 \pm 0.9$ | $2.0^{+1.0}_{-1.0}$ | 0.027 |
| 27 | MMJ200811.74−132130.36 | 3.22 | $3.2 \pm 1.0$ | $2.0^{+1.1}_{-1.1}$ | 0.037 |
| 28 | MMJ200746.18−130854.15 | 3.18 | $4.0 \pm 1.2$ | $2.2^{+1.3}_{-1.5}$ | 0.060 |
| 29 | MMJ200758.81−132037.89 | 3.16 | $2.9 \pm 0.9$ | $1.8^{+1.0}_{-1.0}$ | 0.036 |
| 30 | MMJ200805.62−131355.55 | 3.13 | $2.9 \pm 0.9$ | $1.8^{+1.0}_{-1.0}$ | 0.039 |

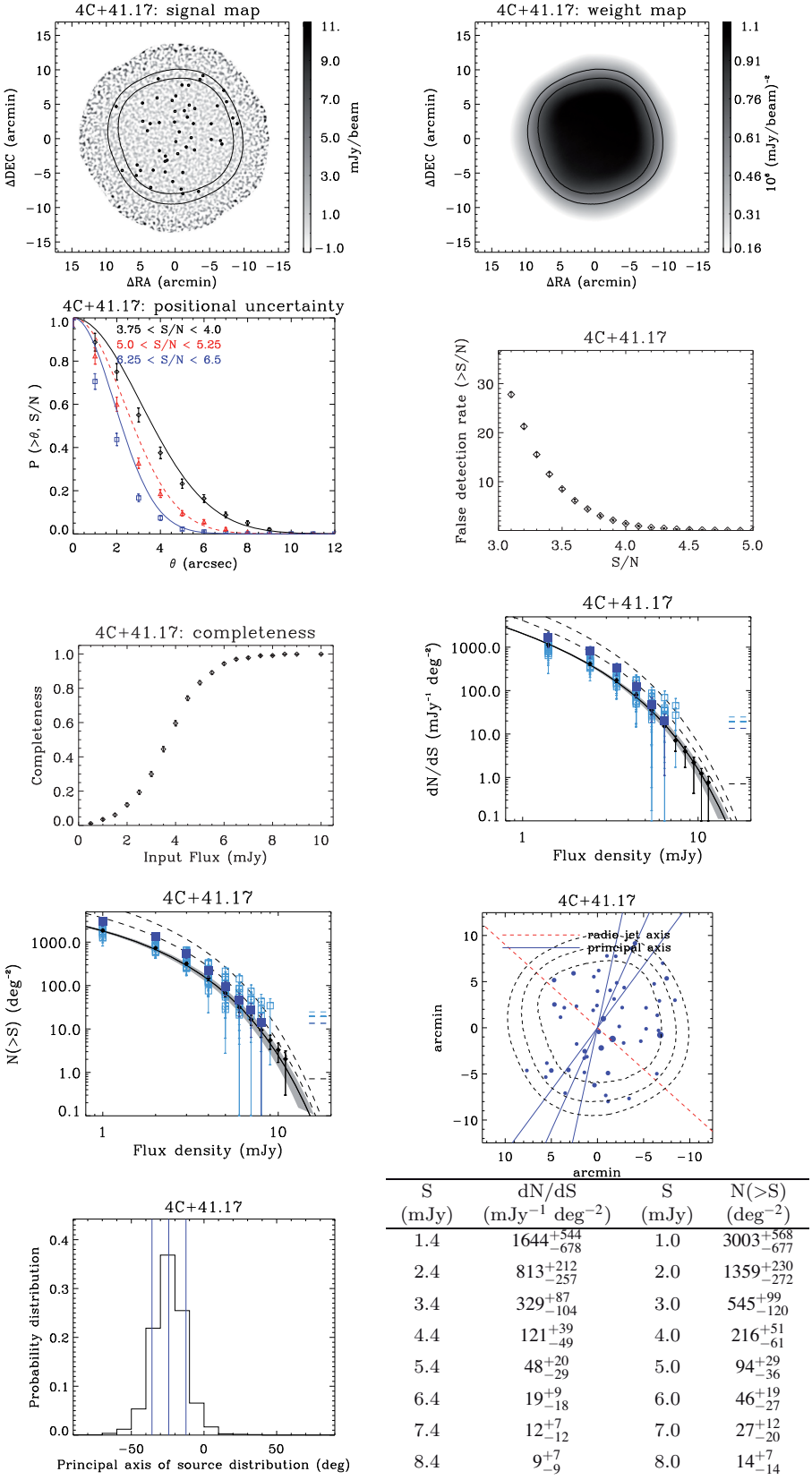


| S (mJy) | dN/dS (mJy$^{-1}$ deg$^{-2}$) | S (mJy) | N(>S) (deg$^{-2}$) |
|---|---|---|---|
| 1.4 | $1644^{+544}_{-678}$ | 1.0 | $3003^{+568}_{-677}$ |
| 2.4 | $813^{+212}_{-257}$ | 2.0 | $1359^{+230}_{-272}$ |
| 3.4 | $329^{+87}_{-104}$ | 3.0 | $545^{+99}_{-120}$ |
| 4.4 | $121^{+39}_{-49}$ | 4.0 | $216^{+51}_{-61}$ |
| 5.4 | $48^{+20}_{-29}$ | 5.0 | $94^{+29}_{-36}$ |
| 6.4 | $19^{+9}_{-18}$ | 6.0 | $46^{+19}_{-27}$ |
| 7.4 | $12^{+7}_{-12}$ | 7.0 | $27^{+12}_{-20}$ |
| 8.4 | $9^{+7}_{-9}$ | 8.0 | $14^{+7}_{-14}$ |

**Figure A5.** 4C+41.17 products.

**Table A5.** 4C+41.17 source catalogue.

| ID | IAU name | S/N | $S_{1.1mm}$ (measured) (mJy) | $S_{1.1mm}$ (deboosted) (mJy) | $P(<0)$ |
|---|---|---|---|---|---|
| 1 | MMJ065043.59+412918.63 | 8.93 | $8.9 \pm 1.0$ | $8.2^{+1.0}_{-1.0}$ | 0.000 |
| 2 | MMJ065015.97+412944.58 | 8.50 | $8.7 \pm 1.0$ | $8.0^{+1.0}_{-1.1}$ | 0.000 |
| 3 | MMJ065050.17+412820.22 | 6.33 | $6.3 \pm 1.0$ | $5.5^{+1.0}_{-1.0}$ | 0.000 |
| 4 | MMJ065048.98+413130.17 | 6.00 | $5.9 \pm 1.0$ | $5.0^{+1.1}_{-0.9}$ | 0.000 |
| 5 | MMJ065030.59+413940.08 | 5.94 | $7.9 \pm 1.3$ | $6.5^{+1.4}_{-1.4}$ | 0.000 |
| 6 | MMJ065117.29+413302.93 | 5.89 | $5.9 \pm 1.0$ | $5.0^{+1.0}_{-1.1}$ | 0.000 |
| 7 | MMJ065106.22+413625.46 | 5.54 | $5.5 \pm 1.0$ | $4.6^{+1.0}_{-1.1}$ | 0.000 |
| 8 | MMJ065117.51+413541.19 | 5.38 | $5.4 \pm 1.0$ | $4.5^{+1.0}_{-1.1}$ | 0.000 |
| 9 | MMJ065046.25+412536.89 | 5.34 | $5.4 \pm 1.0$ | $4.4^{+1.1}_{-1.0}$ | 0.000 |
| 10 | MMJ065012.23+413552.48 | 4.93 | $6.2 \pm 1.3$ | $4.7^{+1.4}_{-1.3}$ | 0.002 |
| 11 | MMJ065059.74+412759.11 | 4.70 | $4.7 \pm 1.0$ | $3.7^{+1.1}_{-1.1}$ | 0.002 |
| 12 | MMJ065119.02+412553.42 | 4.69 | $5.0 \pm 1.1$ | $3.8^{+1.2}_{-1.1}$ | 0.002 |
| 13 | MMJ065051.62+413004.98 | 4.68 | $4.7 \pm 1.0$ | $3.6^{+1.1}_{-1.1}$ | 0.002 |
| 14 | MMJ065054.07+412418.34 | 4.54 | $4.7 \pm 1.0$ | $3.6^{+1.1}_{-1.1}$ | 0.004 |
| 15 | MMJ065109.16+412557.07 | 4.54 | $4.6 \pm 1.0$ | $3.6^{+1.1}_{-1.2}$ | 0.004 |
| 16 | MMJ065111.56+413241.85 | 4.44 | $4.4 \pm 1.0$ | $3.4^{+1.1}_{-1.1}$ | 0.005 |
| 17 | MMJ065044.99+413434.79 | 4.39 | $4.3 \pm 1.0$ | $3.2^{+1.1}_{-1.1}$ | 0.006 |
| 18 | MMJ065024.19+413024.57 | 4.34 | $4.3 \pm 1.0$ | $3.2^{+1.1}_{-1.1}$ | 0.007 |
| 19 | MMJ065051.64+413643.48 | 4.09 | $4.0 \pm 1.0$ | $2.9^{+1.1}_{-1.2}$ | 0.015 |
| 20 | MMJ065046.85+413818.59 | 4.07 | $4.4 \pm 1.1$ | $3.1^{+1.2}_{-1.3}$ | 0.020 |
| 21 | MMJ065122.25+412510.61 | 4.06 | $4.6 \pm 1.1$ | $3.2^{+1.3}_{-1.4}$ | 0.024 |
| 22 | MMJ065104.40+412846.21 | 4.05 | $4.1 \pm 1.0$ | $2.9^{+1.1}_{-1.2}$ | 0.018 |
| 23 | MMJ065047.55+412311.28 | 3.97 | $4.4 \pm 1.1$ | $3.1^{+1.3}_{-1.4}$ | 0.029 |
| 24 | MMJ065059.98+412713.65 | 3.97 | $4.0 \pm 1.0$ | $2.8^{+1.2}_{-1.2}$ | 0.024 |
| 25 | MMJ065133.19+412553.49 | 3.96 | $5.3 \pm 1.3$ | $3.4^{+1.7}_{-1.8}$ | 0.047 |
| 26 | MMJ065059.91+412540.87 | 3.94 | $4.0 \pm 1.0$ | $2.8^{+1.2}_{-1.3}$ | 0.026 |
| 27 | MMJ065007.46+413330.58 | 3.94 | $4.9 \pm 1.2$ | $3.2^{+1.5}_{-1.6}$ | 0.041 |
| 28 | MMJ065038.03+413242.61 | 3.94 | $3.9 \pm 1.0$ | $2.7^{+1.1}_{-1.2}$ | 0.024 |
| 29 | MMJ065111.02+412326.26 | 3.90 | $4.4 \pm 1.1$ | $2.9^{+1.4}_{-1.4}$ | 0.037 |
| 30 | MMJ065041.20+413523.47 | 3.89 | $3.8 \pm 1.0$ | $2.6^{+1.1}_{-1.2}$ | 0.027 |
| 31 | MMJ065034.10+412251.31 | 3.87 | $4.7 \pm 1.2$ | $3.1^{+1.5}_{-1.7}$ | 0.048 |
| 32 | MMJ065041.74+413816.19 | 3.86 | $4.1 \pm 1.1$ | $2.8^{+1.3}_{-1.4}$ | 0.036 |
| 33 | MMJ065032.84+413906.92 | 3.77 | $4.6 \pm 1.2$ | $2.8^{+1.6}_{-1.7}$ | 0.059 |
| 34 | MMJ065014.49+413731.20 | 3.76 | $5.2 \pm 1.4$ | $3.1^{+1.8}_{-2.3}$ | 0.081 |
| 35 | MMJ065104.52+413251.50 | 3.76 | $3.7 \pm 1.0$ | $2.5^{+1.2}_{-1.3}$ | 0.040 |
| 36 | MMJ065042.71+413338.53 | 3.76 | $3.7 \pm 1.0$ | $2.5^{+1.2}_{-1.3}$ | 0.039 |
| 37 | MMJ065024.19+413240.93 | 3.75 | $3.7 \pm 1.0$ | $2.5^{+1.2}_{-1.3}$ | 0.040 |
| 38 | MMJ065058.43+412722.71 | 3.75 | $3.8 \pm 1.0$ | $2.5^{+1.3}_{-1.3}$ | 0.043 |
| 39 | MMJ065019.48+413516.84 | 3.70 | $3.9 \pm 1.1$ | $2.5^{+1.4}_{-1.4}$ | 0.053 |
| 40 | MMJ065113.74+413140.12 | 3.70 | $3.7 \pm 1.0$ | $2.5^{+1.2}_{-1.4}$ | 0.048 |
| 41 | MMJ065016.99+413014.00 | 3.63 | $3.7 \pm 1.0$ | $2.4^{+1.3}_{-1.4}$ | 0.058 |
| 42 | MMJ065052.31+413429.05 | 3.61 | $3.5 \pm 1.0$ | $2.3^{+1.2}_{-1.4}$ | 0.057 |
| 43 | MMJ065037.19+412852.58 | 3.59 | $3.6 \pm 1.0$ | $2.3^{+1.2}_{-1.4}$ | 0.060 |
| 44 | MMJ065052.64+413256.14 | 3.59 | $3.5 \pm 1.0$ | $2.3^{+1.2}_{-1.4}$ | 0.060 |
| 45 | MMJ065039.75+413039.76 | 3.58 | $3.5 \pm 1.0$ | $2.3^{+1.2}_{-1.5}$ | 0.061 |
| 46 | MMJ065036.89+413452.65 | 3.57 | $3.5 \pm 1.0$ | $2.2^{+1.2}_{-1.4}$ | 0.061 |
| 47 | MMJ065137.93+413510.69 | 3.57 | $4.7 \pm 1.3$ | $2.6^{+1.4}_{-2.5}$ | 0.105 |
| 48 | MMJ065121.62+412641.57 | 3.56 | $3.8 \pm 1.1$ | $2.3^{+1.4}_{-1.6}$ | 0.074 |
| 49 | MMJ065046.23+412232.04 | 3.55 | $4.2 \pm 1.2$ | $2.5^{+1.3}_{-2.1}$ | 0.090 |
| 50 | MMJ065054.45+413603.25 | 3.54 | $3.5 \pm 1.0$ | $2.2^{+1.2}_{-1.5}$ | 0.066 |
| 51 | MMJ065105.33+413912.76 | 3.53 | $4.3 \pm 1.2$ | $2.5^{+1.3}_{-2.3}$ | 0.100 |

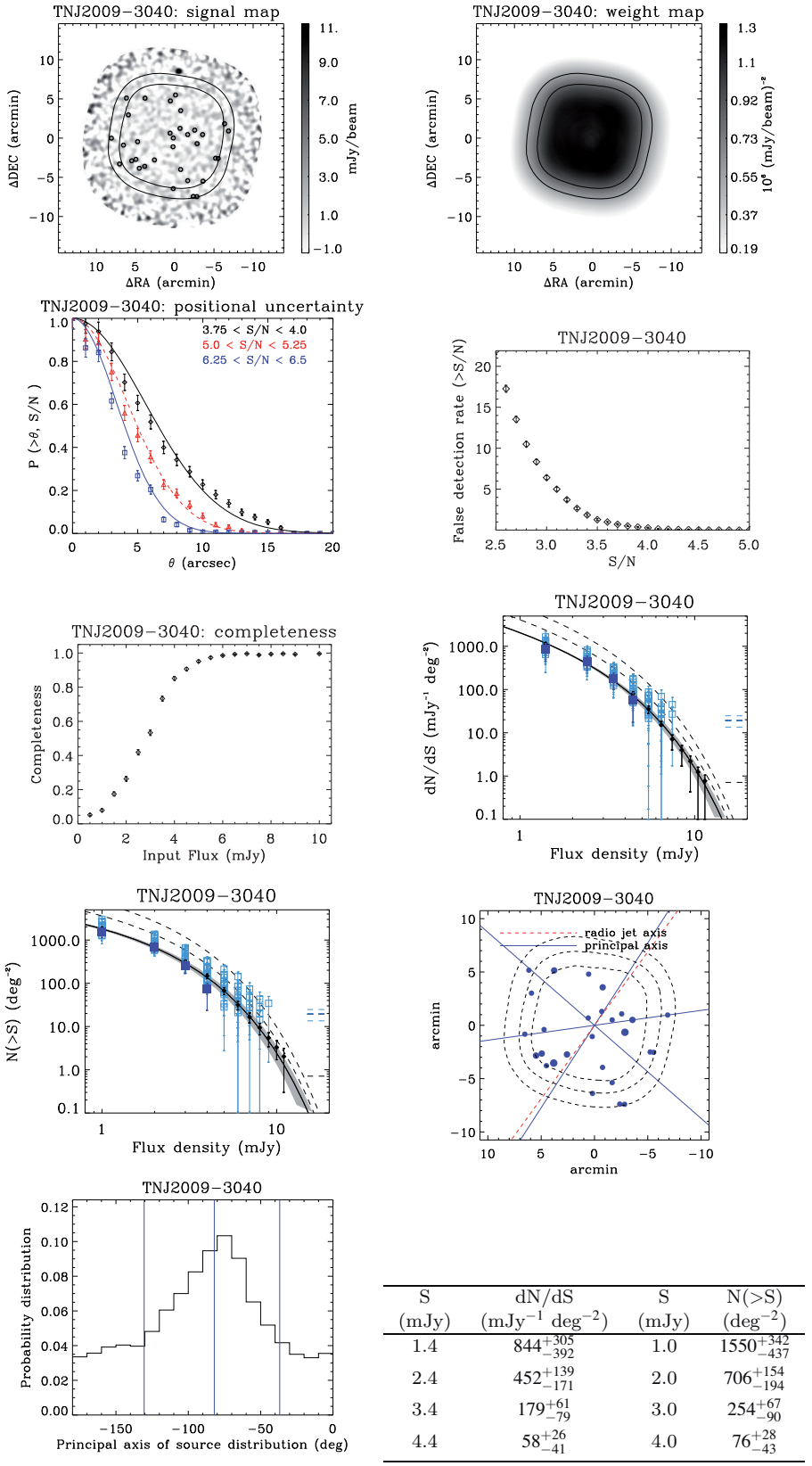


| S (mJy) | dN/dS (mJy$^{-1}$ deg$^{-2}$) | S (mJy) | N(>S) (deg$^{-2}$) |
|---|---|---|---|
| 1.4 | $844^{+305}_{-392}$ | 1.0 | $1550^{+342}_{-437}$ |
| 2.4 | $452^{+139}_{-171}$ | 2.0 | $706^{+154}_{-194}$ |
| 3.4 | $179^{+61}_{-79}$ | 3.0 | $254^{+67}_{-90}$ |
| 4.4 | $58^{+26}_{-41}$ | 4.0 | $76^{+28}_{-43}$ |

**Figure A6.** TNJ2009−3040 products.

**Table A6.** TNJ2009−3040 source catalogue.

| ID | IAU name | S/N | $S_{1.1mm}$ (measured) (mJy) | $S_{1.1mm}$ (deboosted) (mJy) | $P(<0)$ |
|---|---|---|---|---|---|
| 1 | MMJ201005.87−304339.86 | 5.85 | $5.5 \pm 0.9$ | $4.8^{+0.9}_{-1.0}$ | 0.000 |
| 2 | MMJ200934.77−304046.39 | 5.24 | $4.8 \pm 0.9$ | $4.0^{+1.0}_{-0.9}$ | 0.000 |
| 3 | MMJ200931.51−303936.94 | 4.58 | $4.2 \pm 0.9$ | $3.4^{+1.0}_{-0.9}$ | 0.000 |
| 4 | MMJ201013.58−304257.78 | 4.44 | $4.3 \pm 1.0$ | $3.4^{+1.0}_{-1.0}$ | 0.001 |
| 5 | MMJ201000.08−304251.29 | 4.37 | $4.0 \pm 0.9$ | $3.1^{+0.9}_{-1.0}$ | 0.001 |
| 6 | MMJ201005.65−303458.52 | 4.27 | $4.1 \pm 1.0$ | $3.2^{+1.0}_{-1.0}$ | 0.001 |
| 7 | MMJ200944.50−303633.67 | 4.25 | $3.9 \pm 0.9$ | $3.0^{+0.9}_{-0.9}$ | 0.001 |
| 8 | MMJ201011.09−304246.30 | 4.17 | $3.9 \pm 0.9$ | $3.0^{+1.0}_{-1.0}$ | 0.002 |
| 9 | MMJ200916.16−303909.54 | 3.90 | $4.6 \pm 1.2$ | $3.1^{+1.3}_{-1.2}$ | 0.008 |
| 10 | MMJ200948.93−304630.51 | 3.78 | $4.1 \pm 1.1$ | $2.8^{+1.2}_{-1.2}$ | 0.009 |
| 11 | MMJ200950.82−303926.14 | 3.76 | $3.5 \pm 0.9$ | $2.5^{+1.0}_{-1.0}$ | 0.007 |
| 12 | MMJ200940.36−303936.91 | 3.74 | $3.4 \pm 0.9$ | $2.5^{+0.9}_{-1.0}$ | 0.007 |
| 13 | MMJ200950.62−303519.42 | 3.65 | $3.4 \pm 0.9$ | $2.4^{+1.0}_{-1.0}$ | 0.009 |
| 14 | MMJ201015.55−303706.34 | 3.64 | $3.7 \pm 1.0$ | $2.6^{+1.0}_{-1.2}$ | 0.012 |
| 15 | MMJ200937.03−304730.59 | 3.63 | $4.7 \pm 1.3$ | $2.9^{+1.4}_{-1.4}$ | 0.021 |
| 16 | MMJ200948.89−304003.17 | 3.55 | $3.3 \pm 0.9$ | $2.4^{+1.0}_{-1.1}$ | 0.013 |
| 17 | MMJ200934.92−304731.70 | 3.48 | $4.6 \pm 1.3$ | $2.6^{+1.5}_{-1.4}$ | 0.032 |
| 18 | MMJ200923.77−304237.52 | 3.44 | $3.5 \pm 1.0$ | $2.4^{+1.1}_{-1.2}$ | 0.021 |
| 19 | MMJ201010.08−304031.14 | 3.40 | $3.1 \pm 0.9$ | $2.1^{+1.0}_{-1.0}$ | 0.018 |
| 20 | MMJ200936.20−303903.12 | 3.36 | $3.0 \pm 0.9$ | $2.0^{+1.0}_{-1.0}$ | 0.020 |
| 21 | MMJ201018.47−304057.25 | 3.30 | $3.4 \pm 1.0$ | $2.1^{+1.1}_{-1.1}$ | 0.030 |
| 22 | MMJ200949.05−304110.42 | 3.27 | $3.0 \pm 0.9$ | $2.0^{+1.0}_{-1.0}$ | 0.026 |
| 23 | MMJ201016.68−303457.41 | 3.25 | $3.7 \pm 1.1$ | $2.2^{+1.1}_{-1.4}$ | 0.041 |
| 24 | MMJ200922.24−304239.64 | 3.17 | $3.4 \pm 1.1$ | $2.0^{+1.1}_{-1.2}$ | 0.044 |
| 25 | MMJ200940.35−304529.78 | 3.17 | $3.1 \pm 1.0$ | $1.9^{+1.0}_{-1.1}$ | 0.038 |
| 26 | MMJ201009.08−304354.60 | 3.13 | $3.0 \pm 1.0$ | $1.8^{+1.0}_{-1.1}$ | 0.040 |
| 27 | MMJ200944.55−304404.05 | 3.08 | $2.8 \pm 0.9$ | $1.7^{+0.9}_{-1.0}$ | 0.041 |
| 28 | MMJ200931.28−304533.67 | 3.07 | $3.3 \pm 1.1$ | $1.8^{+1.1}_{-1.2}$ | 0.055 |
| 29 | MMJ200944.90−303849.26 | 3.07 | $2.8 \pm 0.9$ | $1.7^{+1.0}_{-1.0}$ | 0.044 |
| 30 | MMJ200918.47−303813.84 | 3.05 | $3.3 \pm 1.1$ | $1.8^{+1.2}_{-1.2}$ | 0.059 |
| 31 | MMJ200947.58−303434.03 | 3.03 | $2.9 \pm 1.0$ | $1.7^{+1.0}_{-1.1}$ | 0.051 |
| 32 | MMJ201025.64−304004.00 | 3.02 | $3.8 \pm 1.3$ | $1.9^{+1.2}_{-1.5}$ | 0.079 |
| 33 | MMJ201020.82−304322.13 | 3.02 | $3.4 \pm 1.1$ | $1.8^{+1.2}_{-1.3}$ | 0.067 |

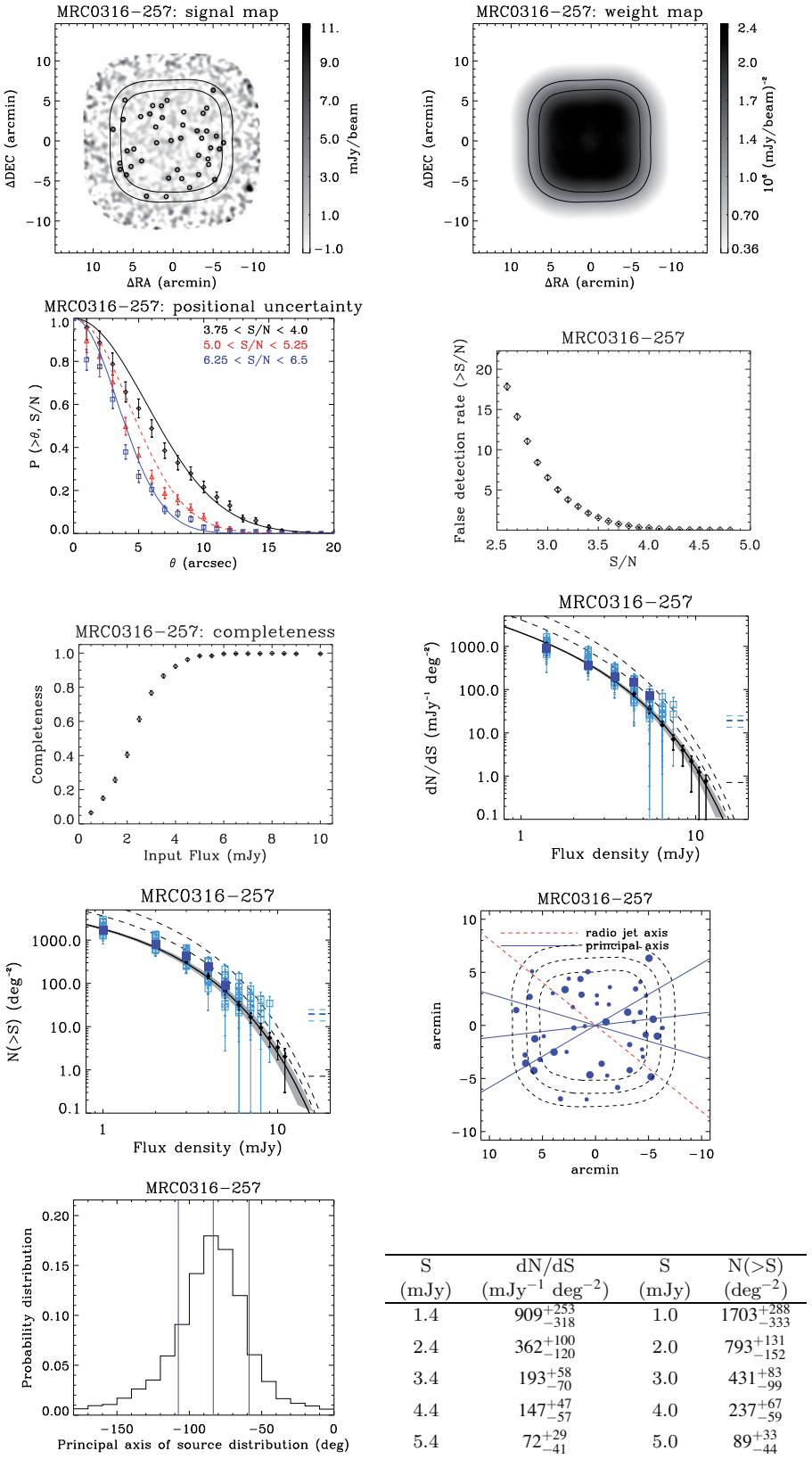


| S (mJy) | dN/dS (mJy$^{-1}$ deg$^{-2}$) | S (mJy) | N(>S) (deg$^{-2}$) |
|---|---|---|---|
| 1.4 | $909^{+253}_{-318}$ | 1.0 | $1703^{+288}_{-333}$ |
| 2.4 | $362^{+100}_{-120}$ | 2.0 | $793^{+131}_{-152}$ |
| 3.4 | $193^{+58}_{-70}$ | 3.0 | $431^{+83}_{-99}$ |
| 4.4 | $147^{+47}_{-57}$ | 4.0 | $237^{+67}_{-59}$ |
| 5.4 | $72^{+29}_{-41}$ | 5.0 | $89^{+33}_{-44}$ |

**Figure A7.** MRC0316−257 products.

**Table A7.** MRC0316−257 source catalogue.

| ID | IAU name | S/N | $S_{1.1mm}$ (measured) (mJy) | $S_{1.1mm}$ (deboosted) (mJy) | $P(<0)$ |
|---|---|---|---|---|---|
| 1 | MMJ031758.69−253355.57 | 7.88 | $5.2 \pm 0.7$ | $4.9^{+0.7}_{-0.7}$ | 0.000 |
| 2 | MMJ031837.94−253925.24 | 7.81 | $6.0 \pm 0.8$ | $5.6^{+0.8}_{-0.8}$ | 0.000 |
| 3 | MMJ031824.87−253147.88 | 7.72 | $5.1 \pm 0.7$ | $4.7^{+0.7}_{-0.7}$ | 0.000 |
| 4 | MMJ031814.48−253949.57 | 7.37 | $5.0 \pm 0.7$ | $4.6^{+0.7}_{-0.7}$ | 0.000 |
| 5 | MMJ031746.31−253611.03 | 7.34 | $5.5 \pm 0.8$ | $5.1^{+0.7}_{-0.8}$ | 0.000 |
| 6 | MMJ031748.05−253435.04 | 7.17 | $5.2 \pm 0.7$ | $4.7^{+0.8}_{-0.7}$ | 0.000 |
| 7 | MMJ031807.76−253450.27 | 6.94 | $4.7 \pm 0.7$ | $4.3^{+0.7}_{-0.7}$ | 0.000 |
| 8 | MMJ031748.93−254001.09 | 6.92 | $5.4 \pm 0.8$ | $4.9^{+0.8}_{-0.8}$ | 0.000 |
| 9 | MMJ031829.48−253740.90 | 6.89 | $4.6 \pm 0.7$ | $4.2^{+0.7}_{-0.7}$ | 0.000 |
| 10 | MMJ031841.34−253843.86 | 6.81 | $5.5 \pm 0.8$ | $5.0^{+0.9}_{-0.8}$ | 0.000 |
| 11 | MMJ031749.77−252850.49 | 6.71 | $5.9 \pm 0.9$ | $5.2^{+0.9}_{-0.9}$ | 0.000 |
| 12 | MMJ031837.49−253625.87 | 6.61 | $4.8 \pm 0.7$ | $4.3^{+0.7}_{-0.7}$ | 0.000 |
| 13 | MMJ031809.60−253846.59 | 6.39 | $4.2 \pm 0.7$ | $3.8^{+0.7}_{-0.7}$ | 0.000 |
| 14 | MMJ031751.18−253602.45 | 6.22 | $4.3 \pm 0.7$ | $3.9^{+0.7}_{-0.7}$ | 0.000 |
| 15 | MMJ031757.85−253923.07 | 6.05 | $4.1 \pm 0.7$ | $3.7^{+0.7}_{-0.7}$ | 0.000 |
| 16 | MMJ031818.43−253047.87 | 5.97 | $4.0 \pm 0.7$ | $3.6^{+0.7}_{-0.7}$ | 0.000 |
| 17 | MMJ031817.97−253216.43 | 5.73 | $3.8 \pm 0.7$ | $3.4^{+0.7}_{-0.7}$ | 0.000 |
| 18 | MMJ031839.66−253229.04 | 5.58 | $4.3 \pm 0.8$ | $3.8^{+0.7}_{-0.8}$ | 0.000 |
| 19 | MMJ031813.14−253508.26 | 5.51 | $3.8 \pm 0.7$ | $3.3^{+0.7}_{-0.7}$ | 0.000 |
| 20 | MMJ031845.28−253343.65 | 5.27 | $4.8 \pm 0.9$ | $4.0^{+0.9}_{-0.9}$ | 0.000 |
| 21 | MMJ031757.87−253658.77 | 5.02 | $3.3 \pm 0.7$ | $2.9^{+0.7}_{-0.7}$ | 0.000 |
| 22 | MMJ031826.79−254205.03 | 4.88 | $4.2 \pm 0.9$ | $3.5^{+0.9}_{-0.9}$ | 0.000 |
| 23 | MMJ031815.35−253007.18 | 4.88 | $3.4 \pm 0.7$ | $2.9^{+0.7}_{-0.7}$ | 0.000 |
| 24 | MMJ031835.33−253822.69 | 4.65 | $3.3 \pm 0.7$ | $2.8^{+0.7}_{-0.7}$ | 0.000 |
| 25 | MMJ031821.17−253524.92 | 4.60 | $3.1 \pm 0.7$ | $2.6^{+0.7}_{-0.7}$ | 0.000 |
| 26 | MMJ031802.89−254101.09 | 4.31 | $3.2 \pm 0.7$ | $2.6^{+0.8}_{-0.8}$ | 0.001 |
| 27 | MMJ031753.39−253356.73 | 4.21 | $2.8 \pm 0.7$ | $2.3^{+0.7}_{-0.7}$ | 0.001 |
| 28 | MMJ031841.57−253757.12 | 4.21 | $3.4 \pm 0.8$ | $2.7^{+0.8}_{-0.9}$ | 0.001 |
| 29 | MMJ031755.39−253143.91 | 4.11 | $2.8 \pm 0.7$ | $2.2^{+0.7}_{-0.7}$ | 0.001 |
| 30 | MMJ031823.31−253046.15 | 3.93 | $2.7 \pm 0.7$ | $2.1^{+0.7}_{-0.7}$ | 0.002 |
| 31 | MMJ031752.69−253725.95 | 3.92 | $2.7 \pm 0.7$ | $2.1^{+0.7}_{-0.7}$ | 0.002 |
| 32 | MMJ031806.14−253133.87 | 3.69 | $2.4 \pm 0.7$ | $1.9^{+0.7}_{-0.7}$ | 0.004 |
| 33 | MMJ031744.03−253524.33 | 3.52 | $2.8 \pm 0.8$ | $2.1^{+0.8}_{-0.9}$ | 0.010 |
| 34 | MMJ031821.62−253326.57 | 3.46 | $2.3 \pm 0.7$ | $1.7^{+0.7}_{-0.7}$ | 0.008 |
| 35 | MMJ031829.95−253208.21 | 3.45 | $2.3 \pm 0.7$ | $1.7^{+0.7}_{-0.7}$ | 0.009 |
| 36 | MMJ031756.13−253450.42 | 3.44 | $2.3 \pm 0.7$ | $1.7^{+0.7}_{-0.7}$ | 0.009 |
| 37 | MMJ031833.78−253611.52 | 3.38 | $2.3 \pm 0.7$ | $1.7^{+0.7}_{-0.7}$ | 0.011 |
| 38 | MMJ031838.68−253004.80 | 3.37 | $2.7 \pm 0.8$ | $1.9^{+0.9}_{-0.8}$ | 0.016 |
| 39 | MMJ031752.32−253807.67 | 3.36 | $2.3 \pm 0.7$ | $1.7^{+0.7}_{-0.7}$ | 0.012 |
| 40 | MMJ031815.85−254208.51 | 3.34 | $2.8 \pm 0.8$ | $2.0^{+0.9}_{-0.9}$ | 0.019 |
| 41 | MMJ031753.39−253104.96 | 3.31 | $2.3 \pm 0.7$ | $1.6^{+0.7}_{-0.7}$ | 0.014 |
| 42 | MMJ031806.56−253311.81 | 3.06 | $2.0 \pm 0.7$ | $1.4^{+0.7}_{-0.7}$ | 0.026 |
| 43 | MMJ031807.22−253953.68 | 3.03 | $2.1 \pm 0.7$ | $1.4^{+0.8}_{-0.7}$ | 0.029 |

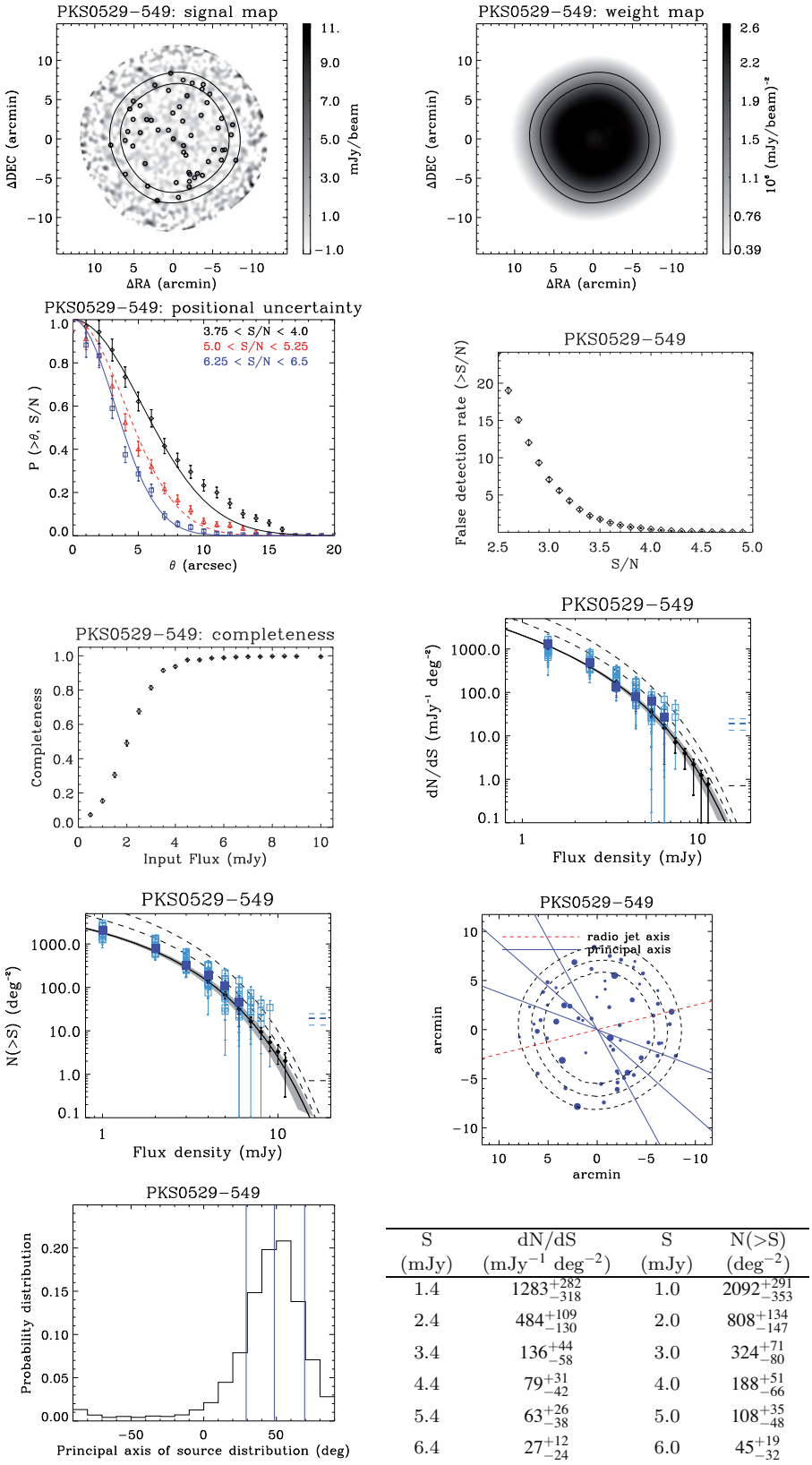


| S (mJy) | dN/dS (mJy$^{-1}$ deg$^{-2}$) | S (mJy) | N(>S) (deg$^{-2}$) |
|---|---|---|---|
| 1.4 | $1283^{+282}_{-318}$ | 1.0 | $2092^{+291}_{-353}$ |
| 2.4 | $484^{+109}_{-130}$ | 2.0 | $808^{+134}_{-147}$ |
| 3.4 | $136^{+44}_{-58}$ | 3.0 | $324^{+71}_{-80}$ |
| 4.4 | $79^{+31}_{-42}$ | 4.0 | $188^{+51}_{-66}$ |
| 5.4 | $63^{+26}_{-38}$ | 5.0 | $108^{+35}_{-48}$ |
| 6.4 | $27^{+12}_{-24}$ | 6.0 | $45^{+19}_{-32}$ |

**Figure A8.** PKS0529−549 products.

**Table A8.** PKS0529−549 source catalogue.

| ID | IAU name | S/N | $S_{1.1mm}$ (measured) (mJy) | $S_{1.1mm}$ (deboosted) (mJy) | $P(<0)$ |
|---|---|---|---|---|---|
| 1 | MMJ053025.20−545422.02 | 9.72 | $6.4 \pm 0.7$ | $6.0^{+0.7}_{-0.6}$ | 0.000 |
| 2 | MMJ053039.52−550212.93 | 9.68 | $8.9 \pm 0.9$ | $8.3^{+0.9}_{-0.9}$ | 0.000 |
| 3 | MMJ053013.09−544852.52 | 9.32 | $6.2 \pm 0.7$ | $5.8^{+0.7}_{-0.7}$ | 0.000 |
| 4 | MMJ053050.23−545730.72 | 9.16 | $6.0 \pm 0.7$ | $5.6^{+0.7}_{-0.6}$ | 0.000 |
| 5 | MMJ053016.15−545513.12 | 8.66 | $5.6 \pm 0.6$ | $5.2^{+0.6}_{-0.7}$ | 0.000 |
| 6 | MMJ053048.78−545154.66 | 7.58 | $4.8 \pm 0.6$ | $4.5^{+0.6}_{-0.7}$ | 0.000 |
| 7 | MMJ053054.44−545334.29 | 7.58 | $4.8 \pm 0.6$ | $4.4^{+0.7}_{-0.6}$ | 0.000 |
| 8 | MMJ053003.86−545846.47 | 7.48 | $5.0 \pm 0.7$ | $4.6^{+0.7}_{-0.7}$ | 0.000 |
| 9 | MMJ052932.76−545233.82 | 6.82 | $5.6 \pm 0.8$ | $5.1^{+0.8}_{-0.9}$ | 0.000 |
| 10 | MMJ053041.54−544731.49 | 6.48 | $5.2 \pm 0.8$ | $4.6^{+0.8}_{-0.8}$ | 0.000 |
| 11 | MMJ053027.53−544600.34 | 6.15 | $5.6 \pm 0.9$ | $4.9^{+0.9}_{-0.9}$ | 0.000 |
| 12 | MMJ053011.19−550028.22 | 6.10 | $4.4 \pm 0.7$ | $4.0^{+0.7}_{-0.7}$ | 0.000 |
| 13 | MMJ053044.77−545160.00 | 5.37 | $3.4 \pm 0.6$ | $3.0^{+0.6}_{-0.7}$ | 0.000 |
| 14 | MMJ052954.18−545715.33 | 5.11 | $3.4 \pm 0.7$ | $2.9^{+0.7}_{-0.7}$ | 0.000 |
| 15 | MMJ053107.92−545433.47 | 4.95 | $3.5 \pm 0.7$ | $3.0^{+0.7}_{-0.7}$ | 0.000 |
| 16 | MMJ053000.62−545121.68 | 4.85 | $3.1 \pm 0.6$ | $2.7^{+0.6}_{-0.7}$ | 0.000 |
| 17 | MMJ053101.07−545516.20 | 4.68 | $3.1 \pm 0.7$ | $2.6^{+0.7}_{-0.7}$ | 0.000 |
| 18 | MMJ053105.52−545325.33 | 4.58 | $3.1 \pm 0.7$ | $2.6^{+0.7}_{-0.7}$ | 0.000 |
| 19 | MMJ053047.98−550021.82 | 4.58 | $3.5 \pm 0.8$ | $2.9^{+0.8}_{-0.8}$ | 0.000 |
| 20 | MMJ053100.58−544933.32 | 4.57 | $3.5 \pm 0.8$ | $2.9^{+0.8}_{-0.8}$ | 0.000 |
| 21 | MMJ052945.58−545257.57 | 4.53 | $3.1 \pm 0.7$ | $2.6^{+0.7}_{-0.7}$ | 0.000 |
| 22 | MMJ052942.44−545145.84 | 4.15 | $3.0 \pm 0.7$ | $2.4^{+0.8}_{-0.8}$ | 0.001 |
| 23 | MMJ052953.04−544839.74 | 3.97 | $3.1 \pm 0.8$ | $2.4^{+0.8}_{-0.8}$ | 0.002 |
| 24 | MMJ053010.98−545946.32 | 3.91 | $2.7 \pm 0.7$ | $2.1^{+0.7}_{-0.7}$ | 0.002 |
| 25 | MMJ052933.98−545349.99 | 3.88 | $3.0 \pm 0.8$ | $2.3^{+0.8}_{-0.8}$ | 0.003 |
| 26 | MMJ053029.48−545315.71 | 3.80 | $2.4 \pm 0.6$ | $1.9^{+0.6}_{-0.7}$ | 0.003 |
| 27 | MMJ052942.59−545702.96 | 3.79 | $2.7 \pm 0.7$ | $2.1^{+0.8}_{-0.8}$ | 0.004 |
| 28 | MMJ053006.35−545918.82 | 3.78 | $2.6 \pm 0.7$ | $2.0^{+0.7}_{-0.7}$ | 0.003 |
| 29 | MMJ053016.87−545206.19 | 3.77 | $2.4 \pm 0.6$ | $1.9^{+0.7}_{-0.7}$ | 0.003 |
| 30 | MMJ053038.68−545314.40 | 3.68 | $2.3 \pm 0.6$ | $1.8^{+0.7}_{-0.7}$ | 0.004 |
| 31 | MMJ053022.67−545955.43 | 3.64 | $2.4 \pm 0.7$ | $1.8^{+0.7}_{-0.7}$ | 0.005 |
| 32 | MMJ053107.78−545851.46 | 3.57 | $3.1 \pm 0.9$ | $2.2^{+1.0}_{-0.9}$ | 0.012 |
| 33 | MMJ052959.42−545900.48 | 3.57 | $2.5 \pm 0.7$ | $1.8^{+0.7}_{-0.7}$ | 0.007 |
| 34 | MMJ053029.47−544812.29 | 3.54 | $2.4 \pm 0.7$ | $1.8^{+0.7}_{-0.7}$ | 0.008 |
| 35 | MMJ053020.68−550148.39 | 3.50 | $2.9 \pm 0.8$ | $2.0^{+0.9}_{-0.9}$ | 0.013 |
| 36 | MMJ052949.11−545541.66 | 3.47 | $2.3 \pm 0.7$ | $1.7^{+0.7}_{-0.7}$ | 0.009 |
| 37 | MMJ053016.52−544653.03 | 3.45 | $2.8 \pm 0.8$ | $2.0^{+0.8}_{-0.9}$ | 0.013 |
| 38 | MMJ052929.76−545704.04 | 3.44 | $3.1 \pm 0.9$ | $2.1^{+1.0}_{-1.0}$ | 0.018 |
| 39 | MMJ053014.07−545626.40 | 3.39 | $2.1 \pm 0.6$ | $1.6^{+0.7}_{-0.7}$ | 0.010 |
| 40 | MMJ053011.48−545838.37 | 3.39 | $2.2 \pm 0.6$ | $1.6^{+0.7}_{-0.7}$ | 0.011 |
| 41 | MMJ052941.60−545547.58 | 3.36 | $2.4 \pm 0.7$ | $1.7^{+0.7}_{-0.8}$ | 0.013 |
| 42 | MMJ053009.52−545355.68 | 3.36 | $2.1 \pm 0.6$ | $1.6^{+0.7}_{-0.7}$ | 0.011 |
| 43 | MMJ053103.73−545032.94 | 3.33 | $2.5 \pm 0.7$ | $1.7^{+0.8}_{-0.8}$ | 0.016 |
| 44 | MMJ053008.53−544716.01 | 3.30 | $2.6 \pm 0.8$ | $1.7^{+0.8}_{-0.8}$ | 0.020 |
| 45 | MMJ052939.67−545545.21 | 3.21 | $2.3 \pm 0.7$ | $1.6^{+0.8}_{-0.8}$ | 0.021 |
| 46 | MMJ052959.77−544801.70 | 3.20 | $2.5 \pm 0.8$ | $1.7^{+0.8}_{-0.8}$ | 0.025 |
| 47 | MMJ053025.61−545104.18 | 3.19 | $2.0 \pm 0.6$ | $1.4^{+0.7}_{-0.7}$ | 0.018 |
| 48 | MMJ052958.83−544726.66 | 3.12 | $2.6 \pm 0.8$ | $1.7^{+0.9}_{-0.9}$ | 0.034 |
| 49 | MMJ053010.61−545851.71 | 3.12 | $2.0 \pm 0.7$ | $1.4^{+0.7}_{-0.7}$ | 0.023 |

**Table A8** – *continued*

| ID | IAU name | S/N | $S_{1.1mm}$ (measured) (mJy) | $S_{1.1mm}$ (deboosted) (mJy) | $P(<0)$ |
|---|---|---|---|---|---|
| 50 | MMJ053120.59−545509.25 | 3.09 | $2.8 \pm 0.9$ | $1.7^{+1.0}_{-1.0}$ | 0.043 |
| 51 | MMJ052955.45−544944.85 | 3.08 | $2.1 \pm 0.7$ | $1.4^{+0.7}_{-0.8}$ | 0.029 |
| 52 | MMJ053100.77−545152.79 | 3.06 | $2.1 \pm 0.7$ | $1.4^{+0.7}_{-0.7}$ | 0.029 |
| 53 | MMJ053016.05−545603.50 | 3.05 | $1.9 \pm 0.6$ | $1.4^{+0.7}_{-0.7}$ | 0.026 |
| 54 | MMJ053019.74−545016.71 | 3.05 | $1.9 \pm 0.6$ | $1.4^{+0.7}_{-0.7}$ | 0.027 |
| 55 | MMJ053054.57−545007.30 | 3.03 | $2.1 \pm 0.7$ | $1.4^{+0.7}_{-0.8}$ | 0.033 |

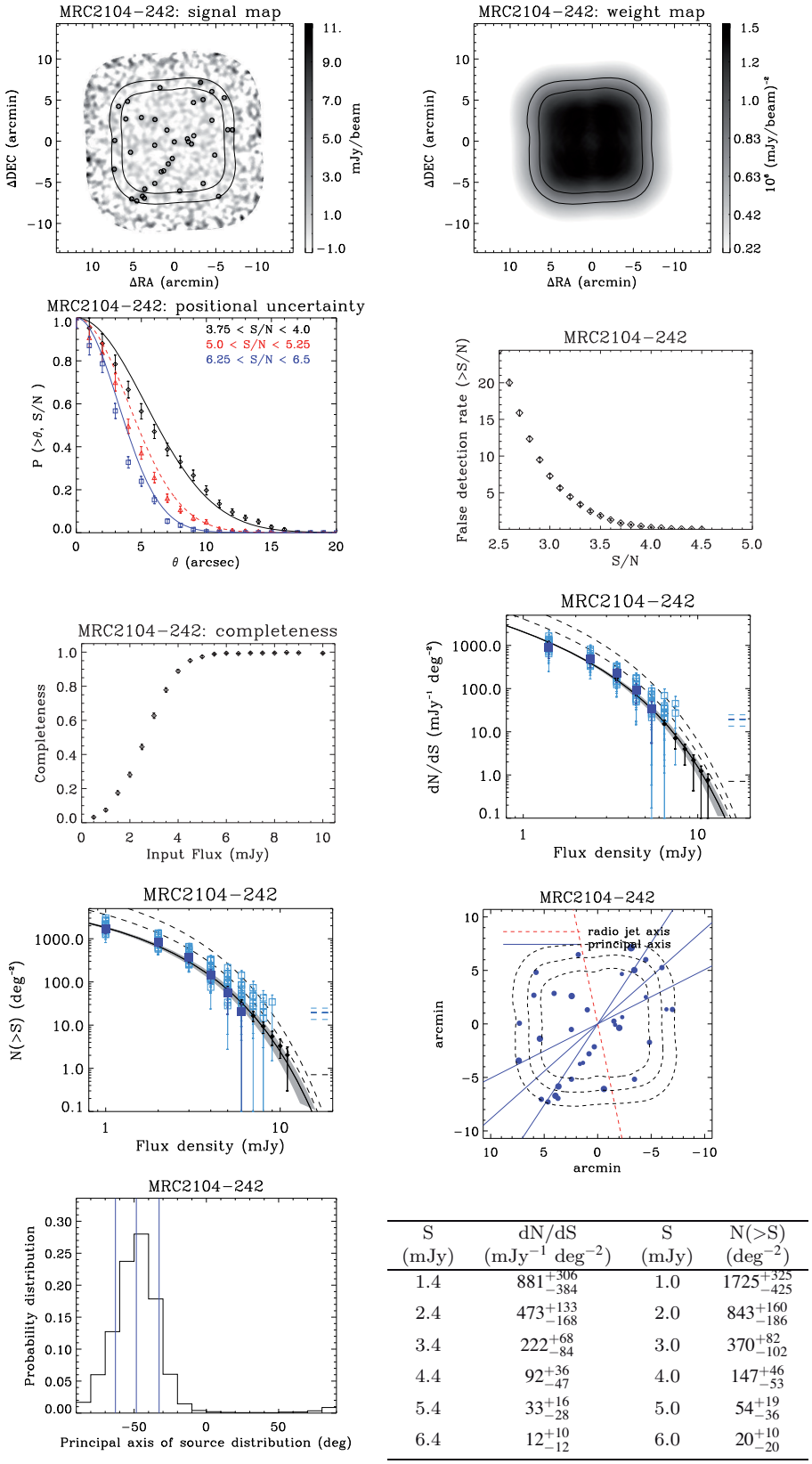


| S (mJy) | dN/dS (mJy$^{-1}$ deg$^{-2}$) | S (mJy) | N(>S) (deg$^{-2}$) |
|---|---|---|---|
| 1.4 | $881^{+306}_{-384}$ | 1.0 | $1725^{+325}_{-425}$ |
| 2.4 | $473^{+133}_{-168}$ | 2.0 | $843^{+160}_{-186}$ |
| 3.4 | $222^{+68}_{-84}$ | 3.0 | $370^{+82}_{-102}$ |
| 4.4 | $92^{+36}_{-47}$ | 4.0 | $147^{+46}_{-53}$ |
| 5.4 | $33^{+16}_{-28}$ | 5.0 | $54^{+19}_{-36}$ |
| 6.4 | $12^{+10}_{-12}$ | 6.0 | $20^{+10}_{-20}$ |

**Figure A9.** MRC2104−242 products.

**Table A9.** MRC2104−242 source catalogue.

| ID | IAU name | S/N | $S_{1.1mm}$ (measured) (mJy) | $S_{1.1mm}$ (deboosted) (mJy) | $P(<0)$ |
|---|---|---|---|---|---|
| 1 | MMJ210644.32−235801.57 | 6.90 | $7.8 \pm 1.1$ | $6.8^{+1.2}_{-1.1}$ | 0.000 |
| 2 | MMJ210642.99−240007.56 | 5.60 | $5.1 \pm 0.9$ | $4.4^{+0.9}_{-0.9}$ | 0.000 |
| 3 | MMJ210708.64−240232.83 | 5.52 | $4.7 \pm 0.8$ | $4.0^{+0.9}_{-0.9}$ | 0.000 |
| 4 | MMJ210714.07−241059.63 | 5.41 | $5.2 \pm 1.0$ | $4.4^{+1.0}_{-1.0}$ | 0.000 |
| 5 | MMJ210655.44−241113.81 | 5.33 | $5.3 \pm 1.0$ | $4.4^{+1.0}_{-1.0}$ | 0.000 |
| 6 | MMJ210649.15−240531.31 | 5.16 | $4.4 \pm 0.8$ | $3.7^{+0.8}_{-0.9}$ | 0.000 |
| 7 | MMJ210730.34−240835.08 | 5.13 | $6.0 \pm 1.2$ | $4.8^{+1.2}_{-1.2}$ | 0.000 |
| 8 | MMJ210715.32−241152.09 | 4.70 | $5.1 \pm 1.1$ | $4.0^{+1.1}_{-1.1}$ | 0.000 |
| 9 | MMJ210721.66−240631.96 | 4.64 | $4.2 \pm 0.9$ | $3.4^{+0.9}_{-1.0}$ | 0.000 |
| 10 | MMJ210701.54−240756.62 | 4.47 | $3.8 \pm 0.8$ | $3.0^{+0.9}_{-0.9}$ | 0.000 |
| 11 | MMJ210723.21−240020.04 | 4.39 | $4.3 \pm 1.0$ | $3.4^{+1.0}_{-1.0}$ | 0.001 |
| 12 | MMJ210724.12−240228.43 | 4.27 | $4.0 \pm 0.9$ | $3.1^{+1.0}_{-1.0}$ | 0.001 |
| 13 | MMJ210658.33−240515.96 | 4.25 | $3.7 \pm 0.9$ | $2.9^{+0.9}_{-0.9}$ | 0.001 |
| 14 | MMJ210714.29−241206.17 | 4.16 | $4.6 \pm 1.1$ | $3.4^{+1.2}_{-1.2}$ | 0.003 |
| 15 | MMJ210659.39−240717.35 | 4.03 | $3.5 \pm 0.9$ | $2.7^{+0.9}_{-0.9}$ | 0.002 |
| 16 | MMJ210715.83−240218.01 | 3.96 | $3.4 \pm 0.9$ | $2.6^{+0.9}_{-0.9}$ | 0.003 |
| 17 | MMJ210730.07−240505.45 | 3.88 | $4.5 \pm 1.2$ | $3.1^{+1.2}_{-1.3}$ | 0.009 |
| 18 | MMJ210651.35−240453.66 | 3.84 | $3.2 \pm 0.8$ | $2.4^{+0.9}_{-0.9}$ | 0.004 |
| 19 | MMJ210642.91−241019.45 | 3.81 | $3.6 \pm 0.9$ | $2.6^{+1.0}_{-1.0}$ | 0.006 |
| 20 | MMJ210721.08−241211.94 | 3.71 | $4.5 \pm 1.2$ | $3.0^{+1.3}_{-1.4}$ | 0.016 |
| 21 | MMJ210627.38−240348.10 | 3.64 | $4.3 \pm 1.2$ | $2.8^{+1.3}_{-1.3}$ | 0.018 |
| 22 | MMJ210636.77−240652.34 | 3.58 | $3.2 \pm 0.9$ | $2.2^{+1.0}_{-0.9}$ | 0.011 |
| 23 | MMJ210705.93−235840.63 | 3.57 | $3.8 \pm 1.1$ | $2.5^{+1.2}_{-1.1}$ | 0.016 |
| 24 | MMJ210708.73−241019.20 | 3.55 | $3.2 \pm 0.9$ | $2.2^{+1.0}_{-1.0}$ | 0.012 |
| 25 | MMJ210638.32−235908.55 | 3.55 | $3.7 \pm 1.0$ | $2.5^{+1.1}_{-1.2}$ | 0.017 |
| 26 | MMJ210708.78−240540.22 | 3.55 | $3.0 \pm 0.9$ | $2.2^{+0.9}_{-0.9}$ | 0.011 |
| 27 | MMJ210631.69−235953.32 | 3.49 | $4.0 \pm 1.1$ | $2.5^{+1.3}_{-1.2}$ | 0.025 |
| 28 | MMJ210702.23−240349.98 | 3.47 | $3.0 \pm 0.9$ | $2.1^{+0.9}_{-0.9}$ | 0.014 |
| 29 | MMJ210718.35−241226.49 | 3.47 | $4.2 \pm 1.2$ | $2.6^{+1.3}_{-1.4}$ | 0.030 |
| 30 | MMJ210629.84−240347.34 | 3.43 | $3.7 \pm 1.1$ | $2.3^{+1.2}_{-1.2}$ | 0.026 |
| 31 | MMJ210638.27−240238.28 | 3.33 | $3.0 \pm 0.9$ | $2.0^{+1.0}_{-0.9}$ | 0.023 |
| 32 | MMJ210705.26−240853.48 | 3.24 | $2.7 \pm 0.8$ | $1.8^{+0.9}_{-0.9}$ | 0.026 |
| 33 | MMJ210648.10−240029.03 | 3.20 | $2.8 \pm 0.9$ | $1.8^{+0.9}_{-1.0}$ | 0.030 |
| 34 | MMJ210704.01−240847.38 | 3.19 | $2.7 \pm 0.8$ | $1.8^{+0.9}_{-0.9}$ | 0.029 |
| 35 | MMJ210634.70−241153.39 | 3.17 | $3.8 \pm 1.2$ | $2.1^{+1.3}_{-1.4}$ | 0.058 |
| 36 | MMJ210728.00−240056.05 | 3.13 | $3.4 \pm 1.1$ | $2.0^{+1.1}_{-1.2}$ | 0.052 |
| 37 | MMJ210650.85−240514.29 | 3.05 | $2.6 \pm 0.8$ | $1.6^{+0.9}_{-1.0}$ | 0.041 |
| 38 | MMJ210647.94−240431.22 | 3.02 | $2.6 \pm 0.9$ | $1.6^{+0.9}_{-0.9}$ | 0.045 |

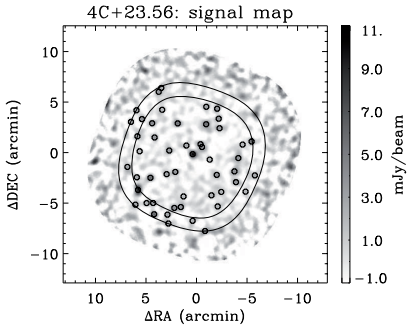


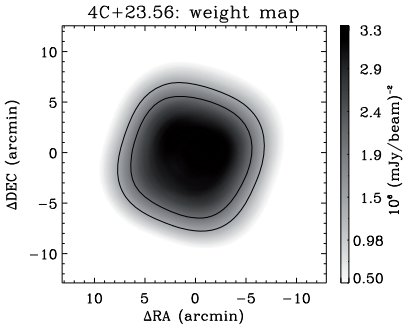


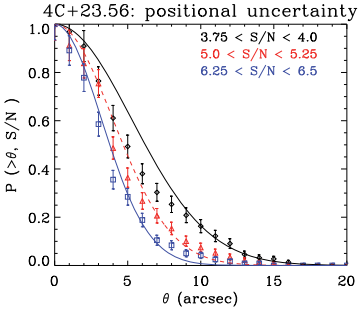


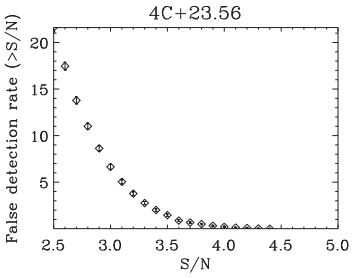


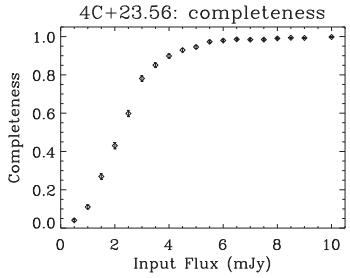


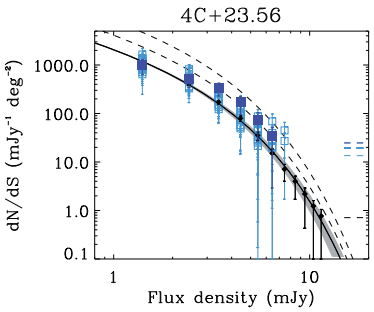


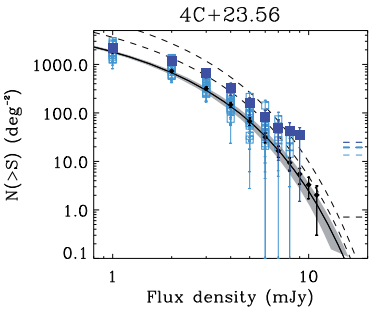


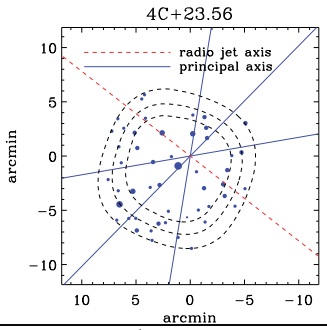


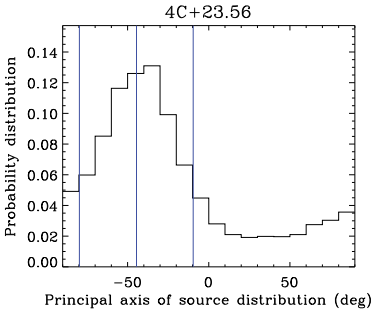


| S (mJy) | dN/dS (mJy$^{-1}$ deg$^{-2}$) | S (mJy) | N(>S) (deg$^{-2}$) |
|---|---|---|---|
| 1.4 | $1006^{+297}_{-370}$ | 1.0 | $2172^{+353}_{-413}$ |
| 2.4 | $504^{+131}_{-162}$ | 2.0 | $1165^{+182}_{-206}$ |
| 3.4 | $333^{+86}_{-103}$ | 3.0 | $660^{+121}_{-135}$ |
| 4.4 | $169^{+54}_{-74}$ | 4.0 | $327^{+82}_{-98}$ |
| 5.4 | $73^{+31}_{-46}$ | 5.0 | $157^{+46}_{-67}$ |
| 6.4 | $34^{+16}_{-32}$ | 6.0 | $84^{+29}_{-57}$ |
| 7.4 | $6^{+10}_{-6}$ | 7.0 | $49^{+22}_{-38}$ |
| 8.4 | $8^{+11}_{-8}$ | 8.0 | $42^{+20}_{-36}$ |
| 9.4 | $19^{+13}_{-19}$ | 9.0 | $34^{+15}_{-32}$ |

**Figure A10.** 4C+23.56 products.

**Table A10.** 4C+23.56 source catalogue.

| ID | IAU name | S/N | $S_{1.1mm}$ (measured) (mJy) | $S_{1.1mm}$ (deboosted) (mJy) | $P(<0)$ |
|---|---|---|---|---|---|
| 1 | MMJ210719.67+233050.70 | 18.37 | $10.3 \pm 0.6$ | $10.1^{+0.5}_{-0.6}$ | 0.000 |
| 2 | MMJ210743.23+232718.06 | 13.56 | $9.5 \pm 0.7$ | $9.2^{+0.7}_{-0.7}$ | 0.000 |
| 3 | MMJ210737.89+232830.12 | 10.24 | $6.2 \pm 0.6$ | $6.0^{+0.6}_{-0.6}$ | 0.000 |
| 4 | MMJ210713.83+233348.31 | 10.06 | $5.8 \pm 0.6$ | $5.5^{+0.6}_{-0.6}$ | 0.000 |
| 5 | MMJ210726.11+233353.38 | 9.84 | $5.5 \pm 0.6$ | $5.3^{+0.6}_{-0.6}$ | 0.000 |
| 6 | MMJ210654.21+233205.65 | 9.09 | $6.2 \pm 0.7$ | $5.9^{+0.7}_{-0.7}$ | 0.000 |
| 7 | MMJ210652.62+233447.40 | 8.72 | $7.4 \pm 0.9$ | $6.8^{+0.9}_{-0.8}$ | 0.000 |
| 8 | MMJ210716.26+233149.69 | 8.30 | $4.6 \pm 0.6$ | $4.3^{+0.6}_{-0.5}$ | 0.000 |
| 9 | MMJ210736.28+232453.70 | 8.29 | $6.6 \pm 0.8$ | $6.2^{+0.8}_{-0.8}$ | 0.000 |
| 10 | MMJ210715.63+233133.16 | 7.74 | $4.3 \pm 0.6$ | $4.0^{+0.5}_{-0.6}$ | 0.000 |
| 11 | MMJ210709.27+232847.49 | 7.46 | $4.2 \pm 0.6$ | $4.0^{+0.5}_{-0.6}$ | 0.000 |
| 12 | MMJ210727.15+232905.09 | 7.12 | $4.1 \pm 0.6$ | $3.8^{+0.6}_{-0.6}$ | 0.000 |
| 13 | MMJ210737.16+233354.07 | 7.10 | $4.4 \pm 0.6$ | $4.1^{+0.6}_{-0.7}$ | 0.000 |
| 14 | MMJ210701.62+232908.57 | 7.00 | $4.2 \pm 0.6$ | $3.9^{+0.6}_{-0.6}$ | 0.000 |
| 15 | MMJ210729.77+233112.12 | 6.99 | $3.9 \pm 0.6$ | $3.6^{+0.6}_{-0.6}$ | 0.000 |
| 16 | MMJ210708.41+233421.22 | 6.90 | $4.2 \pm 0.6$ | $3.9^{+0.6}_{-0.6}$ | 0.000 |
| 17 | MMJ210659.94+233027.27 | 6.87 | $4.1 \pm 0.6$ | $3.8^{+0.6}_{-0.6}$ | 0.000 |
| 18 | MMJ210736.10+233229.61 | 6.72 | $4.0 \pm 0.6$ | $3.6^{+0.6}_{-0.6}$ | 0.000 |
| 19 | MMJ210708.05+233324.73 | 6.67 | $3.8 \pm 0.6$ | $3.5^{+0.6}_{-0.6}$ | 0.000 |
| 20 | MMJ210700.97+232804.31 | 6.31 | $4.1 \pm 0.6$ | $3.6^{+0.7}_{-0.6}$ | 0.000 |
| 21 | MMJ210727.57+232531.32 | 6.27 | $4.2 \pm 0.7$ | $3.8^{+0.7}_{-0.7}$ | 0.000 |
| 22 | MMJ210709.09+233520.53 | 6.14 | $4.1 \pm 0.7$ | $3.6^{+0.7}_{-0.7}$ | 0.000 |
| 23 | MMJ210724.78+232536.48 | 5.87 | $3.8 \pm 0.6$ | $3.4^{+0.6}_{-0.7}$ | 0.000 |
| 24 | MMJ210741.56+233418.80 | 5.83 | $4.2 \pm 0.7$ | $3.6^{+0.8}_{-0.7}$ | 0.000 |
| 25 | MMJ210714.31+232314.34 | 5.79 | $4.9 \pm 0.8$ | $4.3^{+0.9}_{-0.9}$ | 0.000 |
| 26 | MMJ210730.90+232851.78 | 5.70 | $3.3 \pm 0.6$ | $2.9^{+0.6}_{-0.6}$ | 0.000 |
| 27 | MMJ210722.38+233141.75 | 5.29 | $3.0 \pm 0.6$ | $2.6^{+0.5}_{-0.6}$ | 0.000 |
| 28 | MMJ210743.51+233236.57 | 4.91 | $3.4 \pm 0.7$ | $2.9^{+0.7}_{-0.7}$ | 0.000 |
| 29 | MMJ210713.78+233531.96 | 4.90 | $3.2 \pm 0.6$ | $2.7^{+0.7}_{-0.7}$ | 0.000 |
| 30 | MMJ210734.33+233700.69 | 4.70 | $3.7 \pm 0.8$ | $3.1^{+0.8}_{-0.8}$ | 0.000 |
| 31 | MMJ210736.73+232600.68 | 4.67 | $3.3 \pm 0.7$ | $2.8^{+0.7}_{-0.7}$ | 0.000 |
| 32 | MMJ210730.55+232451.23 | 4.59 | $3.4 \pm 0.7$ | $2.8^{+0.8}_{-0.8}$ | 0.000 |
| 33 | MMJ210743.76+232833.16 | 4.53 | $3.0 \pm 0.7$ | $2.5^{+0.7}_{-0.7}$ | 0.000 |
| 34 | MMJ210747.83+232934.76 | 4.09 | $3.0 \pm 0.7$ | $2.4^{+0.8}_{-0.8}$ | 0.001 |
| 35 | MMJ210711.55+232646.23 | 4.05 | $2.4 \pm 0.6$ | $1.9^{+0.6}_{-0.6}$ | 0.001 |
| 36 | MMJ210712.30+233018.17 | 3.93 | $2.2 \pm 0.6$ | $1.7^{+0.6}_{-0.6}$ | 0.001 |
| 37 | MMJ210707.31+232706.33 | 3.86 | $2.3 \pm 0.6$ | $1.9^{+0.6}_{-0.6}$ | 0.002 |
| 38 | MMJ210652.82+232844.48 | 3.80 | $3.0 \pm 0.8$ | $2.2^{+0.8}_{-0.8}$ | 0.005 |
| 39 | MMJ210719.69+232414.75 | 3.73 | $2.7 \pm 0.7$ | $2.1^{+0.8}_{-0.8}$ | 0.005 |
| 40 | MMJ210743.94+233511.33 | 3.69 | $3.1 \pm 0.9$ | $2.3^{+0.9}_{-0.9}$ | 0.008 |
| 41 | MMJ210744.36+232550.55 | 3.65 | $3.0 \pm 0.8$ | $2.2^{+0.9}_{-0.9}$ | 0.008 |
| 42 | MMJ210708.85+232540.29 | 3.63 | $2.4 \pm 0.7$ | $1.8^{+0.7}_{-0.7}$ | 0.005 |
| 43 | MMJ210658.11+233147.42 | 3.52 | $2.2 \pm 0.6$ | $1.6^{+0.7}_{-0.7}$ | 0.007 |
| 44 | MMJ210739.53+232600.04 | 3.47 | $2.5 \pm 0.7$ | $1.8^{+0.8}_{-0.8}$ | 0.011 |
| 45 | MMJ210746.31+233402.29 | 3.41 | $2.9 \pm 0.8$ | $1.9^{+0.9}_{-0.9}$ | 0.017 |
| 46 | MMJ210730.14+232358.78 | 3.39 | $2.9 \pm 0.9$ | $2.0^{+0.9}_{-0.9}$ | 0.019 |
| 47 | MMJ210732.83+233514.25 | 3.36 | $2.1 \pm 0.6$ | $1.6^{+0.7}_{-0.7}$ | 0.012 |
| 48 | MMJ210723.60+232639.57 | 3.28 | $2.0 \pm 0.6$ | $1.4^{+0.6}_{-0.6}$ | 0.013 |
| 49 | MMJ210742.55+233107.74 | 3.11 | $2.0 \pm 0.6$ | $1.4^{+0.7}_{-0.7}$ | 0.024 |
| 50 | MMJ210656.83+232707.92 | 3.08 | $2.3 \pm 0.8$ | $1.5^{+0.8}_{-0.8}$ | 0.034 |
| 51 | MMJ210733.21+233724.08 | 3.07 | $2.6 \pm 0.8$ | $1.6^{+0.9}_{-0.9}$ | 0.041 |

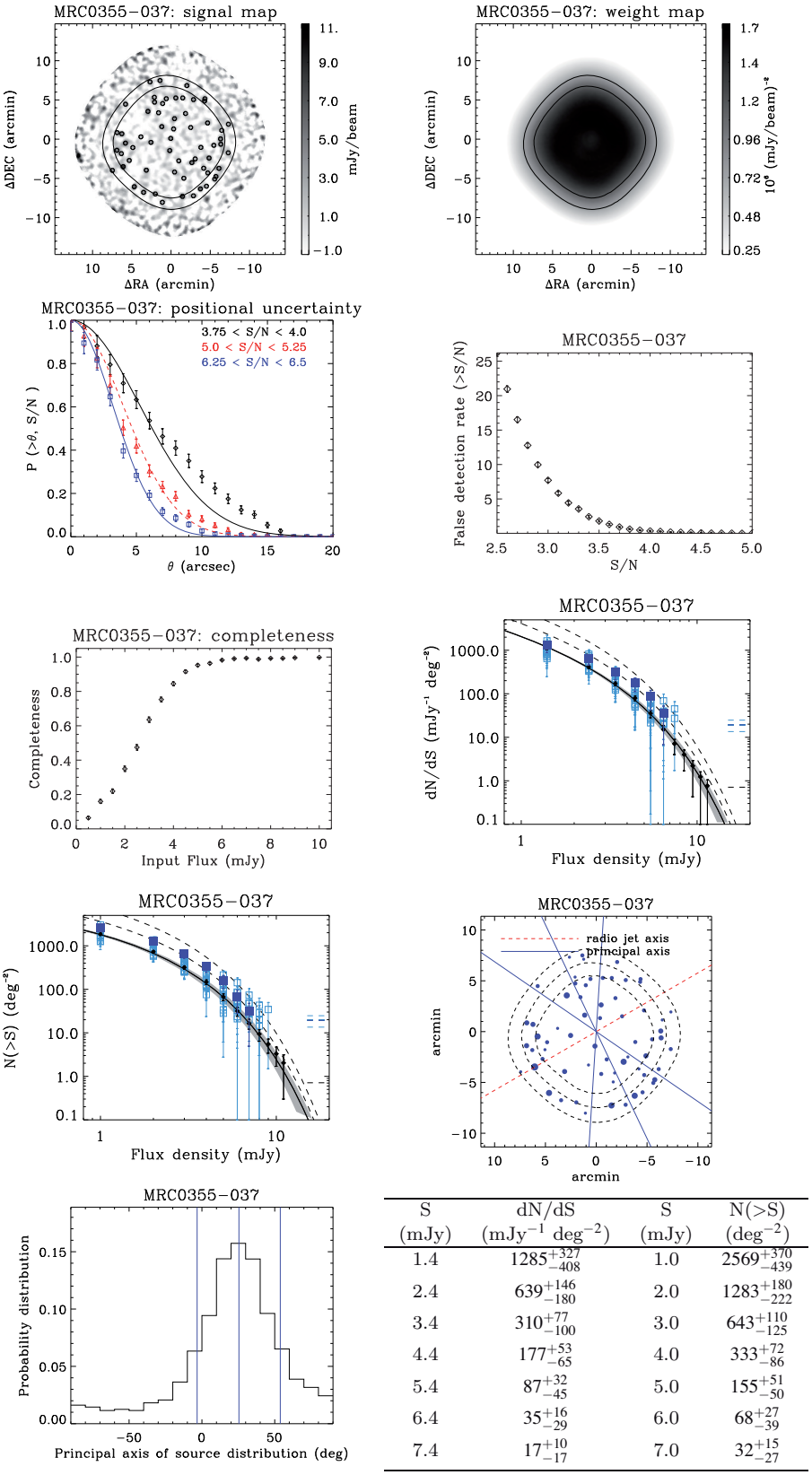


| S (mJy) | dN/dS (mJy$^{-1}$ deg$^{-2}$) | S (mJy) | N(>S) (deg$^{-2}$) |
|---|---|---|---|
| 1.4 | $1285^{+327}_{-408}$ | 1.0 | $2569^{+370}_{-439}$ |
| 2.4 | $639^{+146}_{-180}$ | 2.0 | $1283^{+180}_{-222}$ |
| 3.4 | $310^{+77}_{-100}$ | 3.0 | $643^{+110}_{-125}$ |
| 4.4 | $177^{+53}_{-65}$ | 4.0 | $333^{+72}_{-86}$ |
| 5.4 | $87^{+32}_{-45}$ | 5.0 | $155^{+51}_{-50}$ |
| 6.4 | $35^{+16}_{-29}$ | 6.0 | $68^{+27}_{-39}$ |
| 7.4 | $17^{+10}_{-17}$ | 7.0 | $32^{+15}_{-27}$ |

**Figure A11.** MRC0355−037 products.

**Table A11.** MRC0355−037 source catalogue.

| ID | IAU name | S/N | $S_{1.1mm}$ (measured) (mJy) | $S_{1.1mm}$ (deboosted) (mJy) | $P(<0)$ |
|---|---|---|---|---|---|
| 1 | MMJ035812.35−033738.25 | 9.75 | $9.0 \pm 0.9$ | $8.5^{+0.8}_{-1.0}$ | 0.000 |
| 2 | MMJ035742.05−034125.45 | 7.50 | $7.1 \pm 0.9$ | $6.5^{+0.9}_{-1.0}$ | 0.000 |
| 3 | MMJ035732.89−034028.04 | 7.42 | $7.5 \pm 1.0$ | $6.6^{+1.1}_{-1.0}$ | 0.000 |
| 4 | MMJ035759.69−033035.79 | 7.28 | $5.9 \pm 0.8$ | $5.4^{+0.8}_{-0.8}$ | 0.000 |
| 5 | MMJ035811.19−033438.14 | 7.16 | $5.9 \pm 0.8$ | $5.4^{+0.8}_{-0.9}$ | 0.000 |
| 6 | MMJ035737.25−033707.60 | 6.95 | $5.5 \pm 0.8$ | $5.0^{+0.8}_{-0.8}$ | 0.000 |
| 7 | MMJ035806.68−034011.54 | 6.78 | $7.0 \pm 1.0$ | $6.1^{+1.1}_{-1.0}$ | 0.000 |
| 8 | MMJ035758.16−033432.31 | 6.37 | $5.0 \pm 0.8$ | $4.5^{+0.8}_{-0.8}$ | 0.000 |
| 9 | MMJ035746.13−033131.77 | 6.19 | $4.8 \pm 0.8$ | $4.2^{+0.8}_{-0.7}$ | 0.000 |
| 10 | MMJ035748.05−033402.40 | 6.11 | $5.0 \pm 0.8$ | $4.4^{+0.9}_{-0.8}$ | 0.000 |
| 11 | MMJ035728.47−033632.33 | 6.06 | $5.0 \pm 0.8$ | $4.5^{+0.8}_{-0.9}$ | 0.000 |
| 12 | MMJ035748.57−033535.03 | 6.05 | $4.9 \pm 0.8$ | $4.2^{+0.9}_{-0.8}$ | 0.000 |
| 13 | MMJ035752.63−033232.28 | 5.99 | $4.7 \pm 0.8$ | $4.2^{+0.8}_{-0.8}$ | 0.000 |
| 14 | MMJ035815.53−033532.56 | 5.95 | $5.4 \pm 0.9$ | $4.7^{+0.9}_{-0.9}$ | 0.000 |
| 15 | MMJ035722.62−033405.92 | 5.74 | $5.1 \pm 0.9$ | $4.4^{+0.9}_{-0.9}$ | 0.000 |
| 16 | MMJ035800.53−033805.15 | 5.61 | $4.6 \pm 0.8$ | $3.9^{+0.8}_{-0.8}$ | 0.000 |
| 17 | MMJ035813.02−033326.88 | 5.54 | $4.8 \pm 0.9$ | $4.1^{+0.9}_{-0.9}$ | 0.000 |
| 18 | MMJ035815.45−033317.71 | 5.24 | $4.8 \pm 0.9$ | $4.0^{+1.0}_{-0.9}$ | 0.000 |
| 19 | MMJ035722.47−033446.62 | 5.11 | $4.6 \pm 0.9$ | $3.8^{+0.9}_{-0.9}$ | 0.000 |
| 20 | MMJ035724.97−033853.50 | 5.09 | $5.3 \pm 1.0$ | $4.2^{+1.2}_{-1.0}$ | 0.000 |
| 21 | MMJ035801.91−034054.72 | 4.80 | $4.8 \pm 1.0$ | $3.8^{+1.1}_{-1.0}$ | 0.000 |
| 22 | MMJ035746.09−033819.50 | 4.69 | $3.7 \pm 0.8$ | $3.1^{+0.8}_{-0.8}$ | 0.000 |
| 23 | MMJ035723.43−033750.92 | 4.63 | $4.6 \pm 1.0$ | $3.7^{+1.0}_{-1.1}$ | 0.000 |
| 24 | MMJ035739.81−032718.60 | 4.53 | $4.6 \pm 1.0$ | $3.6^{+1.1}_{-1.1}$ | 0.001 |
| 25 | MMJ035736.43−032905.33 | 4.49 | $4.0 \pm 0.9$ | $3.2^{+0.9}_{-0.9}$ | 0.000 |
| 26 | MMJ035813.28−033558.50 | 4.37 | $3.8 \pm 0.9$ | $3.0^{+0.9}_{-0.9}$ | 0.001 |
| 27 | MMJ035729.23−033204.29 | 4.35 | $3.6 \pm 0.8$ | $2.9^{+0.8}_{-0.9}$ | 0.001 |
| 28 | MMJ035740.49−033051.77 | 4.18 | $3.3 \pm 0.8$ | $2.6^{+0.8}_{-0.8}$ | 0.001 |
| 29 | MMJ035753.53−032639.47 | 4.12 | $4.4 \pm 1.1$ | $3.2^{+1.1}_{-1.1}$ | 0.003 |
| 30 | MMJ035809.24−033650.95 | 4.10 | $3.4 \pm 0.8$ | $2.6^{+0.9}_{-0.9}$ | 0.001 |
| 31 | MMJ035729.14−033825.91 | 4.03 | $3.7 \pm 0.9$ | $2.8^{+0.9}_{-1.0}$ | 0.002 |
| 32 | MMJ035745.47−032852.69 | 3.96 | $3.3 \pm 0.8$ | $2.5^{+0.9}_{-0.9}$ | 0.002 |
| 33 | MMJ035756.31−032925.13 | 3.96 | $3.3 \pm 0.8$ | $2.5^{+0.9}_{-0.9}$ | 0.002 |
| 34 | MMJ035746.57−033249.88 | 3.78 | $3.0 \pm 0.8$ | $2.2^{+0.8}_{-0.8}$ | 0.004 |
| 35 | MMJ035743.94−033653.65 | 3.74 | $3.0 \pm 0.8$ | $2.2^{+0.8}_{-0.9}$ | 0.004 |
| 36 | MMJ035732.66−033510.86 | 3.68 | $2.9 \pm 0.8$ | $2.1^{+0.8}_{-0.8}$ | 0.005 |
| 37 | MMJ035736.46−034121.33 | 3.65 | $3.7 \pm 1.0$ | $2.5^{+1.1}_{-1.2}$ | 0.010 |
| 38 | MMJ035729.79−034007.86 | 3.63 | $3.8 \pm 1.0$ | $2.5^{+1.1}_{-1.2}$ | 0.011 |
| 39 | MMJ035811.14−032940.64 | 3.60 | $3.8 \pm 1.1$ | $2.5^{+1.1}_{-1.2}$ | 0.012 |
| 40 | MMJ035752.18−032935.75 | 3.59 | $2.9 \pm 0.8$ | $2.1^{+0.9}_{-0.9}$ | 0.007 |
| 41 | MMJ035725.56−033912.44 | 3.47 | $3.7 \pm 1.1$ | $2.4^{+1.1}_{-1.3}$ | 0.017 |
| 42 | MMJ035741.93−032852.88 | 3.46 | $2.9 \pm 0.8$ | $2.0^{+0.9}_{-1.0}$ | 0.011 |
| 43 | MMJ035718.68−033552.60 | 3.44 | $3.5 \pm 1.0$ | $2.2^{+1.1}_{-1.1}$ | 0.017 |
| 44 | MMJ035730.59−032859.53 | 3.42 | $3.5 \pm 1.0$ | $2.2^{+1.1}_{-1.2}$ | 0.018 |
| 45 | MMJ035807.43−033512.16 | 3.41 | $2.7 \pm 0.8$ | $1.9^{+0.8}_{-0.9}$ | 0.012 |
| 46 | MMJ035730.75−032915.97 | 3.40 | $3.3 \pm 1.0$ | $2.1^{+1.1}_{-1.1}$ | 0.018 |
| 47 | MMJ035750.33−032858.57 | 3.33 | $2.7 \pm 0.8$ | $1.8^{+0.9}_{-0.9}$ | 0.015 |
| 48 | MMJ035755.93−034107.05 | 3.30 | $3.1 \pm 0.9$ | $2.0^{+1.0}_{-1.1}$ | 0.021 |
| 49 | MMJ035754.28−033046.17 | 3.29 | $2.6 \pm 0.8$ | $1.7^{+0.8}_{-0.9}$ | 0.016 |

**Table A11** – *continued*

| ID | IAU name | S/N | $S_{1.1mm}$ (measured) (mJy) | $S_{1.1mm}$ (deboosted) (mJy) | $P(<0)$ |
|---|---|---|---|---|---|
| 50 | MMJ035726.03−033454.92 | 3.27 | $2.7 \pm 0.8$ | $1.8^{+0.8}_{-1.0}$ | 0.018 |
| 51 | MMJ035737.86−033239.11 | 3.26 | $2.5 \pm 0.8$ | $1.7^{+0.8}_{-0.9}$ | 0.017 |
| 52 | MMJ035756.41−032847.67 | 3.20 | $2.7 \pm 0.9$ | $1.7^{+0.9}_{-1.0}$ | 0.023 |
| 53 | MMJ035731.22−033750.10 | 3.19 | $2.7 \pm 0.8$ | $1.7^{+0.9}_{-0.9}$ | 0.023 |
| 54 | MMJ035803.29−033350.31 | 3.18 | $2.5 \pm 0.8$ | $1.6^{+0.8}_{-0.9}$ | 0.021 |
| 55 | MMJ035722.02−033300.66 | 3.17 | $2.9 \pm 0.9$ | $1.8^{+0.9}_{-1.1}$ | 0.028 |
| 56 | MMJ035752.33−034210.83 | 3.17 | $3.3 \pm 1.0$ | $1.9^{+1.1}_{-1.2}$ | 0.033 |
| 57 | MMJ035758.64−032650.13 | 3.17 | $3.5 \pm 1.1$ | $2.0^{+1.1}_{-1.3}$ | 0.037 |
| 58 | MMJ035718.62−033213.59 | 3.15 | $3.4 \pm 1.1$ | $1.9^{+1.1}_{-1.3}$ | 0.037 |
| 59 | MMJ035735.58−033639.07 | 3.14 | $2.5 \pm 0.8$ | $1.6^{+0.8}_{-0.9}$ | 0.024 |
| 60 | MMJ035817.86−033806.72 | 3.06 | $3.5 \pm 1.1$ | $1.8^{+1.1}_{-1.4}$ | 0.049 |
| 61 | MMJ035741.36−033906.62 | 3.06 | $2.5 \pm 0.8$ | $1.5^{+0.9}_{-0.9}$ | 0.029 |

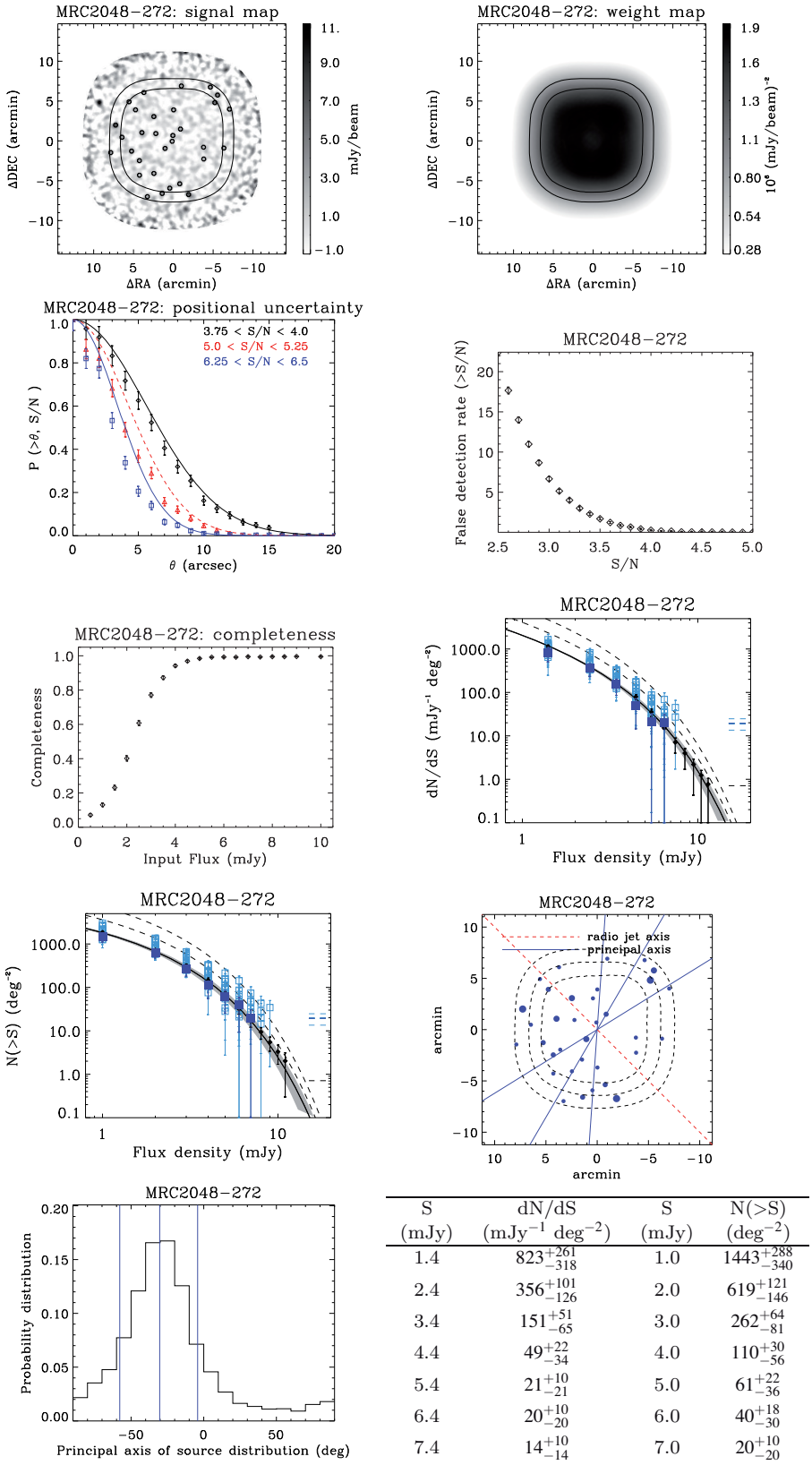


| S (mJy) | dN/dS (mJy$^{-1}$ deg$^{-2}$) | S (mJy) | N(>S) (deg$^{-2}$) |
|---|---|---|---|
| 1.4 | $823^{+261}_{-318}$ | 1.0 | $1443^{+288}_{-340}$ |
| 2.4 | $356^{+101}_{-126}$ | 2.0 | $619^{+121}_{-146}$ |
| 3.4 | $151^{+51}_{-65}$ | 3.0 | $262^{+64}_{-81}$ |
| 4.4 | $49^{+22}_{-34}$ | 4.0 | $110^{+30}_{-56}$ |
| 5.4 | $21^{+10}_{-21}$ | 5.0 | $61^{+22}_{-36}$ |
| 6.4 | $20^{+10}_{-20}$ | 6.0 | $40^{+18}_{-30}$ |
| 7.4 | $14^{+10}_{-14}$ | 7.0 | $20^{+10}_{-20}$ |

**Figure A12.** MRC2048−272 products.

**Table A12.** MRC2048−272 source catalogue.

| ID | IAU name | S/N | $S_{1.1mm}$ (measured) (mJy) | $S_{1.1mm}$ (deboosted) (mJy) | $P(<0)$ |
|---|---|---|---|---|---|
| 1 | MMJ205136.12−270103.24 | 8.06 | $7.9 \pm 1.0$ | $7.2^{+1.0}_{-1.0}$ | 0.000 |
| 2 | MMJ205054.99−270947.22 | 8.00 | $7.5 \pm 0.9$ | $6.8^{+1.1}_{-0.8}$ | 0.000 |
| 3 | MMJ205040.21−265814.51 | 7.55 | $6.6 \pm 0.9$ | $5.9^{+0.9}_{-0.8}$ | 0.000 |
| 4 | MMJ205038.67−265717.40 | 5.83 | $5.7 \pm 1.0$ | $5.0^{+0.9}_{-1.1}$ | 0.000 |
| 5 | MMJ205121.30−270200.05 | 5.73 | $4.3 \pm 0.8$ | $3.8^{+0.8}_{-0.7}$ | 0.000 |
| 6 | MMJ205108.25−270359.00 | 5.40 | $4.1 \pm 0.8$ | $3.6^{+0.8}_{-0.8}$ | 0.000 |
| 7 | MMJ205114.57−265959.45 | 5.39 | $4.0 \pm 0.7$ | $3.5^{+0.7}_{-0.8}$ | 0.000 |
| 8 | MMJ205122.74−270531.46 | 5.19 | $4.0 \pm 0.8$ | $3.4^{+0.8}_{-0.8}$ | 0.000 |
| 9 | MMJ205127.14−270419.70 | 4.90 | $3.8 \pm 0.8$ | $3.2^{+0.8}_{-0.8}$ | 0.000 |
| 10 | MMJ205059.98−270825.79 | 4.59 | $3.7 \pm 0.8$ | $3.0^{+0.8}_{-0.8}$ | 0.000 |
| 11 | MMJ205124.88−265908.33 | 4.49 | $3.6 \pm 0.8$ | $2.9^{+0.8}_{-0.8}$ | 0.000 |
| 12 | MMJ205109.87−270938.77 | 4.47 | $4.1 \pm 0.9$ | $3.2^{+1.0}_{-0.9}$ | 0.001 |
| 13 | MMJ205059.57−270133.54 | 4.29 | $3.2 \pm 0.8$ | $2.6^{+0.8}_{-0.8}$ | 0.001 |
| 14 | MMJ205138.91−270430.68 | 4.02 | $4.3 \pm 1.1$ | $3.1^{+1.1}_{-1.1}$ | 0.004 |
| 15 | MMJ205103.85−270221.81 | 4.00 | $3.1 \pm 0.8$ | $2.4^{+0.8}_{-0.8}$ | 0.002 |
| 16 | MMJ205042.73−265617.39 | 3.97 | $4.1 \pm 1.0$ | $2.9^{+1.1}_{-1.1}$ | 0.004 |
| 17 | MMJ205132.52−270235.06 | 3.95 | $3.5 \pm 0.9$ | $2.6^{+0.9}_{-0.9}$ | 0.003 |
| 18 | MMJ205105.60−270858.66 | 3.93 | $3.3 \pm 0.8$ | $2.5^{+0.8}_{-0.9}$ | 0.003 |
| 19 | MMJ205046.43−270518.70 | 3.76 | $2.9 \pm 0.8$ | $2.2^{+0.8}_{-0.8}$ | 0.004 |
| 20 | MMJ205114.57−270707.53 | 3.74 | $2.8 \pm 0.8$ | $2.2^{+0.8}_{-0.8}$ | 0.005 |
| 21 | MMJ205046.54−270350.35 | 3.53 | $2.7 \pm 0.8$ | $2.0^{+0.8}_{-0.8}$ | 0.009 |
| 22 | MMJ205118.25−271002.11 | 3.50 | $3.6 \pm 1.0$ | $2.4^{+1.1}_{-1.1}$ | 0.018 |
| 23 | MMJ205103.45−265908.87 | 3.46 | $2.6 \pm 0.8$ | $1.8^{+0.8}_{-0.8}$ | 0.011 |
| 24 | MMJ205031.96−265903.25 | 3.35 | $3.5 \pm 1.1$ | $2.3^{+1.1}_{-1.2}$ | 0.029 |
| 25 | MMJ205059.07−265608.95 | 3.34 | $3.1 \pm 0.9$ | $2.1^{+1.0}_{-1.0}$ | 0.023 |
| 26 | MMJ205128.52−265807.86 | 3.27 | $2.9 \pm 0.9$ | $1.9^{+0.9}_{-1.0}$ | 0.025 |
| 27 | MMJ205113.45−270207.33 | 3.19 | $2.4 \pm 0.8$ | $1.6^{+0.8}_{-0.8}$ | 0.023 |
| 28 | MMJ205120.18−265658.57 | 3.10 | $2.7 \pm 0.9$ | $1.7^{+0.9}_{-1.0}$ | 0.038 |
| 29 | MMJ205035.07−270356.50 | 3.05 | $2.8 \pm 0.9$ | $1.7^{+1.0}_{-1.0}$ | 0.045 |
| 30 | MMJ205122.72−270720.74 | 3.04 | $2.4 \pm 0.8$ | $1.5^{+0.8}_{-0.9}$ | 0.038 |
| 31 | MMJ205104.24−270305.45 | 3.03 | $2.3 \pm 0.8$ | $1.5^{+0.8}_{-0.8}$ | 0.036 |

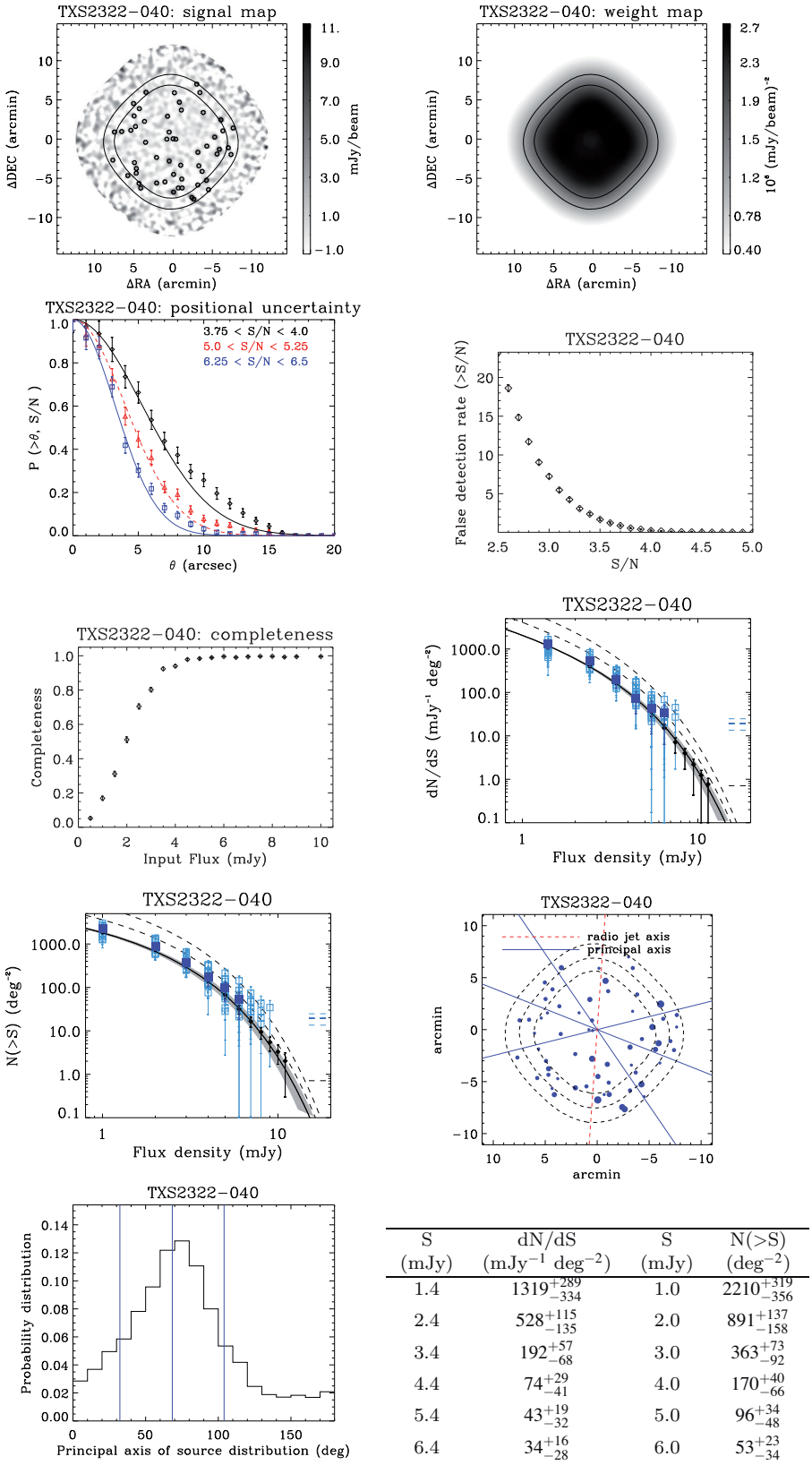


| S (mJy) | dN/dS (mJy$^{-1}$ deg$^{-2}$) | S (mJy) | N(>S) (deg$^{-2}$) |
|---|---|---|---|
| 1.4 | $1319^{+289}_{-334}$ | 1.0 | $2210^{+319}_{-356}$ |
| 2.4 | $528^{+115}_{-135}$ | 2.0 | $891^{+137}_{-158}$ |
| 3.4 | $192^{+57}_{-68}$ | 3.0 | $363^{+73}_{-92}$ |
| 4.4 | $74^{+29}_{-41}$ | 4.0 | $170^{+40}_{-66}$ |
| 5.4 | $43^{+19}_{-32}$ | 5.0 | $96^{+34}_{-48}$ |
| 6.4 | $34^{+16}_{-28}$ | 6.0 | $53^{+23}_{-34}$ |

**Figure A13.** TXS2322−040 products.

**Table A13.** TXS2322−040 source catalogue.

| ID | IAU name | S/N | $S_{1.1mm}$ (measured) (mJy) | $S_{1.1mm}$ (deboosted) (mJy) | $P(<0)$ |
|---|---|---|---|---|---|
| 1 | MMJ232445.77−034219.54 | 10.00 | $7.6 \pm 0.8$ | $7.2^{+0.7}_{-0.8}$ | 0.000 |
| 2 | MMJ232510.01−035132.31 | 9.81 | $6.8 \pm 0.7$ | $6.4^{+0.7}_{-0.7}$ | 0.000 |
| 3 | MMJ232500.57−035213.99 | 8.10 | $6.6 \pm 0.8$ | $6.0^{+0.8}_{-0.8}$ | 0.000 |
| 4 | MMJ232453.16−035002.48 | 8.01 | $6.1 \pm 0.8$ | $5.6^{+0.8}_{-0.8}$ | 0.000 |
| 5 | MMJ232446.55−034605.21 | 7.87 | $5.3 \pm 0.7$ | $4.9^{+0.7}_{-0.7}$ | 0.000 |
| 6 | MMJ232459.63−035226.05 | 7.79 | $6.6 \pm 0.8$ | $6.0^{+0.9}_{-0.9}$ | 0.000 |
| 7 | MMJ232512.19−034734.85 | 7.77 | $4.9 \pm 0.6$ | $4.5^{+0.6}_{-0.6}$ | 0.000 |
| 8 | MMJ232507.00−034005.26 | 7.45 | $4.7 \pm 0.6$ | $4.4^{+0.6}_{-0.7}$ | 0.000 |
| 9 | MMJ232448.95−034431.59 | 6.77 | $4.4 \pm 0.6$ | $4.1^{+0.6}_{-0.7}$ | 0.000 |
| 10 | MMJ232518.64−035022.82 | 6.24 | $4.1 \pm 0.7$ | $3.7^{+0.7}_{-0.7}$ | 0.000 |
| 11 | MMJ232513.06−034152.58 | 5.65 | $3.5 \pm 0.6$ | $3.1^{+0.6}_{-0.6}$ | 0.000 |
| 12 | MMJ232447.74−034641.04 | 5.52 | $3.7 \pm 0.7$ | $3.3^{+0.7}_{-0.7}$ | 0.000 |
| 13 | MMJ232457.56−034627.91 | 5.45 | $3.4 \pm 0.6$ | $3.0^{+0.6}_{-0.6}$ | 0.000 |
| 14 | MMJ232528.98−034832.48 | 5.42 | $3.6 \pm 0.7$ | $3.2^{+0.7}_{-0.7}$ | 0.000 |
| 15 | MMJ232526.76−035101.75 | 5.24 | $4.1 \pm 0.8$ | $3.5^{+0.8}_{-0.8}$ | 0.000 |
| 16 | MMJ232524.05-033849.34 | 5.16 | $4.0 \pm 0.8$ | $3.4^{+0.8}_{-0.8}$ | 0.000 |
| 17 | MMJ232505.59−035100.82 | 5.11 | $3.5 \pm 0.7$ | $3.0^{+0.7}_{-0.7}$ | 0.000 |
| 18 | MMJ232509.96−034917.08 | 5.02 | $3.1 \pm 0.6$ | $2.7^{+0.7}_{-0.6}$ | 0.000 |
| 19 | MMJ232506.32−034806.83 | 5.01 | $3.1 \pm 0.6$ | $2.7^{+0.7}_{-0.6}$ | 0.000 |
| 20 | MMJ232540.17−034353.05 | 4.85 | $3.7 \pm 0.8$ | $3.1^{+0.8}_{-0.8}$ | 0.000 |
| 21 | MMJ232533.36−034926.22 | 4.76 | $3.7 \pm 0.8$ | $3.1^{+0.8}_{-0.8}$ | 0.000 |
| 22 | MMJ232454.81−034123.65 | 4.56 | $3.1 \pm 0.7$ | $2.6^{+0.7}_{-0.7}$ | 0.000 |
| 23 | MMJ232457.57−035037.59 | 4.31 | $3.2 \pm 0.7$ | $2.6^{+0.7}_{-0.8}$ | 0.001 |
| 24 | MMJ232536.49−034349.34 | 4.31 | $3.0 \pm 0.7$ | $2.5^{+0.7}_{-0.8}$ | 0.000 |
| 25 | MMJ232527.47−034054.16 | 4.27 | $3.0 \pm 0.7$ | $2.4^{+0.7}_{-0.7}$ | 0.001 |
| 26 | MMJ232530.43−034014.66 | 4.16 | $3.2 \pm 0.8$ | $2.6^{+0.8}_{-0.8}$ | 0.001 |
| 27 | MMJ232439.52−034322.33 | 4.12 | $3.6 \pm 0.9$ | $2.7^{+0.9}_{-0.9}$ | 0.002 |
| 28 | MMJ232530.15−034149.96 | 4.05 | $2.8 \pm 0.7$ | $2.2^{+0.7}_{-0.7}$ | 0.001 |
| 29 | MMJ232506.00−034104.93 | 3.94 | $2.4 \pm 0.6$ | $2.0^{+0.6}_{-0.7}$ | 0.002 |
| 30 | MMJ232524.29−034512.00 | 3.83 | $2.4 \pm 0.6$ | $1.9^{+0.7}_{-0.7}$ | 0.002 |
| 31 | MMJ232441.99−034553.09 | 3.82 | $2.9 \pm 0.8$ | $2.2^{+0.8}_{-0.8}$ | 0.004 |
| 32 | MMJ232452.97−034540.93 | 3.75 | $2.3 \pm 0.6$ | $1.8^{+0.6}_{-0.7}$ | 0.003 |
| 33 | MMJ232529.95−034747.21 | 3.72 | $2.4 \pm 0.7$ | $1.9^{+0.7}_{-0.7}$ | 0.004 |
| 34 | MMJ232524.82−034231.90 | 3.69 | $2.3 \pm 0.6$ | $1.8^{+0.7}_{-0.7}$ | 0.004 |
| 35 | MMJ232455.38−034854.19 | 3.69 | $2.5 \pm 0.7$ | $1.9^{+0.7}_{-0.7}$ | 0.004 |
| 36 | MMJ232440.61−034644.87 | 3.69 | $3.0 \pm 0.8$ | $2.2^{+0.8}_{-0.9}$ | 0.007 |
| 37 | MMJ232505.78−034952.76 | 3.67 | $2.3 \pm 0.6$ | $1.8^{+0.7}_{-0.7}$ | 0.004 |
| 38 | MMJ232508.83−034447.38 | 3.65 | $2.3 \pm 0.6$ | $1.8^{+0.7}_{-0.7}$ | 0.005 |
| 39 | MMJ232529.05−034907.34 | 3.60 | $2.5 \pm 0.7$ | $1.9^{+0.7}_{-0.7}$ | 0.006 |
| 40 | MMJ232512.22−034353.57 | 3.59 | $2.3 \pm 0.6$ | $1.7^{+0.7}_{-0.7}$ | 0.005 |
| 41 | MMJ232510.19−034444.52 | 3.57 | $2.3 \pm 0.6$ | $1.7^{+0.7}_{-0.7}$ | 0.006 |
| 42 | MMJ232514.38−035014.22 | 3.46 | $2.2 \pm 0.6$ | $1.6^{+0.7}_{-0.7}$ | 0.008 |
| 43 | MMJ232518.69−034707.59 | 3.45 | $2.2 \pm 0.6$ | $1.6^{+0.7}_{-0.7}$ | 0.008 |
| 44 | MMJ232456.51−033851.30 | 3.39 | $2.7 \pm 0.8$ | $1.9^{+0.9}_{-0.9}$ | 0.016 |
| 45 | MMJ232444.76−034344.01 | 3.37 | $2.4 \pm 0.7$ | $1.7^{+0.7}_{-0.8}$ | 0.014 |
| 46 | MMJ232541.02−034727.84 | 3.34 | $2.8 \pm 0.8$ | $1.9^{+0.9}_{-0.9}$ | 0.019 |
| 47 | MMJ232458.11−033747.04 | 3.32 | $3.0 \pm 0.9$ | $2.0^{+0.9}_{-1.0}$ | 0.024 |
| 48 | MMJ232507.54−035101.29 | 3.27 | $2.2 \pm 0.7$ | $1.6^{+0.7}_{-0.7}$ | 0.016 |
| 49 | MMJ232513.42−034447.55 | 3.17 | $2.0 \pm 0.6$ | $1.4^{+0.7}_{-0.7}$ | 0.019 |

**Table A13** – *continued*

| ID | IAU name | S/N | $S_{1.1mm}$ (measured) (mJy) | $S_{1.1mm}$ (deboosted) (mJy) | $P(<0)$ |
|---|---|---|---|---|---|
| 50 | MMJ232457.04−034811.52 | 3.15 | $2.0 \pm 0.6$ | $1.4^{+0.7}_{-0.7}$ | 0.020 |
| 51 | MMJ232529.42−034310.57 | 3.14 | $2.0 \pm 0.6$ | $1.4^{+0.7}_{-0.7}$ | 0.021 |
| 52 | MMJ232452.13−035113.84 | 3.13 | $2.8 \pm 0.9$ | $1.7^{+0.9}_{-1.0}$ | 0.037 |
| 53 | MMJ232527.62−035026.40 | 3.12 | $2.4 \pm 0.8$ | $1.6^{+0.8}_{-0.8}$ | 0.029 |
| 54 | MMJ232531.81−034339.82 | 3.11 | $2.0 \pm 0.7$ | $1.4^{+0.7}_{-0.7}$ | 0.023 |
| 55 | MMJ232509.54−033852.77 | 3.02 | $2.0 \pm 0.7$ | $1.4^{+0.7}_{-0.8}$ | 0.031 |

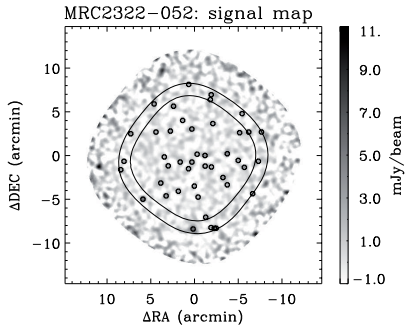


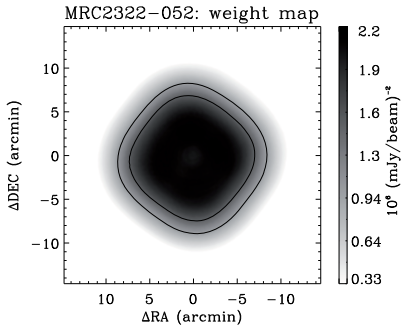


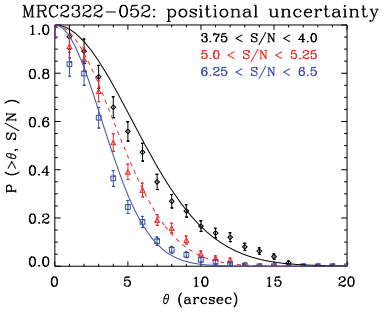


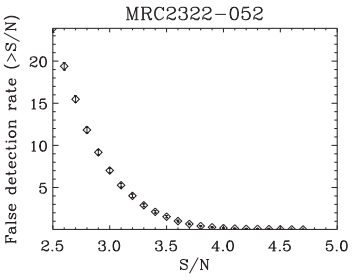


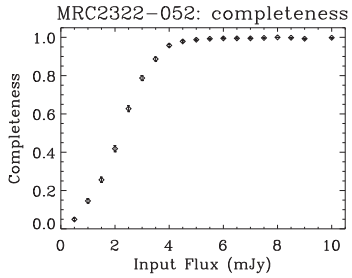


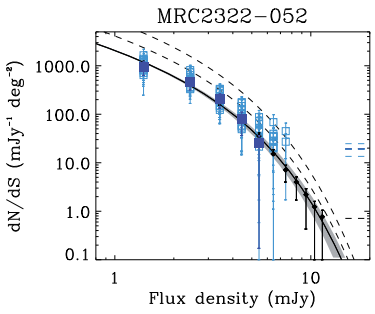


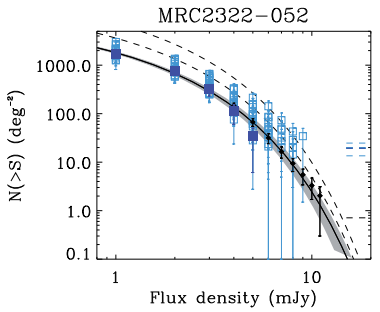


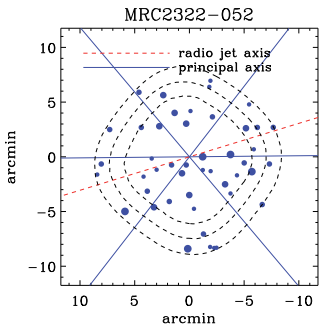


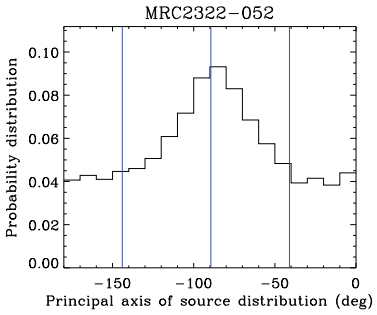


| S (mJy) | dN/dS (mJy$^{-1}$ deg$^{-2}$) | S (mJy) | N(>S) (deg$^{-2}$) |
|---|---|---|---|
| 1.4 | $943^{+258}_{-314}$ | 1.0 | $1713^{+281}_{-338}$ |
| 2.4 | $452^{+105}_{-134}$ | 2.0 | $770^{+130}_{-157}$ |
| 3.4 | $204^{+57}_{-71}$ | 3.0 | $317^{+74}_{-85}$ |
| 4.4 | $79^{+30}_{-43}$ | 4.0 | $113^{+39}_{-52}$ |
| 5.4 | $25^{+11}_{-24}$ | 5.0 | $33^{+16}_{-27}$ |

**Figure A14.** MRC2322−052 products.

**Table A14.** MRC2322−052 source catalogue.

| ID | IAU name | S/N | $S_{1.1mm}$ (measured) (mJy) | $S_{1.1mm}$ (deboosted) (mJy) | $P(<0)$ |
|---|---|---|---|---|---|
| 1 | MMJ232504.54−045724.13 | 7.09 | $4.9 \pm 0.7$ | $4.5^{+0.7}_{-0.7}$ | 0.000 |
| 2 | MMJ232514.75−045736.21 | 6.68 | $4.7 \pm 0.7$ | $4.2^{+0.7}_{-0.7}$ | 0.000 |
| 3 | MMJ232543.27−050236.04 | 6.55 | $6.0 \pm 0.9$ | $5.3^{+0.9}_{-0.9}$ | 0.000 |
| 4 | MMJ232520.22−050600.69 | 6.55 | $6.1 \pm 0.9$ | $5.3^{+1.0}_{-0.9}$ | 0.000 |
| 5 | MMJ232456.70−045857.92 | 5.92 | $4.4 \pm 0.7$ | $3.9^{+0.8}_{-0.7}$ | 0.000 |
| 6 | MMJ232530.66−045448.88 | 5.68 | $4.0 \pm 0.7$ | $3.5^{+0.7}_{-0.7}$ | 0.000 |
| 7 | MMJ232458.87−045459.93 | 5.54 | $4.2 \pm 0.8$ | $3.7^{+0.7}_{-0.8}$ | 0.000 |
| 8 | MMJ232520.80−045434.83 | 5.50 | $3.7 \pm 0.7$ | $3.3^{+0.7}_{-0.7}$ | 0.000 |
| 9 | MMJ232506.52−050007.33 | 5.49 | $3.8 \pm 0.7$ | $3.4^{+0.7}_{-0.8}$ | 0.000 |
| 10 | MMJ232529.21−045158.40 | 5.40 | $4.1 \pm 0.8$ | $3.6^{+0.8}_{-0.8}$ | 0.000 |
| 11 | MMJ232532.62−050213.34 | 5.26 | $3.9 \pm 0.7$ | $3.3^{+0.8}_{-0.7}$ | 0.000 |
| 12 | MMJ232525.05−045335.83 | 4.85 | $3.4 \pm 0.7$ | $2.9^{+0.7}_{-0.7}$ | 0.000 |
| 13 | MMJ232522.34−045907.04 | 4.76 | $3.3 \pm 0.7$ | $2.8^{+0.7}_{-0.7}$ | 0.000 |
| 14 | MMJ232519.67−050106.42 | 4.74 | $3.3 \pm 0.7$ | $2.8^{+0.7}_{-0.7}$ | 0.000 |
| 15 | MMJ232454.69−045455.67 | 4.67 | $3.9 \pm 0.8$ | $3.2^{+0.9}_{-0.8}$ | 0.000 |
| 16 | MMJ232459.51−045810.19 | 4.64 | $3.3 \pm 0.7$ | $2.8^{+0.7}_{-0.7}$ | 0.000 |
| 17 | MMJ232548.86−045507.04 | 4.60 | $4.4 \pm 1.0$ | $3.5^{+1.0}_{-1.0}$ | 0.000 |
| 18 | MMJ232514.46−050439.98 | 4.58 | $3.7 \pm 0.8$ | $3.0^{+0.8}_{-0.9}$ | 0.000 |
| 19 | MMJ232527.00−050141.68 | 4.52 | $3.2 \pm 0.7$ | $2.6^{+0.7}_{-0.7}$ | 0.000 |
| 20 | MMJ232520.78−045821.47 | 4.45 | $3.2 \pm 0.7$ | $2.6^{+0.7}_{-0.7}$ | 0.000 |
| 21 | MMJ232535.07−050045.24 | 4.44 | $3.1 \pm 0.7$ | $2.6^{+0.7}_{-0.7}$ | 0.000 |
| 22 | MMJ232526.16−045821.31 | 4.14 | $2.9 \pm 0.7$ | $2.3^{+0.7}_{-0.7}$ | 0.001 |
| 23 | MMJ232452.90−050158.34 | 4.01 | $4.0 \pm 1.0$ | $3.0^{+1.1}_{-1.1}$ | 0.004 |
| 24 | MMJ232511.17−045357.41 | 3.92 | $2.7 \pm 0.7$ | $2.1^{+0.8}_{-0.7}$ | 0.002 |
| 25 | MMJ232538.13−045142.68 | 3.86 | $3.6 \pm 0.9$ | $2.6^{+1.0}_{-1.0}$ | 0.006 |
| 26 | MMJ232551.95−045816.07 | 3.71 | $3.4 \pm 0.9$ | $2.4^{+1.0}_{-1.0}$ | 0.009 |
| 27 | MMJ232448.85−045455.18 | 3.65 | $3.7 \pm 1.0$ | $2.5^{+1.1}_{-1.1}$ | 0.013 |
| 28 | MMJ232450.26−045815.95 | 3.63 | $3.1 \pm 0.9$ | $2.2^{+0.9}_{-0.9}$ | 0.010 |
| 29 | MMJ232537.27−045455.61 | 3.55 | $2.6 \pm 0.7$ | $1.9^{+0.8}_{-0.8}$ | 0.009 |
| 30 | MMJ232531.65−045847.52 | 3.54 | $2.4 \pm 0.7$ | $1.8^{+0.7}_{-0.7}$ | 0.008 |
| 31 | MMJ232510.51−050556.44 | 3.48 | $3.4 \pm 1.0$ | $2.3^{+1.0}_{-1.1}$ | 0.020 |
| 32 | MMJ232514.70−045849.09 | 3.43 | $2.4 \pm 0.7$ | $1.7^{+0.8}_{-0.7}$ | 0.012 |
| 33 | MMJ232511.82−045855.21 | 3.37 | $2.3 \pm 0.7$ | $1.7^{+0.7}_{-0.8}$ | 0.014 |
| 34 | MMJ232518.38−045727.48 | 3.34 | $2.4 \pm 0.7$ | $1.7^{+0.7}_{-0.8}$ | 0.016 |
| 35 | MMJ232511.91−045039.60 | 3.33 | $3.0 \pm 0.9$ | $2.0^{+1.0}_{-1.0}$ | 0.026 |
| 36 | MMJ232533.45−045746.24 | 3.32 | $2.3 \pm 0.7$ | $1.6^{+0.7}_{-0.7}$ | 0.016 |
| 37 | MMJ232509.67−050555.14 | 3.28 | $3.2 \pm 1.0$ | $2.1^{+1.0}_{-1.1}$ | 0.034 |
| 38 | MMJ232512.31−045112.96 | 3.27 | $2.7 \pm 0.8$ | $1.8^{+0.9}_{-0.9}$ | 0.026 |
| 39 | MMJ232504.53−050057.73 | 3.27 | $2.3 \pm 0.7$ | $1.6^{+0.8}_{-0.8}$ | 0.019 |
| 40 | MMJ232553.43−045913.87 | 3.26 | $3.2 \pm 1.0$ | $2.0^{+1.1}_{-1.1}$ | 0.035 |
| 41 | MMJ232457.72−045249.33 | 3.19 | $3.0 \pm 0.9$ | $1.9^{+1.0}_{-1.1}$ | 0.039 |
| 42 | MMJ232517.94−050221.65 | 3.13 | $2.2 \pm 0.7$ | $1.5^{+0.8}_{-0.8}$ | 0.027 |
| 43 | MMJ232522.24−044928.85 | 3.08 | $3.0 \pm 1.0$ | $1.8^{+1.1}_{-1.1}$ | 0.054 |
| 44 | MMJ232512.01−050550.91 | 3.08 | $2.9 \pm 0.9$ | $1.7^{+1.0}_{-1.1}$ | 0.049 |

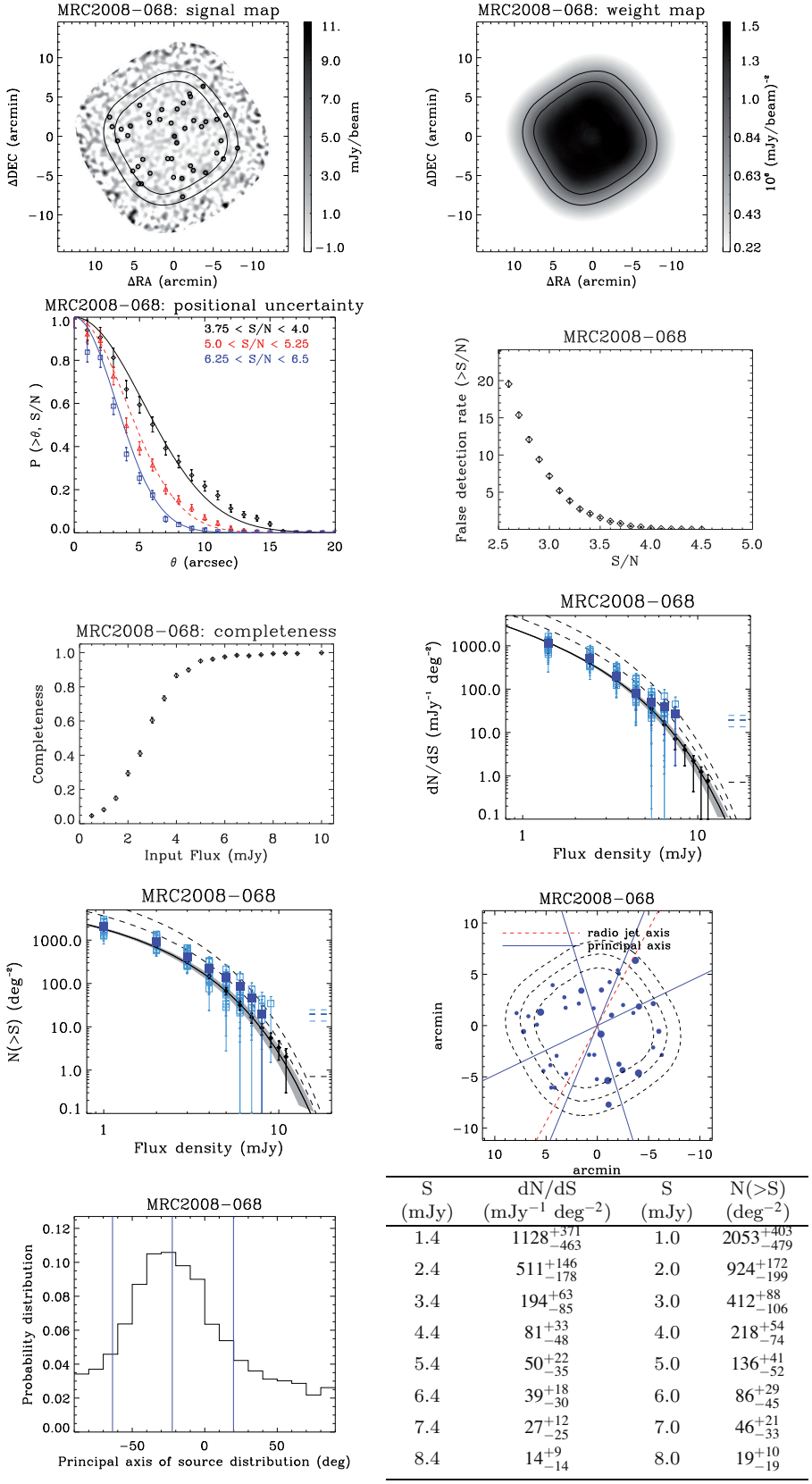


| S (mJy) | dN/dS (mJy$^{-1}$ deg$^{-2}$) | S (mJy) | N(>S) (deg$^{-2}$) |
|---|---|---|---|
| 1.4 | $1128^{+371}_{-463}$ | 1.0 | $2053^{+403}_{-479}$ |
| 2.4 | $511^{+146}_{-178}$ | 2.0 | $924^{+172}_{-199}$ |
| 3.4 | $194^{+63}_{-85}$ | 3.0 | $412^{+88}_{-106}$ |
| 4.4 | $81^{+33}_{-48}$ | 4.0 | $218^{+54}_{-74}$ |
| 5.4 | $50^{+22}_{-35}$ | 5.0 | $136^{+41}_{-52}$ |
| 6.4 | $39^{+18}_{-30}$ | 6.0 | $86^{+29}_{-45}$ |
| 7.4 | $27^{+12}_{-25}$ | 7.0 | $46^{+21}_{-33}$ |
| 8.4 | $14^{+9}_{-14}$ | 8.0 | $19^{+10}_{-19}$ |

**Figure A15.** MRC2008−068 products.

**Table A15.** MRC2008−068 source catalogue.

| ID | IAU name | S/N | $S_{1.1mm}$ (measured) (mJy) | $S_{1.1mm}$ (deboosted) (mJy) | $P(<0)$ |
|---|---|---|---|---|---|
| 1 | MMJ201113.99−064403.26 | 9.84 | $8.6 \pm 0.9$ | $8.0^{+0.9}_{-0.8}$ | 0.000 |
| 2 | MMJ201112.78−064453.62 | 8.20 | $7.1 \pm 0.9$ | $6.6^{+0.8}_{-0.9}$ | 0.000 |
| 3 | MMJ201110.11−064925.25 | 8.11 | $7.2 \pm 0.9$ | $6.6^{+0.9}_{-0.9}$ | 0.000 |
| 4 | MMJ201059.29−063742.32 | 7.66 | $8.7 \pm 1.1$ | $7.8^{+1.1}_{-1.2}$ | 0.000 |
| 5 | MMJ201058.04−064841.54 | 7.38 | $7.1 \pm 1.0$ | $6.4^{+1.0}_{-1.0}$ | 0.000 |
| 6 | MMJ201136.52−064245.13 | 6.93 | $6.1 \pm 0.9$ | $5.5^{+0.8}_{-0.9}$ | 0.000 |
| 7 | MMJ201057.88−064212.14 | 6.43 | $5.6 \pm 0.9$ | $5.0^{+0.9}_{-0.9}$ | 0.000 |
| 8 | MMJ201104.32−064824.44 | 6.00 | $5.3 \pm 0.9$ | $4.7^{+0.9}_{-0.9}$ | 0.000 |
| 9 | MMJ201109.79−065146.06 | 5.73 | $6.5 \pm 1.1$ | $5.5^{+1.1}_{-1.3}$ | 0.000 |
| 10 | MMJ201120.50−064039.46 | 5.58 | $4.8 \pm 0.9$ | $4.1^{+0.9}_{-0.9}$ | 0.000 |
| 11 | MMJ201143.19−064438.40 | 5.24 | $5.2 \pm 1.0$ | $4.4^{+1.0}_{-1.1}$ | 0.000 |
| 12 | MMJ201050.06−064437.35 | 5.02 | $4.7 \pm 0.9$ | $3.9^{+0.9}_{-1.0}$ | 0.000 |
| 13 | MMJ201108.63−064302.80 | 4.88 | $4.1 \pm 0.8$ | $3.4^{+0.9}_{-0.9}$ | 0.000 |
| 14 | MMJ201105.72−064749.47 | 4.77 | $4.1 \pm 0.9$ | $3.4^{+0.9}_{-0.9}$ | 0.000 |
| 15 | MMJ201112.60−064035.33 | 4.43 | $3.7 \pm 0.8$ | $3.0^{+0.8}_{-0.9}$ | 0.001 |
| 16 | MMJ201052.25−064155.02 | 4.18 | $4.1 \pm 1.0$ | $3.1^{+1.0}_{-1.0}$ | 0.002 |
| 17 | MMJ201130.22−064700.37 | 4.08 | $3.5 \pm 0.9$ | $2.7^{+0.9}_{-0.9}$ | 0.002 |
| 18 | MMJ201105.77−063859.77 | 4.03 | $3.6 \pm 0.9$ | $2.8^{+0.9}_{-1.0}$ | 0.003 |
| 19 | MMJ201104.09−064203.47 | 3.94 | $3.4 \pm 0.9$ | $2.6^{+0.9}_{-0.9}$ | 0.003 |
| 20 | MMJ201137.94−064358.29 | 3.80 | $3.4 \pm 0.9$ | $2.5^{+0.9}_{-1.0}$ | 0.006 |
| 21 | MMJ201115.67−064222.47 | 3.74 | $3.2 \pm 0.9$ | $2.4^{+0.9}_{-0.9}$ | 0.007 |
| 22 | MMJ201109.40−063949.44 | 3.69 | $3.2 \pm 0.9$ | $2.4^{+0.9}_{-1.0}$ | 0.008 |
| 23 | MMJ201106.18−063840.00 | 3.65 | $3.3 \pm 0.9$ | $2.4^{+1.0}_{-1.0}$ | 0.010 |
| 24 | MMJ201052.28−064611.67 | 3.65 | $3.3 \pm 0.9$ | $2.4^{+1.0}_{-1.0}$ | 0.010 |
| 25 | MMJ201127.18−064118.07 | 3.60 | $3.1 \pm 0.9$ | $2.2^{+0.9}_{-0.9}$ | 0.010 |
| 26 | MMJ201132.65−064755.13 | 3.57 | $3.3 \pm 0.9$ | $2.2^{+1.0}_{-1.0}$ | 0.013 |
| 27 | MMJ201126.68−064219.64 | 3.56 | $3.0 \pm 0.8$ | $2.2^{+0.9}_{-0.9}$ | 0.011 |
| 28 | MMJ201130.96−065006.68 | 3.54 | $3.6 \pm 1.0$ | $2.4^{+1.1}_{-1.1}$ | 0.017 |
| 29 | MMJ201145.94−064250.69 | 3.45 | $3.7 \pm 1.1$ | $2.4^{+1.1}_{-1.2}$ | 0.024 |
| 30 | MMJ201048.88−064655.33 | 3.44 | $3.5 \pm 1.0$ | $2.2^{+1.1}_{-1.1}$ | 0.023 |
| 31 | MMJ201132.33−065006.60 | 3.42 | $3.6 \pm 1.0$ | $2.4^{+1.1}_{-1.2}$ | 0.026 |
| 32 | MMJ201115.41−064654.72 | 3.30 | $2.8 \pm 0.8$ | $1.9^{+0.9}_{-0.9}$ | 0.023 |
| 33 | MMJ201135.39−064829.08 | 3.29 | $3.3 \pm 1.0$ | $2.1^{+1.1}_{-1.1}$ | 0.033 |
| 34 | MMJ201041.60−064533.73 | 3.22 | $4.0 \pm 1.2$ | $2.2^{+1.3}_{-1.5}$ | 0.057 |
| 35 | MMJ201100.08−064249.71 | 3.20 | $2.7 \pm 0.9$ | $1.8^{+0.9}_{-0.9}$ | 0.031 |
| 36 | MMJ201047.60−064121.69 | 3.11 | $3.7 \pm 1.2$ | $1.9^{+1.3}_{-1.4}$ | 0.067 |
| 37 | MMJ201141.30−064309.16 | 3.10 | $2.9 \pm 0.9$ | $1.8^{+1.0}_{-1.1}$ | 0.045 |
| 38 | MMJ201131.78−064007.03 | 3.09 | $2.9 \pm 0.9$ | $1.8^{+1.0}_{-1.1}$ | 0.046 |
| 39 | MMJ201114.41−064917.27 | 3.04 | $2.6 \pm 0.9$ | $1.6^{+0.9}_{-1.0}$ | 0.046 |
| 40 | MMJ201117.44−064654.47 | 3.04 | $2.6 \pm 0.8$ | $1.6^{+0.9}_{-1.0}$ | 0.044 |
| 41 | MMJ201126.47−064846.27 | 3.03 | $2.6 \pm 0.9$ | $1.6^{+0.9}_{-1.0}$ | 0.047 |

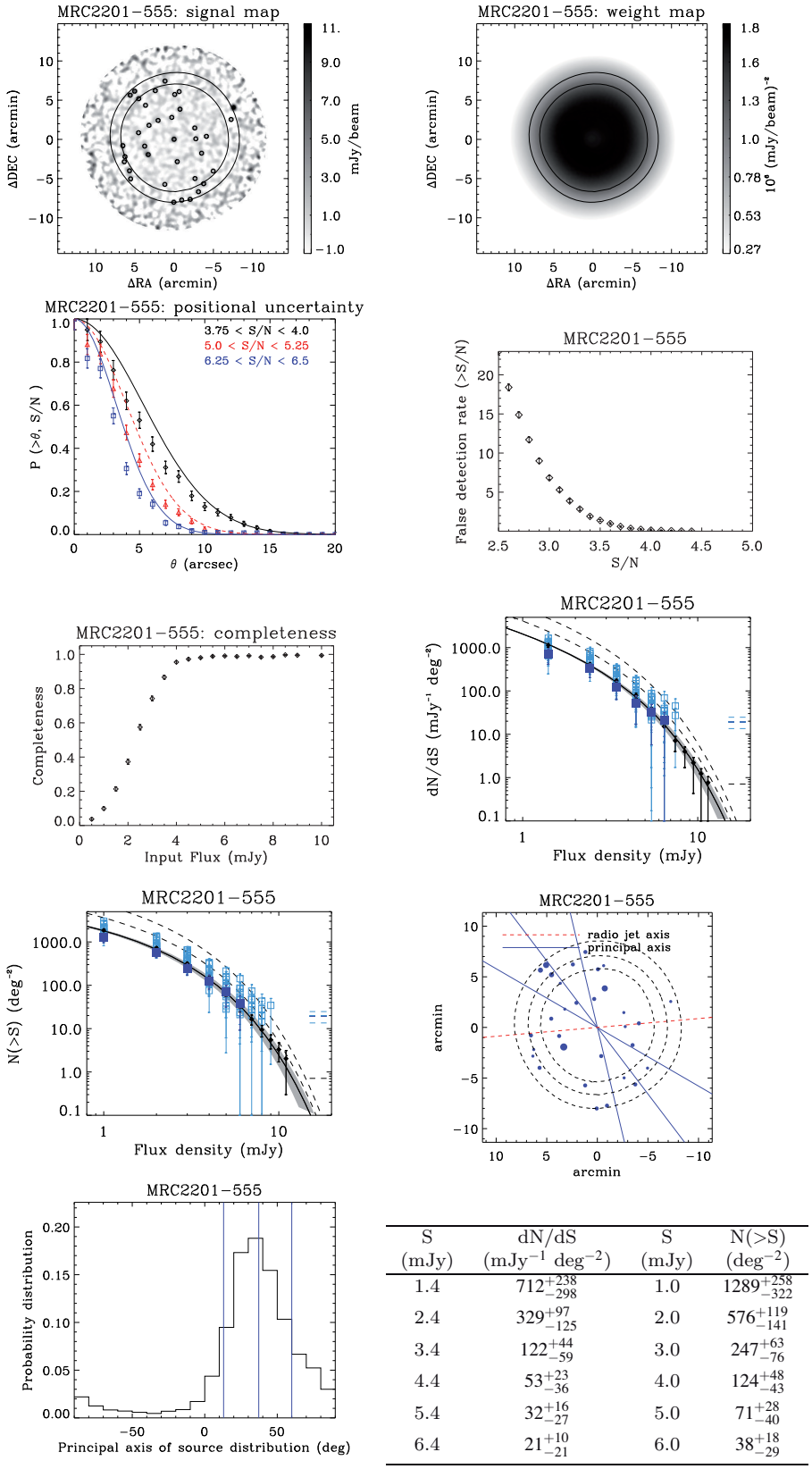


| S (mJy) | dN/dS (mJy$^{-1}$ deg$^{-2}$) | S (mJy) | N(>S) (deg$^{-2}$) |
|---|---|---|---|
| 1.4 | $712^{+238}_{-298}$ | 1.0 | $1289^{+258}_{-322}$ |
| 2.4 | $329^{+97}_{-125}$ | 2.0 | $576^{+119}_{-141}$ |
| 3.4 | $122^{+44}_{-59}$ | 3.0 | $247^{+63}_{-76}$ |
| 4.4 | $53^{+23}_{-36}$ | 4.0 | $124^{+48}_{-43}$ |
| 5.4 | $32^{+16}_{-27}$ | 5.0 | $71^{+28}_{-40}$ |
| 6.4 | $21^{+10}_{-21}$ | 6.0 | $38^{+18}_{-29}$ |

**Figure A16.** MRC2201−555 products.

**Table A16.** MRC2201−555 source catalogue.

| ID | IAU name | S/N | $S_{1.1mm}$ (measured) (mJy) | $S_{1.1mm}$ (deboosted) (mJy) | $P(<0)$ |
|---|---|---|---|---|---|
| 1 | MMJ220528.18−551939.97 | 10.24 | $7.7 \pm 0.8$ | $7.3^{+0.8}_{-0.7}$ | 0.000 |
| 2 | MMJ220504.97−551742.63 | 7.84 | $6.1 \pm 0.8$ | $5.7^{+0.8}_{-0.8}$ | 0.000 |
| 3 | MMJ220540.28−551134.15 | 6.93 | $7.2 \pm 1.0$ | $6.4^{+1.0}_{-1.1}$ | 0.000 |
| 4 | MMJ220459.69−551352.65 | 6.91 | $5.3 \pm 0.8$ | $4.8^{+0.8}_{-0.8}$ | 0.000 |
| 5 | MMJ220544.24−551204.60 | 5.89 | $6.1 \pm 1.0$ | $5.2^{+1.1}_{-1.1}$ | 0.000 |
| 6 | MMJ220536.57−551231.83 | 5.67 | $5.1 \pm 0.9$ | $4.3^{+0.9}_{-0.9}$ | 0.000 |
| 7 | MMJ220502.14−552033.87 | 5.10 | $3.8 \pm 0.7$ | $3.3^{+0.8}_{-0.8}$ | 0.000 |
| 8 | MMJ220440.34−551928.87 | 5.01 | $3.8 \pm 0.8$ | $3.2^{+0.8}_{-0.8}$ | 0.000 |
| 9 | MMJ220545.02−552143.49 | 4.64 | $4.4 \pm 1.0$ | $3.5^{+1.0}_{-1.0}$ | 0.000 |
| 10 | MMJ220550.93−551831.39 | 4.49 | $4.0 \pm 0.9$ | $3.2^{+0.9}_{-0.9}$ | 0.000 |
| 11 | MMJ220531.36−551834.71 | 4.23 | $3.2 \pm 0.8$ | $2.6^{+0.8}_{-0.8}$ | 0.001 |
| 12 | MMJ220438.42−552322.08 | 4.21 | $3.9 \pm 0.9$ | $3.0^{+0.9}_{-1.0}$ | 0.002 |
| 13 | MMJ220519.32−551518.35 | 4.12 | $3.1 \pm 0.8$ | $2.5^{+0.8}_{-0.8}$ | 0.001 |
| 14 | MMJ220458.10−552527.71 | 4.06 | $4.4 \pm 1.1$ | $3.2^{+1.1}_{-1.1}$ | 0.004 |
| 15 | MMJ220505.27−552544.62 | 3.91 | $4.3 \pm 1.1$ | $3.0^{+1.2}_{-1.2}$ | 0.007 |
| 16 | MMJ220521.77−551130.71 | 3.90 | $3.4 \pm 0.9$ | $2.5^{+0.9}_{-0.9}$ | 0.004 |
| 17 | MMJ220507.01−551455.39 | 3.79 | $2.9 \pm 0.8$ | $2.2^{+0.8}_{-0.8}$ | 0.004 |
| 18 | MMJ220513.29−552327.89 | 3.76 | $3.1 \pm 0.8$ | $2.3^{+0.8}_{-0.9}$ | 0.006 |
| 19 | MMJ220513.09−551017.09 | 3.69 | $3.5 \pm 1.0$ | $2.5^{+1.0}_{-1.1}$ | 0.010 |
| 20 | MMJ220504.42−551159.46 | 3.67 | $2.9 \pm 0.8$ | $2.2^{+0.8}_{-0.9}$ | 0.007 |
| 21 | MMJ220435.99−551719.83 | 3.58 | $2.7 \pm 0.8$ | $2.0^{+0.8}_{-0.8}$ | 0.008 |
| 22 | MMJ220536.82−551652.28 | 3.47 | $2.7 \pm 0.8$ | $1.9^{+0.8}_{-0.8}$ | 0.012 |
| 23 | MMJ220500.45−551137.97 | 3.36 | $2.7 \pm 0.8$ | $1.9^{+0.9}_{-0.9}$ | 0.019 |
| 24 | MMJ220429.92−552145.35 | 3.22 | $2.8 \pm 0.9$ | $1.8^{+0.9}_{-1.0}$ | 0.030 |
| 25 | MMJ220527.41−551555.59 | 3.19 | $2.4 \pm 0.8$ | $1.6^{+0.8}_{-0.8}$ | 0.025 |
| 26 | MMJ220413.92−551510.40 | 3.18 | $3.2 \pm 1.0$ | $2.0^{+1.1}_{-1.1}$ | 0.042 |
| 27 | MMJ220446.20−552243.01 | 3.17 | $2.6 \pm 0.8$ | $1.7^{+0.8}_{-0.9}$ | 0.030 |
| 28 | MMJ220549.64−552034.16 | 3.17 | $3.0 \pm 0.9$ | $1.9^{+1.0}_{-1.1}$ | 0.039 |
| 29 | MMJ220530.51−551322.57 | 3.15 | $2.5 \pm 0.8$ | $1.6^{+0.9}_{-0.9}$ | 0.030 |
| 30 | MMJ220450.50−552522.40 | 3.13 | $3.5 \pm 1.1$ | $2.0^{+1.1}_{-1.3}$ | 0.057 |
| 31 | MMJ220446.45−551615.92 | 3.13 | $2.4 \pm 0.8$ | $1.6^{+0.8}_{-0.8}$ | 0.030 |
| 32 | MMJ220544.00−552244.97 | 3.09 | $3.2 \pm 1.0$ | $1.8^{+1.1}_{-1.2}$ | 0.054 |
| 33 | MMJ220445.48−551739.17 | 3.09 | $2.3 \pm 0.8$ | $1.5^{+0.8}_{-0.8}$ | 0.033 |
| 34 | MMJ220549.03−551955.20 | 3.07 | $2.8 \pm 0.9$ | $1.7^{+0.9}_{-1.0}$ | 0.046 |
| 35 | MMJ220443.05−552423.95 | 3.04 | $3.1 \pm 1.0$ | $1.7^{+1.1}_{-1.1}$ | 0.059 |

[1]*Universidad de las Américas Puebla, Sta. Catarina Mártir, San Andrés Cholula, 72810 Puebla, Mexico*
[2]*Instituto Nacional de Astrofísica, Óptica y Electrónica (INAOE), Aptdo. Postal 51 y 216, 72000 Puebla, Mexico*
[3]*Instituto de Astrofísica e Ciências do Espaço, Universidade do Porto, CAUP, Rua das Estrelas, P-4150-762 Porto, Portugal*
[4]*Department of Astronomy, University of Massachusetts, Amherst, MA 01003, USA*
[5]*Center for Astrophysics and Space Astronomy, University of Colorado, Boulder, CO 80309, USA*
[6]*Institute for Astronomy, University of Edinburgh, Royal Observatory, Blackford Hill, Edinburgh EH9 3HJ, UK*
[7]*ALMA Project Office, National Astronomical Observatory of Japan, 2-21-1 Osawa, Mitaka, Tokyo 181-0015, Japan*
[8]*Institute of Astronomy, University of Tokyo, 2-21-1 Osawa, Mitaka, Tokyo 181-0015, Japan*
[9]*European Southern Observatory, Karl Schwarzschild Strasse 2, D-85748 Garching, Germany*
[10]*National Astronomical Observatory of Japan, 2-21-1 Osawa, Mitaka, Tokyo 181-8588, Japan*
[11]*Department of Astronomy, School of Science, The University of Tokyo, 7-3-1 Hongo, Bunkyo-ku, Tokyo 113-0033, Japan*
[12]*The Graduate University for Advanced Studies (SOKENDAI), 2-21-1 Osawa, Mitaka, Tokyo 181-8588, Japan*
[13]*Astronomy and Space Science Department, Sejong University, Seoul 143-747, South Korea*
[14]*Research Center for the Early Universe, University of Tokyo, 7-3-1 Hongo, Bunkyo-ku, Tokyo 113-0033, Japan*
[15]*National Observatory of Athens, Lofos Nymfon, Athens 11810, Greece*
[16]*Physics Department, Aristotle University of Thessaloniki, 54124 Thessaloniki, Greece*
[17]*Centre for Astrophysics, Science and Technology Research Institute, University of Hertfordshire, Hatfield AL10 9AB, UK*

This paper has been typeset from a TEX/LATEX file prepared by the author.